Sapphire Optical Fibre Interferometric Sensors

Zilan Yu

Submitted for the degree of Master of Science
Department of Mechanical Engineering
Faculty of Engineering
University of Glasgow

Date of Completion: 10/12/2002

This is the original work of the author

Zilan Yu

ARCKNOWLEDGEMENTS

Over the years, many people have been kind enough to share their thoughts about my work with me and I take this opportunity to express my appreciation to them all.

I would like to express my gratitude to my academic supervisor, Dr. James H. Sharp, for his guidance, and continual support in making this thesis come to pass.

Many thanks to Dr. Ian Watson for his constructive suggestions and encouragement on my work.

The technical support given in this course of work was excellent and I would like to thank, especially Mr. Ian Peden and not forgetting the rest who contributed, one way or another towards my experimental work.

Acknowledgements are also extended to Boon Kiat Tan and Kun Guo for their constant spiritual support and all my friends and colleagues, who have helped to create a friendly and enjoyable atmosphere both within and outwith my work place.

Never will I forget and appreciate the love, patience and provision from my dear parents, law-in-parents, wife, and sister for without them, my academic career will not be possible and a success.

This course of research was supported by Department of Mechanical Engineering, University of Glasgow award.

Contents

Abstract

This thesis is mainly concerned with the development of single crystal fibre interferometric sensors. By studying the functional relationship between the angle of wedge-shaped air gap and the separation of consecutive fringes of equal thickness, results shows that the percentage difference of angles between the method of interference fringes and the direct calculated method is about 3.99%. Thus, a procedure of prototype was established to monitor the process of fabrication of a Fabry-Perot cavity.

An intrinsic sapphire fibre-optic Fabry-Perot sensor was fabricated, and the functional relationship between the output of interference signal of the intrinsic sapphire fibre-optic Fabry-Perot sensor and temperature was deduced. The fitting equation, the functional relationship between temperature and the output of the number of interference fringes of the intrinsic sapphire fibre-optic Fabry-Perot sensor, was obtained by data fitting. There is a near linear relationship between the temperature measured and the output signal of the intrinsic sapphire fibre-optic Fabry-Perot sensor for the range of temperature 75 °C - 435 °C.

An extrinsic sapphire fibre-optic Fabry-Perot sensor was fabricated, and the functional relationship between the output of interference signal of the extrinsic sapphire fibre-optic Fabry-Perot sensor and temperature was deduced. High temperature ceramic adhesive based on aluminum oxide was presented to solve the problem of unmatched thermal expansion between the support materials and the extrinsic sapphire fibre-optic Fabry-Perot sensor. Theoretical analysis showed that during the process of the fabrication of the interferometer cavity, the length of Fabry-Perot cavity for fabricating should be tightly controlled.

Phase relationships between the output of the interference signal of a monolithic sapphire fibre-optic Fabry-Perot sensor and the angular frequency of sound wave was deduced. Some monolithic sapphire Fabry-Perot cavities were fabricated, and their internal surfaces were observed. The optical quality of the internal surface of the melted end of the sapphire Fabry-Perot cavities was assessed by Michelson interferometric testing. The experiments showed that interference fringes of equal inclination could be achieved if the internal surface of the monolithic sapphire Fabry-Perot cavities were approximately planar surface. Obviously, there is the potential to fabricate a monolithic sapphire fibre-optic Fabry-Perot sensor by the sapphire tube sheath method. Four problems are presented to discuss which should be solved in future in consideration to the structure and assembly of the monolithic sapphire fibre-optic Fabry-Perot sensor:

This study in this thesis has elucidated the problems associated with procedures in fabrication, assembly, and test of sapphire fibre-optic Fabry-Perot sensor, and achieved greater insights into fabrication of the monolithic sapphire fibre-optic Fabry-Perot sensor which shows the market potential of such an approach in Aerospace and Automobile applications.

§1 Introduction

During the past several decades, the measurement of temperature and vibration has always been a prominent aspect in the field of engineering; for variations of temperature and strain are vital indicators of changes in chemical, physical and biological processes. Therefore, temperature and strain are the important parameters of sensing and instrumentation.

To date, rapidly developing optical fibre sensor technology has emerged as replacements of existing measuring techniques, or extensions of measurement capabilities. The use of optical fibre methods offers added flexibility in comparison with traditional methods, and yields a number of characteristic benefits over electro-magnetic approach [1,2,3,4].

Additionally, current advances in technology have made demand for materials that can support mechanical loading under high temperature, high pressure and high strain environments. Recent progress in this field has quickened the development of these kinds of materials such as ceramic, metal and ceramic composite materials which have found increasing uses in design and fabrication of high performance structures in military, civil and industrial applications.

The structures constituted by these materials can be exposed to temperatures in excess of 1000 °C in aerospace and combustion engines, as well as experience continuous cyclic loading or high magnitude static loading. Therefore, it becomes necessary to monitor and test their performance under conditions that exceed those expected in practical applications.

Conventional sensors are generally unable to survive under high temperature environments (> 1000 °C). Thus, for effective detection of strain and / or vibration in high temperature and electromagnetic environments, we require new kinds of sensors such as fibre-optic sensors [5].

A wide range of fibre-optic sensor designs is available. We have chosen to investigate and design a new kind of fibre-optic Fabry-Perot sensor to detect pressure and vibration waves under high temperatures.

§2 Background and Theory

§2.1 Interferometers

§2.11 Michelson Interferometer

A schematic of the Michelson Interferometer is shown in Figure 2 - 1. A beam (1) of light, from an extended source of light S, is split by a beam splitter into reflected beam (2) and transmitted beam (3), of roughly equal amplitudes. They all continue to be reflected by Mirror 2 and Mirror 1, respectively and return to the beam splitter so that they come together again and demonstrate the interference. One of the mirrors is equipped with tilting adjustment screws that ensures the surfaces of two mirrors are mutually perpendicular. One of the mirrors is also movable along the direction of the beam as a sensing arm.

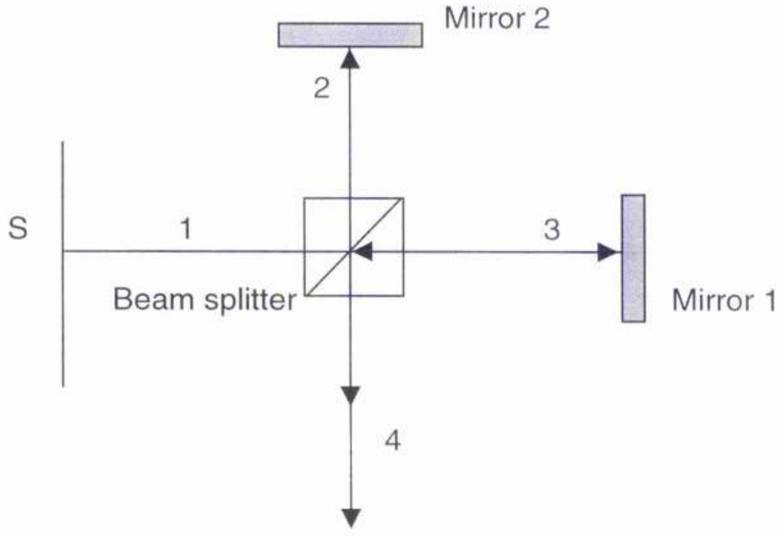

Figure 2 - 1 The Michelson Interferometer

Michelson Interferometer is easily adaptable to measurement of thin films, the determination of index of refraction of a gas, vibration, etc.

§2.12 Fabry-Perot Interferometer

Although simple in structure, the Fabry-Perot Interferometer is a high-resolution instrument that has proved to be a powerful tool in a wide variety of applications such as precision wavelength measurements, analysis of hyperfine spectral line structure, determination of refractive indices of gases, the calibration of the standard meter in terms of wavelength, etc [6].

A typical setup is shown in Figure 2 - 2. Two glass, semi-silvered plates are used to form a plane parallel air gap between plates, within which the beams are multiply reflected. A narrow, monochromatic beam from an extended source with an angle θ with respect to the optical axis of the system produces multiple coherent beams. These parallel rays are brought together at a focus P in the focal plane of lens L. The output of Fabry-Perot Interferometer will be a series of sharp concentric fringes on the screen.

The adjustment of the Fabry-Perot Interferometer is similar to that of the Michelson interferometer in many ways.

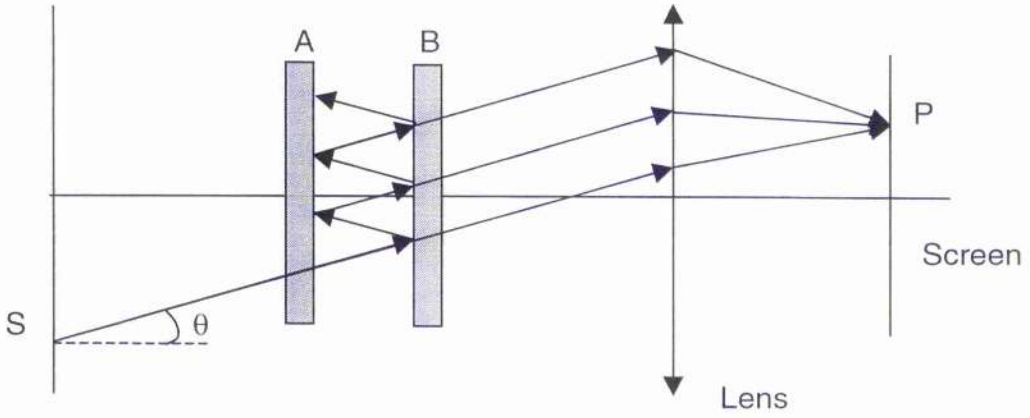

Figure 2 - 2 Febry-Perot Interferometer

§2.2 Overview of Fibre-optic Sensors

Fibre optic sensors are widely used for measuring temperature, displacement, speed, acceleration, angle, pressure, rate of flow, and so on. They have been shown to be equally effective and in some cases exceed existing kinds of sensors. They are especially suitable to be installed in harsh environments such as radiation, corrosion, electromagnetism, etc. Moreover, they are easy to fabricate, have miniaturized sizes and light weight, and can realise remote sensing by connecting with large-scale optical fibre communication networks.

Conventional silica-based optical fibres can be used in medium temperature environments up to 800 °C limited by the softening point of the silica glass fibre material and thermal diffusion of impurities which gradually degrades the waveguide modal properties of the fibre [7]. However, in some applications, higher temperatures may be encountered. Therefore, new materials tolerant of high temperatures to substitute for the glass materials are needed to make sensors. The first sapphire rod-based high temperature sensor was demonstrated by Dils [8] *et al.* in 1982, in which the sapphire-based materials high temperature melting point of 2048 °C was exploited. In this sensor, a metal with a high melting point was deposited onto the fibre tip to serve as a blackbody radiator, and the measured temperature information was extracted by taking the ratio of two specifically selected wavelengths emitted by the blackbody. The measured range of temperatures is from 600°C to approximately 2000 °C. Later, Murphy [9] *et al.* first described a single crystal sapphire rod-based fibre Fabry-Perot interferometric sensor for measurement of acoustic waves and temperature, a

2.25MHz acoustic wave was detected and the phase shift was shown as a function of temperatures from 20 °C to 100 °C. In 1992, an intrinsic sapphire fibre based Fabry-Perot interferometric sensor was demonstrated by Anbo Wang for the measurement at temperatures up to and above 1500 °C, which a resolution of 0.1 °C was obtained [10]. Wang further developed the extrinsic sapphire fibre based Fabry-Perot interferometric sensor in 1994 [11] to detect both strain and temperature measurement, with 10 microstrain resolution over a range of 0 - 1150 microstrain, and 3.5 °C temperature resolution over a range from 150 °C to 650 °C. Recently, a ruby fibre for fluorescence-based temperature sensor was produced by Sharp, *et al.* [12] using the miniature pedestal growth technique. Fluorescence lifetime taken over the range from 0 °C to 600 °C was presented and the measurement deviations of the entire temperature region were less than a temperature change of 0.2 °C.

§2.3 Fibre-optic Sensors

Fibre-optic sensors can be made to be highly sensitive to strain, temperature, pressure and acoustic waves [13, 14, 15]. Since such sensors offer the advantages of simple configuration, single-ended operation, high resolution and potential low cost, different methods for the construction of interference cavities of fibre-optic sensors and output signal demodulation have been developed over the past few years. Fibre-optic sensors can be generally classified into two types, intrinsic and extrinsic interferometric sensors.

§2.31 Fibre-optic Intrinsic Sensors

Intrinsic fibre-optic sensors rely on the properties of the optical fibre itself to convert an environmental action into a modulation of the light beam passing through it. Furthermore, They may be further divided into subclasses by considering the type of modulation impressed on the light beam such as phase, polarisation modulation, intensity, etc [16].

In intrinsic sensors, the fibre construction materials are deliberately chosen in order to give sensitivity to one or more parameters. Often it is not cost effective to make highly specialized fibres for sensing applications. Therefore, intrinsic sensors may utilize readily available fibre in specialized configurations and in conjunction with sophisticated instrumentation.

Mach-Zehnder fibre interferometer first reported by G. B. Hocker [17] in 1979 is the typical intrinsic fibre sensor, which was used to detect pressure and temperature, etc. Figure 2 - 3 shows an all-fibre Mach-Zehnder interferometer. A beam splitter splits the light from the source into two beams which will be coupled into two monomode fibres. The two guided beams will be combined to produce a set of bright and dark interference fringes observable if the optical path difference of the two arms is within the coherence length of the source. If one fibre is subjected to changes in strain, temperature, etc., the phase of the light leaving the fibre will be changed due to the dimensional or index of refraction changes in the fibre. As a result, the difference of pressure, temperature, etc, will appear as a displacement of the fringes which can be measured.

However, the system is also subject to two problems in spite of its high resolution. First, the fringe number is lost when it is switched off. Second, it requires calibration for it is not an absolute device. Many methods have been used to recover the value of the measurand without resort to recalibration such as white light interferometry, etc [4].

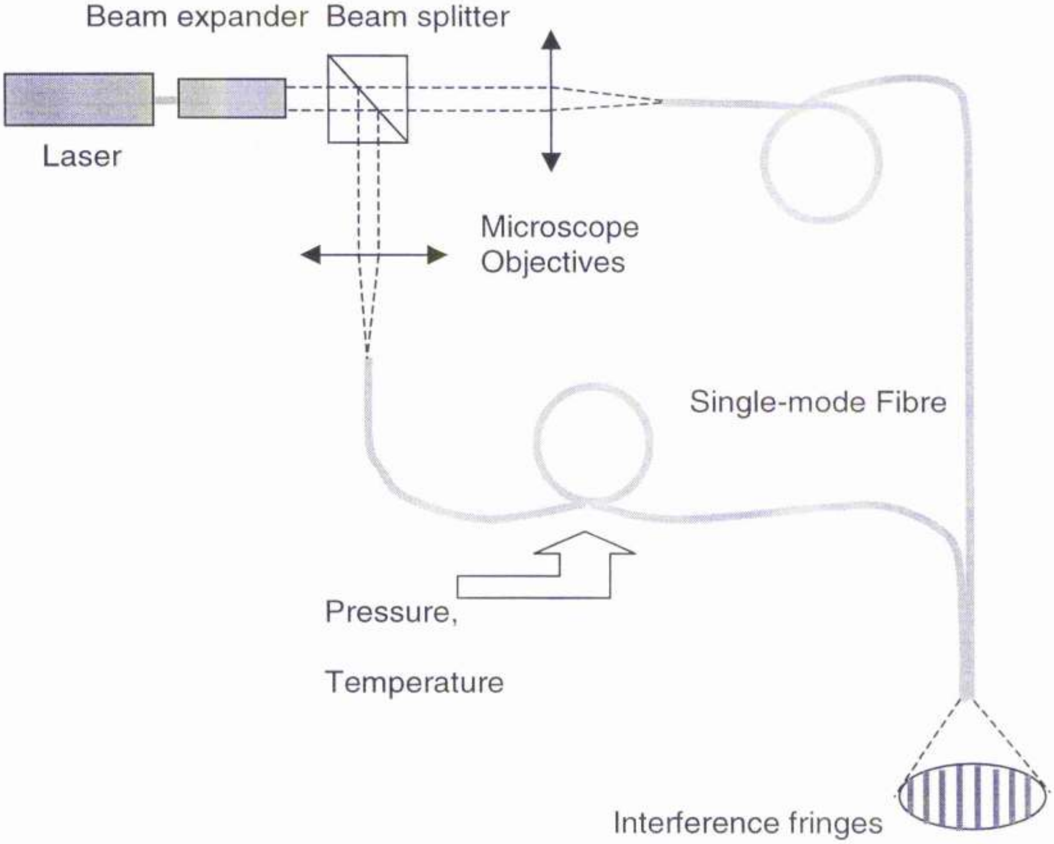

Figure 2 - 3 Single-mode Fibre- optic Mach-Zehnder Interferometer

Fibre-optic Fabry-Perot-type interferometric sensors, as shown in Figure 2 - 4, involve a type of intrinsic sensor. Two endfaces of a length of single mode fibre are optically polished by the same angle and coated with the multilayer of thin dielectric films to form a low-finesse Fabry-Perot cavity, which the typical length of cavity is, generally, a few centimetres. A transmitting fibre was connected by fusion splicing the length of Fabry-Perot cavity. Very high resolution over a temperature range of ~ 80°C can be achieved [18, 19].

Obviously, this type of sensor is very compact, and thus can be used for the applications where the traditional sensors with a bigger size can not be used. However, it suffers from some problems such as the polarization fading, the effects of temperature cross sensitivity, etc.

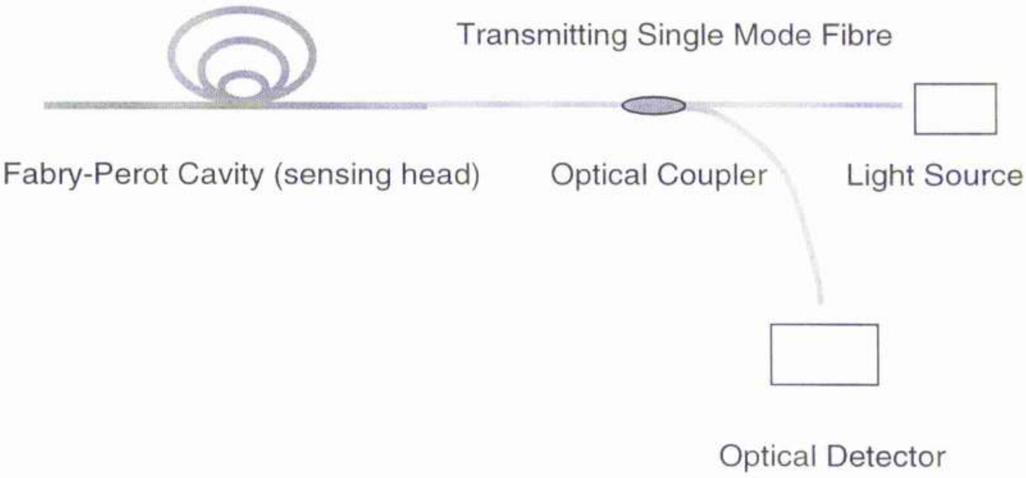

Figure 2 - 4 Schematic of the Fibre-optic Fabry-Perot-type Intrinsic Interferometric Sensor

§2.32 Fibre-optic Extrinsic Sensors

The fibres may be used strictly as information carriers that lead to a black box which impresses information on a light beam that propagates to a remote receiver through a second, or in some cases, the same fibre. That black box may contain mirrors, gas or liquid cells, or dozens of other mechanisms that may generate, modulate, or transform the light beam [20].

Fibre-optic Laser Doppler Velocimetry [21] is one type of extrinsic sensor commercially available from many manufacturers. Figure 2 - 5 shows the arrangement of fibre-optic laser Doppler velocimetry. The input beam from a laser source is divided by a coupler into two beams which are guided into two fibres. The measurement range is formed by the region of intersection of two coherent output beams of the two fibres. The scattered beam from the measurement range is then collected by a lens and combined with the reference beam. These two beams are independent and Doppler shifted. The different frequency shifts for the two beams beat together to form a frequency Δ v which is a function of the velocity of the scattering particle.

Fibre-optic Laser Doppler Velocimetry is often used for surface vibration analysis and calibration. Nevertheless, the application of vibration measurement is limited by the general requirement of a same direct line between the target and laser, and a good environment. Therefore, various fibre-optic interferometers have been investigated as a choice, such as fibre-optic Michelson-type interferometric sensors, fibre-optic Fabry-Perot-type interferometric sensors, etc.

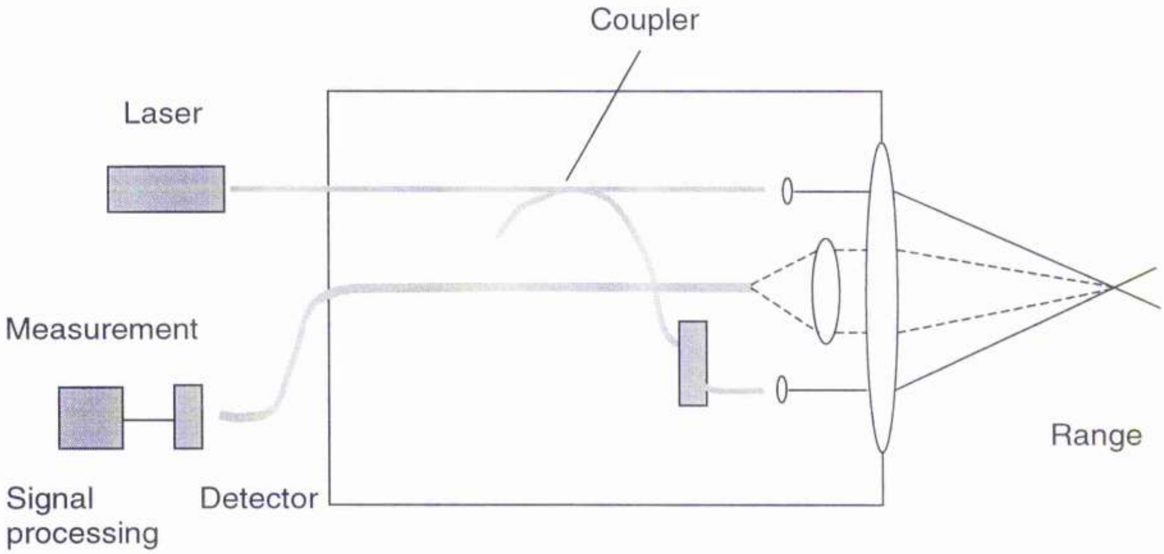

Figure 2 - 5 Sketch of Fibre-optic Laser Doppler Velocimetry

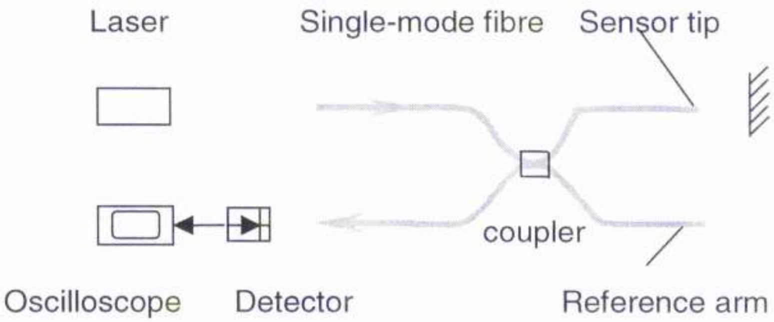

Figure 2 - 6 Schematic of Fibre-optic Michelson-type Interferometric Sensors

Fibre-optic michelson-type interferometric sensor is also a type of extrinsic sensor. Its basic principle is the same as that of Michelson interferometer discussed in section 2.11 above. The schematic of the sensor is shown in Figure 2 - 6.

The fibre-optic Michelson-type Interferometric sensor is often widely used to detect acoustic waves, microdisplacement, etc. Its sensing arm and its reference arm are physically laid on different sites, hence a tiny change in temperature in the reference arm may affect the phase difference detected at the output of the sensor. Many methods have been proposed to solve the problem such as Y junction method [22], active feedback method in the reference arm [23], etc.

An improved configuration of the fibre-optic Michelson-type interferometric sensors [22] has been described as is shown in Figure 2 - 7.

A fused-biconical tapered coupler was constructed from a single-mode fibre. The two output arms of the coupler were cleaved immediately after the coupling length. The coupler was attached to Invar strips with epoxy and polished. One core with a mirrored end is used as the reference arm and the uncoated core served the purpose of the sensing arm.

This sensor is highly stable, and virtually insensitive to temperature drifts in comparison to a classic Michelson-type sensor. It can be used for the measurement of microdisplacements, magnetic fields, and surface acoustic waves in high temperature (T>=700°C) environments. However, its performance depends on the reflectivities of the reference reflection, the fibre coatings, and the packaging material of the fibre coupler. Therefore, it is not suitable to be employed in contaminative and low reflectivity environments.

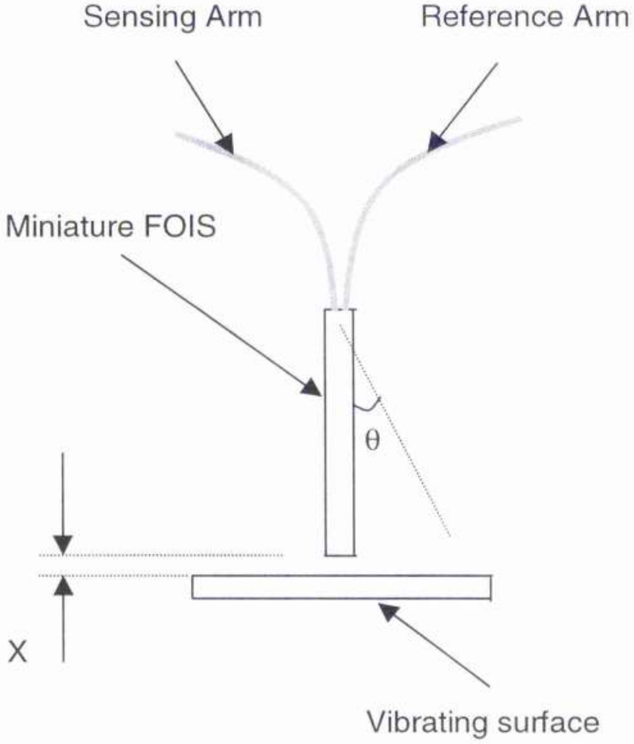

Figure 2 - 7 Details of Michelson-type Interferometer Experiment Setup of SAW Detection

Fibre-optic Fabry-Perot-type interferometric sensors can also involve the extrinsic type of sensor.

In general, the tilt of the reflection surface in the classic bulk Fabry-Perot interferometer or etalon will make the light beam off normal and, as a result, cause the loss of light power. The loss increases with an increase in the length of interferometric cavity. Therefore, it is difficult to construct long-distance bulk Fabry-Perot interferometers. On the contrary, due to the capability of optical fibres to trap light, it is much easier to fabricate the fibre-optic Fabry-Perot extrinsic sensor than to build the traditional bulk Fabry-Perot interferometer.

A fibre-optic Fabry-Perot extrinsic interferometric sensor is schematically shown in Figure 2 - 8. The sensing Fabry-Perot cavity of the sensor is formed by two lengths of single mode fibre, a cleaved end of lead-in fibre and a cleaved end of a short section of reflected fibre. The endface of the reflected fibre is coated with thin high-reflection layer to form a mirror. Both fibres, are held within a sheath by a small gap. A temperature resolution of 0.001°C was proved for the type of the extrinsic sensor [24].

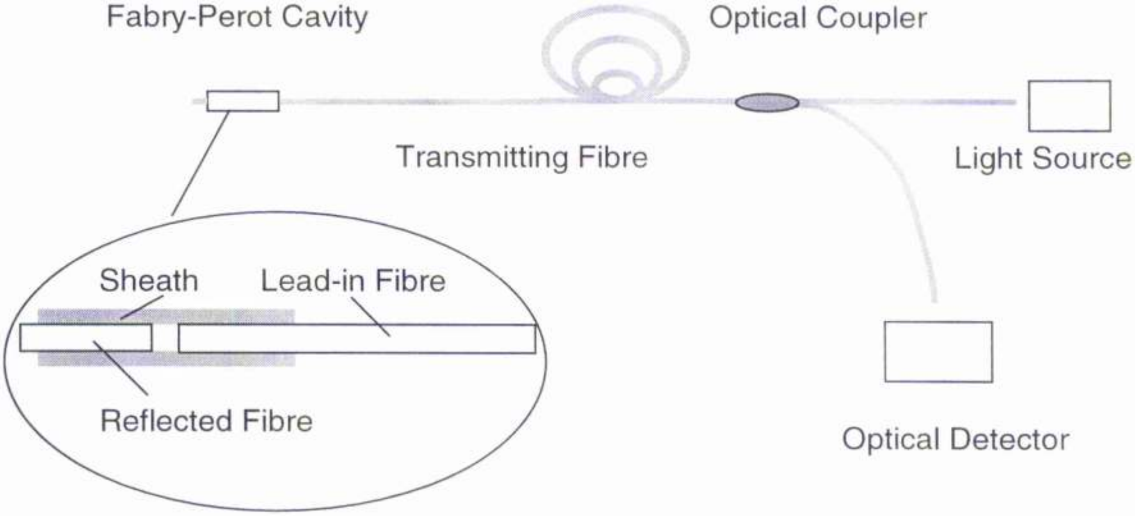

Figure 2 - 8 Schematic of the Fibre-optic Fabry-Perot-type Extrinsic Interferometric Sensor

Compared with the fibre-optic Fabry-Perot intrinsic interferometric sensor, the extrinsic sensor avoids the defects discussed in section 2.31. Another advantage of the extrinsic sensor is that the Fabry-Perot cavity of the extrinsic sensor is much shorter than that of the intrinsic sensor so that the thermal stability of the extrinsic sensor was strengthened.

§2.33 Single Crystal Fibre Sensors

Single crystal fibre is a new kind of functional material with high performance such as high strength, high transparent to light, etc and has been widely used in fibre optic sensors, laser materials and nonlinear optic devices [25,26,27]. Al_2O_3 fibre optic sensors are the most successful application of single crystal fibre, which possesses extraordinary properties such as high temperature resistant, anti-radiation, and chemical erosion resistant, etc. which can not be achieved by conventional devices. Many kinds of single crystal Al_2O_3 fibre sensors were presented during the past twenty years based on the different theories, such as sapphire fibre thermometers, sapphire fibre Fabry-Perot sensors, single-crystal ruby fibres for fluorescence-based sensors, etc.

§2.33.1 Blackbody Radiant Emission Sensors

The technology to measure the temperature by blackbody radiant emission is the one of the most effective methods under the high temperature. Its basic principles is Plank's theorem, in which the radiation intensity is temperature dependant. The typical blackbody sensor [8] is composed of three parts: the head of sensor, the transmitting fibres, and optical detector, as shown in Figure 2 - 9. The head of sensor is a blackbody cavity, which is created by coating a thin iridium film on the surface of the sapphire fibre. The Al_2O_3 films on the iridium film are used to protect the metallic films.

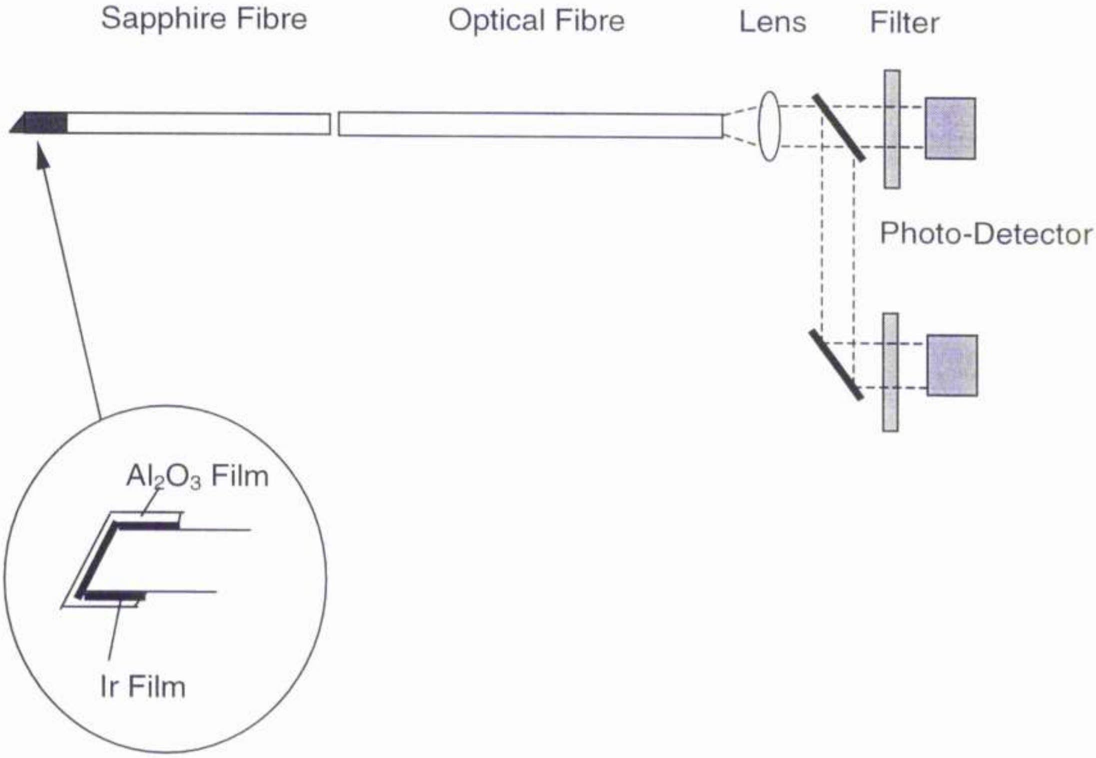

Figure 2 - 9 Schematic of Sapphire Fibre Blackbody Radiant Emission Sensor

The range of temperatures measured by the sapphire fibre blackbody radiant emission sensor is from 600°C to approximately 2000 °C, and it has a high resolution in the high temperature region. However, considering the fact that the radiance intensity distribution is almost exponential form related to temperature, the signal intensity will be so weak during the low temperature field that the output signal of the sensor can hardly be detected. Therefore, it is unsuitable to be used in lower temperature region. In addition, when the metallic film is exposed to high temperatures for a long time, it will volatilize and be oxidized, and the performance of the sensor will decrease quickly. The protective action of the Al_2O_3 film can extend operation. Nevertheless, ceramic materials will be a good choice for the fabrication of blackbody cavities because of their extraordinary chemical stability.

§2.33.2 Fluorescence-Based Temperature Sensors

Since the first fluorescence-based temperature sensor was reported by Sholes in 1980 [28], considerable progress has been made from the biomedical application region to the industrial region in the past decades. The most of investigations on the single-crystal fibre fluorescence-based temperature sensors were focused on the sapphire fibre doped with Cr^{3+} ion sensors in recent years [29,30]. The fluorescence decay time is an exponential distribution and there is a clear corresponding relation between the temperature and the fluorescent lifetime. As a result, the temperature can be estimated by measuring the fluorescence decay time. Generally, there were two different probe structures of the fluorescence-based temperature sensors. The one reported by Gratten, as shown in Figure 2 - 10, consists of three parts [31]: the fluorescent crystal (ruby crystal), the transmitting fibres, and optical detector. The ruby crystal was directly contacted and coupled with the transmitting silica fibre. All the crystal and the silica fibre were protected by a sheath. Apparently, the upper temperature limit of the type of sensor is constrained by the silica fibre and the sheath. Therefore, the second type of probe structure of the sapphire fibre doped with Cr^{3+} ion sensors was developed to overcome the problem above-mentioned, as shown in Figure 2 - 11. The ruby fibre was grown by laser heated pedestal growth for temperature sensing applications in recent years [12]. The integration ruby fibre sensor can withstand temperature near to the melting point 2030°C of the ruby fibre and have a broader measuring temperature region.

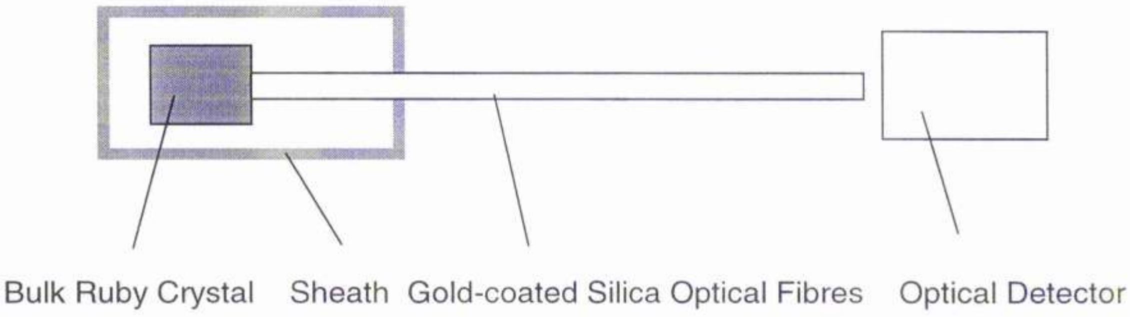

Figure 2 - 10 Schematic of the Ruby Crystal Fluorescence-based Sensor

Figure 2 - 11 Schematic of the Sapphire Fibre Doped with Cr^{3+} Ion Fluorescence-based Sensor

Because the fluorescence lifetime is intrinsic, and thus the lifetime detection will be intensity independent, there will be the long-term stability inherently for the fluorescence-based temperature sensors. In addition, the fabrication of the fluorescence-based temperature sensors in a single fibre will be simple by a single fibre, and the system will also be self-calibrating [32].

However, for the sapphire fibre doped with Cr^{3+} ion sensors, the output of the fluorescence intensity will be affected considerably by the strong background of blackbody radiation under the high temperature. Therefore, the sensor just applied to the range of temperature from room temperature to 600°C [12]. How to improve the situation above-mentioned will be the further research work in the future.

§2.33.3 Intrinsic Sapphire Fibre-optic Fabry-Perot Sensors

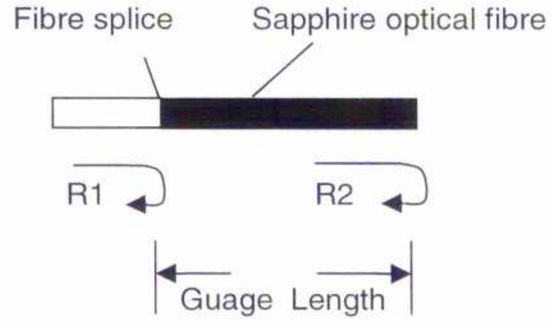

Figure 2 - 12 Schematic of the intrinsic sapphire fibre-based Fabry-Perot interferometer

Apart from those sensors above-discussed, the sapphire fibre-optic Fabry-Perot sensors also were presented in the past ten years. From Figure 2 - 12, a length of multi-mode sapphire fibre is connected by fusion splicing to a single-mode silica fibre to form the FP cavity. A laser beam is launched into the single-mode silica fibre and propagates to the sapphire fibre. Owing to the difference in the refractive index between the silica and sapphire fibres, part of the incident laser power is reflected. The light transmitted into the sapphire fibre excites propagation modes. The propagating light in the sapphire fibre is reflected at the free endface in air. A metal film with a high melting point may be deposited onto the free end face of the fibre to increase the reflection of light. The interference of the two reflections gives rises to the interference fringe output. Since the optical phase of the light travelling in this sapphire fibre is highly sensitive to temperature and longitudinal strain, intrinsic fibre Fabry-Perot interferometric (IFPI) sensors are currently used to measure temperature and these parameters [10].

However, this arrangement lacks flexibility in the control over gauge length, and another possible problem for long-term operation of the sensor is the degradation caused by oxidation of its deposited film at high temperatures.

§2.33.4 Extrinsic Sapphire Fibre-optic Fabry-Perot Sensors

Figure 2 - 13 is the sketch of extrinsic sapphire fibre-based Fabry-Perot interferometer [11].

The extrinsic Fabry-Perot interferometric (EFPI) optical fibre sensors consist of two optical fibres, a reference fibre with two polished endfaces and a reflector fibre with one polished endface enclosing a low-finesse cavity inside a sapphire capillary. The other end of the reflector fibre is left unfinished to prevent secondary reflections. The propagating light in the sapphire fibre is partially reflected at the first sapphire/air interface. Transmitted light projects onto the endface of the second sapphire fibre and is also partially reflected at the air/sapphire interface. Interference between those two reflected waves will happen. Such sensors are used in axial strain and temperature measurement.

The main advantages of EFPI over the IFPI are the avoidance of polarization problems, and the detection of axial strain components only. EFPI is more suitable than IFPI fibre sensor and other electromechanical sensors to monitor material and structure health in both embedded and surface-mounted configurations.

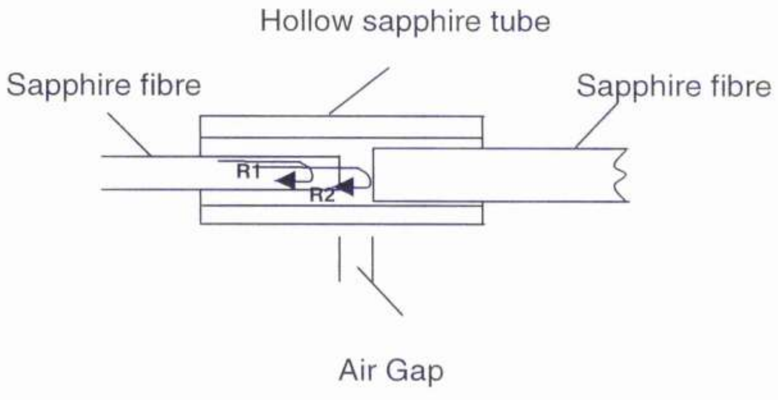

Figure 2 – 13 Sketch of the extrinsic sapphire fibre-based Fabry-Perot interferometer

§2.33.5 Monolithic Sapphire Fibre-optic Fabry-Perot Acoustic Waves and Pressure Sensors

To simplify the design of EFPI sensor, one can conceive a new design of Fabry-Perot high temperature sensor to test pressure and acoustic waves. Figure 2 – 14 shows its scheme of structure.

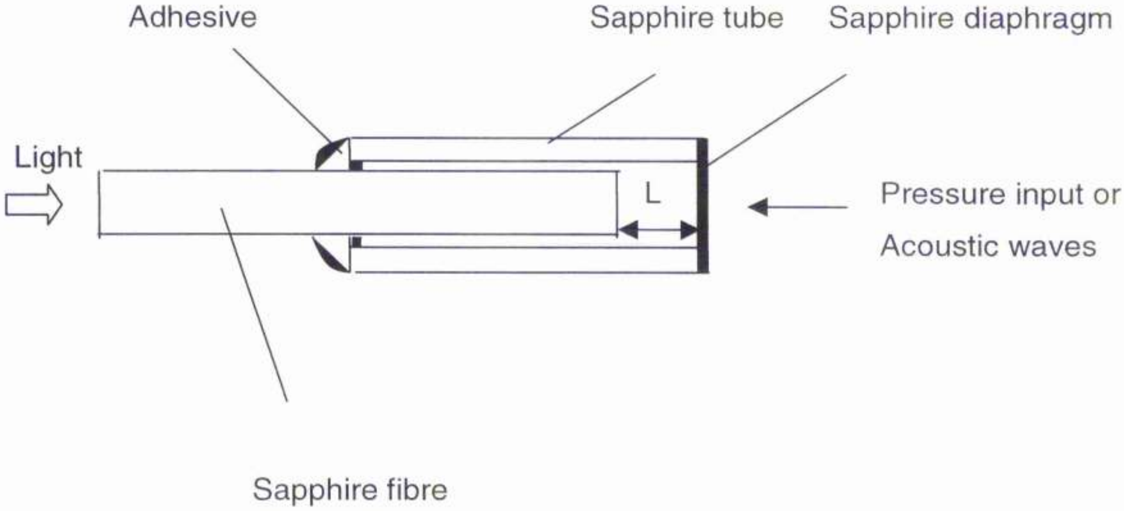

Figure 2 – 14 Schematic diagram of pressure and acoustic waves sensor heads

The sensing cavity is formed between the polished endface of a sapphire fibre and the surface of a very thin sapphire diaphragm. The light from the broadband source is coupled into the lead-in sapphire fibre. It is partly reflected at the first sapphire-air boundary. The transmitted light travels through the air gap and is also partially reflected at the surface of sapphire diaphragm. An interference signal is generated by these two reflected waves and the phase difference depends on the length of air gap, L. Consequently, the acoustic waves and pressure signal will be detected if we choose a suitable signal processing method.

§3 Experimental Design and Results

§3.1 Wedge interferometer

As far as the Fabry-Perot cavity formed by the air-sapphire interfaces at the fibre endfaces, the minute tilt of the reflection surfaces will make the light beam off normal, as a result, cause the loss of light power, and the fringes of the sensor output will decrease highly. Therefore, this is a key problem in fabricating the Fabry-Perot cavity. The goal of this experiment is to establish a procedure to monitor the process of fabrication of a Fabry-Perot cavity in the future work.

In this experiment, the angle of a wedge-shaped air gap between two slightly inclined optical flats was investigated as a function of separation. The angle of a wedge-shaped sheet of glass was calibrated by this method.

Two methodologies were used to check the consistency:

A. Measuring the separation of the interference fringes to calculate the wedge angle (MIF)

B. Direct calculation by measuring tho thickness of the separating shim (DC)

§3.11 Functional relationship between the angle of wedge-shaped air gap and the separation of consecutive fringes of equal thickness (MIF)

For a thin wedge of small angle α, the optical path-length difference (O.P.D) between two reflected rays may be approximated by Eq. (3 -1) [20]:

$$OPD = 2n_f d\cos(r) \qquad (3-1)$$

where *r* is the angle of refraction of the beam, *d* is the thickness at a particular point, n_f is the refractive index, which light spreads in the medium, as Figure 3 – 1 is shown, that is,

$$d = x\alpha_{MIF} \qquad \text{if} \quad \alpha_{MIF} << 1 \qquad (3-2)$$

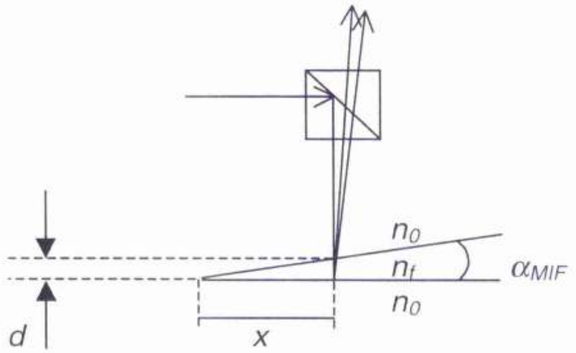

Figure 3 – 1 Fringes from a wedge-shaped thin plate

Therefore, we have:

$$OPD = 2n_f d\cos(r) = 2d\sqrt{n_f^{\ 2} - n_0^2\sin^2(i)} \qquad (3-3)$$

where i is the incident angle of the ray. n_f and n_0 are the refractive indexes, respectively which light spreads in the different medium.

For an interference maximum,

$$(m+\frac{1}{2})\lambda_0 = 2n_f d_m\cos(r) = 2n_f x_m \alpha_{MIF}\cos(r) \qquad (3-4)$$

Therefore, the separation of two consecutive fringes is,

$$\Delta x = x_{m+1} - x_m = \left(\frac{(m+1)+\frac{1}{2}}{2n_f\alpha_{MIF}\cos(r)}\right)\lambda_0 - \left(\frac{m+\frac{1}{2}}{2n_f\alpha_{MIF}\cos(r)}\right)\lambda_0 = \frac{\lambda_0}{2n_f\alpha_{MIF}\cos(r)} \qquad (3-5)$$

Finally, we have

$$\alpha_{MIF} = \frac{\lambda_0}{\Delta x 2n_f\cos(r)} \qquad (3-6)$$

or, in degrees:

$$\alpha_{MIF} = \frac{360^{\circ}}{2\pi} \times \frac{\lambda_0}{\Delta x 2 n_j \cos(r)} \qquad (3-7)$$

Obviously, if the width of two consecutive fringes of equal thickness, Δx, is measured, the angle of wedge could also be calculated exactly.

§3.12 Experimental Design

The schematic of this experiment is shown in Figure 3 – 2. In this experiment, light from a HeNe laser with wavelength 632.8nm passed through a spatial filter with 25 μm diameter of pinhole. It is then divided by a beam splitter, and then incident on the surface of optical flats. The two flats have the same thickness of 13.56mm and diameter of 25.72mm (fabricated by Edmund Industrial Optics) and are laid together with a thin strip of A4 paper along one edge and bound tightly by adhesive tape so as to obtain a wedge-shaped film of air. The optical flats were then fixed on the angle vernier by a clamp in order that the incident angle *i* of the laser beam could be adjusted at will. A travelling microscope with vernier scale was used to measure the separation of consecutive interference fringes of equal thickness produced by the two reflected beams from the two surfaces of wedge-shaped air gap.

The quality of the interference pattern depends on the coherence of light. There are large varieties in the choice of appropriate laser sources. He-Ne laser (λ = 632.8 nm) is a very good selection as a source for it is inexpensive, stable, and emits continuously in comparison with other laser sources. The coherence length of the laser is expressed by [33]

$$L \cong \frac{\lambda^2}{\Delta\lambda} \qquad (3-8)$$

where, $\Delta\lambda \approx 10^{-7}$ Å, and is the linewidth of He-Ne Laser.

So, the coherence length of He-Ne Laser is

$$L \cong \frac{6328^2}{10^{-7}} \times 10^{-10}\, m \approx 4.00 \times 10^4\, m$$

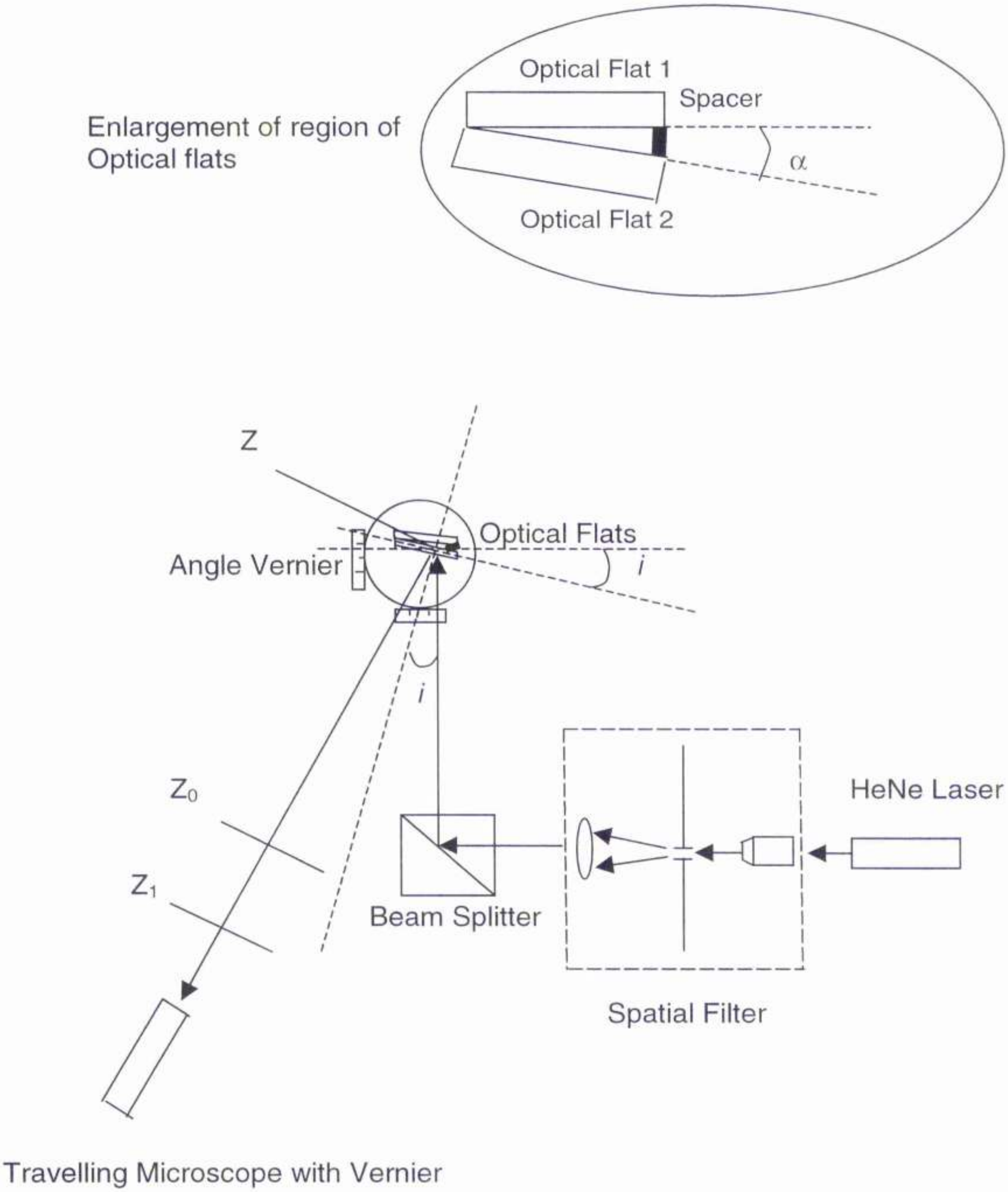

Figure 3 – 2 Schematic of the Wedge interferometer

§3.13 The acquirement of wedged film of air and the calculation of its angle (DC)

§3.13.1 The acquirement of wedged film of air and the calculation of angle of wedged film of air

A thin air wedge was fabricated using the two optical flats according to the method above-mentioned, where the strip of paper was tailored rectangle shape with the 4.1 mm width, as is shown in Figure 3 – 3.

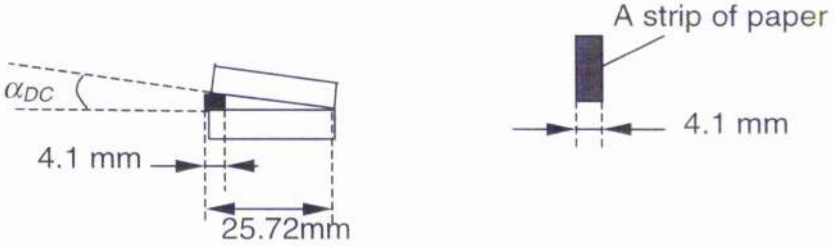

Figure 3 – 3 Schematic of wedged film of air

A screw micrometer was used to measure the thickness of the paper, *d*, according to the method shown in Figure 3 – 4.

The overall thickness d_1 was equal to 27.19 mm, and that the thickness of optical flat d_2 is 13.56 mm. As a result, the thickness of A4 paper

$$d = d_1 - 2d_2 = d_1 - 2\times 13.56 = 27.19 - 27.12 = 0.07mm$$

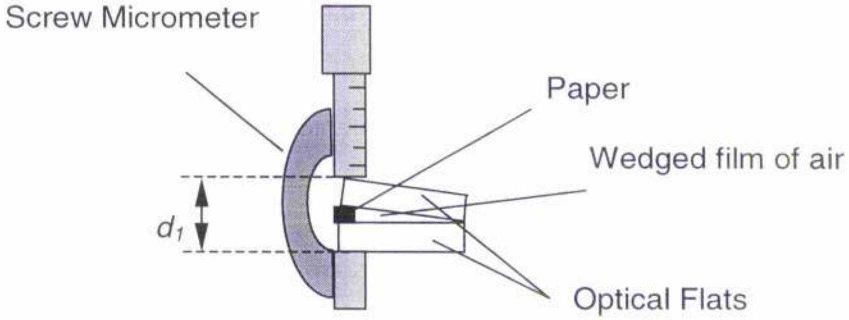

Figure 3 – 4 the measurement of thickness of A4 paper

As it is shown in Figure 3 – 3, we have the angle of wedged film of air

$$\alpha_{DC} \approx \frac{d}{25.72-4.1} \approx \frac{0.07}{21.62} \approx 3.24\times10^{-3}\,radian$$

§3.13.2 Angle Vernier

The Angle Vernier was not only used to acquire the necessary incident angle of the laser beam *i*, but also to control the angle of the reflected light from surface of optical flat. As a result, the background noise caused by that reflected light could be decreased considerably.

§3.13.3 Travelling Microscope with Vernier

Generally, the interference fringes produced by the reflected beams from the two surfaces of wedge-shaped air film are so small that they can hardly be distinguished by naked eyes. Thus, a travelling microscope with vernier scale was used to observe the interference fringes and measure the separation of consecutive interference fringes of equal thickness.

§3.13.4 The measurement and calculation of the separation of consecutive fringes of equal thickness

Since the resulting fringes are formed in the thin film itself (position Z shown in Figure 3 - 2) and the fringe pattern is diverging, the separation of consecutive fringes of equal thickness we measure at position Z_0 or Z_1 is unlikely to be equal to the width of consecutive fringes of equal thickness at position Z. Thus the method of triangle formula was introduced to calculate the separation of consecutive fringes of equal thickness at position Z, as is shown in Figure 3 – 5.

we have assumed that the true width of consecutive fringes of equal thickness is ΔX_Z at position Z, the separation of consecutive fringes of equal thickness is ΔX_{Z0} at the position Z_0, and the separation of consecutive fringes of equal thickness is ΔX_{Z1} at the position Z_1, as a result, we have

$$\frac{\Delta X_Z}{\Delta X_{Z0}} = \frac{m}{m + L_0} \qquad (3-9)$$

$$\frac{\Delta X_{Z0}}{\Delta X_{Z1}} = \frac{m + L_0}{m + L_0 + a} \qquad (3-10)$$

Combined formula (3 – 9) with (3 – 10) above-mentioned, that is

$$m + L_0 = L_0\left(\frac{\Delta X_{Z0}}{\Delta X_{Z0} - \Delta X_Z}\right) \qquad (3-11)$$

Therefore, the true width of consecutive fringes of equal thickness

$$\Delta X_Z = \Delta X_{Z0}\left(1 - \frac{\left(1 - \frac{\Delta X_{Z0}}{\Delta X_{Z1}}\right)L_0}{a \times \frac{\Delta X_{Z0}}{\Delta X_{Z1}}}\right) \qquad (3-12)$$

where,

L_0 is the distance from position Z_0 to position Z (the air film)

and a is the distance between position Z_0 and position Z_1

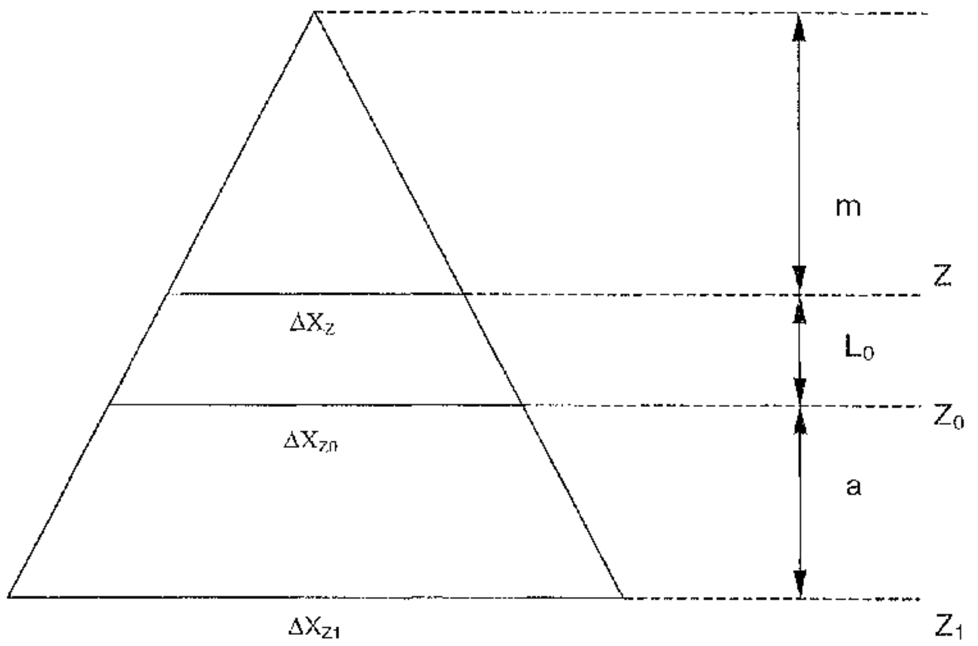

Figure 3 – 5 The calculation of the separation of consecutive fringes of equal thickness

§3.14 Errors and Elimination of Errors

§3.14.1 Percentage Differences of results

From §3.11 and §3.13, the percentage differences between the two different methods can be calculated by

$$PercentageDifference,\% = \left|\frac{\alpha_{MIF} - \alpha_{DC}}{\alpha_{DC}}\right| \times 100\% \qquad (3-13)$$

§3.14.2 Errors and Elimination of Errors

i) Error of Angle of Incident Light

From formula (3 – 3), a change in the angle of incident light, *i*, will cause a variation in the angle of refracted light, *r*, because the relationship between the angle of incident light, *i*, and the angle of refracted light, *r*, is

$$n_f \sin(i) = n_0 \sin(r) \qquad (3-14)$$

Therefore, the original position of incident light should be determined at the beginning of experiment, as it is shown in Figure 3 – 6. That is, the angle vernier should be turned carefully to make the reflected light from the optical flat coincide with the incident light. As a result, the angle of incident light, *i*, at this time is zero. Thus the Error of Angle of Incident Light can be eliminated.

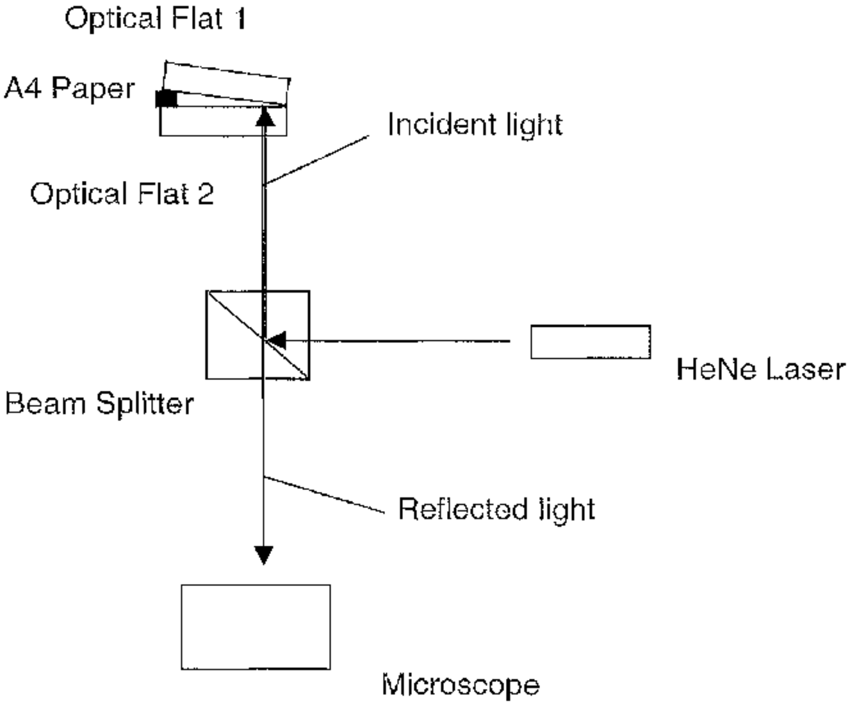

Figure 3 – 6 The Sketch of Original Angle of Incident Light

ii) Error of Position

Limited by the setup itself, the distance L_0 and a, in fact, could not be measured exactly because of the error in estimating the position *Z*, as is shown in

Figure 3 – 2 and Figure 3 – 5. The position Z_0, therefore, should be determined first. Thus the distance *a* could be chosen to suit.

iii) Error of Quality of Interference Pattern

Obviously, the unclear nature of the edge of interference fringes will produce the different values of separation of interference fringes. Hence the method of mean values was introduced to allow for this error. That is,

$$\overline{\Delta X_{Z_i}} = \frac{\sum_{i}^{n} \Delta X_{Z_i}^{n}}{n} \qquad (3-15)$$

where,

$\Delta X_{Z_i}^{n}$ is the separation of consecutive fringes measured at position Z_i, i = 1, 2.

n is the numbers of consecutive fringes measured.

$\overline{\Delta X_{Z_i}}$ is the mean of separation of consecutive fringes at position Z_i.

A spatial filter was employed to improve the quality of the interference pattern. In addition, the background noise caused by spurious reflected light could be significantly decreased when the angle vernier was used to adjust the angle of incident light.

iv) Error of Instruments

Generally, these types of error are due to the limitation of precision and tolerance of instruments. For instance, the travelling microscope gave a precision of ± 0.01 mm.

§3.15 Experimental Results and Discussions

§3.15.1 The Spatial Filter was not used in the setups

The first results were obtained without the use of the spatial filter to give a clear, uniform incident beam.

i) Interference fringes

The fringes, which their edges are obscure, could be observed in the setups shown in Figure 3 - 6 only when the incident beam is almost perpendicular to the surface of optical flat 2. The fringes were observed to die away gradually with the increase of incident angle, and four bright points also are seen finally, which could be the light points reflected from optical flats.

ii) Value of Angle

At position Z_0, only two clear fringes among the group of fringes were visible, we have the separation of fringes:

$$\Delta X^{1}_{Z_0} = 0.65 \text{ mm},$$

$$\Delta X^{2}_{Z_0} = 0.64 \text{ mm},$$

Because parts of the fringes except the clear fringes are unrecognizable, the mean of these separation of fringes:

.

$$\overline{\Delta X_{Z_0}} = \frac{0.65 + 0.64}{2} = 0.645mm$$

At position Z_1, similarly, we have the separation of fringes:

$$\Delta X_{Z_1}^{1} = 0.72 \text{ mm},$$

$$\Delta X_{Z_1}^{2} = 0.73 \text{ mm}.$$

The rest can not be distinguished. So, the mean of separation of fringes is:

$$\overline{\Delta X_{Z_1}} = \frac{0.72 + 0.73}{2} = 0.725mm$$

The distance L_0 between optical flat and Z_0 is equal to 327.04 mm, a between Z_0 and Z_1 is 181.00 mm. All these were measured by long vernier calliper with a precision of ±0.02 mm. Consequently, we have the mean separation of fringes on the film of air gap is

$$\overline{\Delta X_{z}} = \overline{\Delta X_{Z_0}}\left(1 - \frac{\left(1 - \frac{\overline{\Delta X_{Z_0}}}{\overline{\Delta X_{Z_1}}}\right)L_0}{a \times \frac{\overline{\Delta X_{Z_0}}}{\overline{\Delta X_{Z_1}}}}\right) = 0.50mm$$

Considering the equation 3 - 6, the angle of wedge film of air gap is:

$$\alpha_{MIF} = \frac{\lambda_0}{\Delta x 2 n_f \cos(r)} = \frac{632.8\times10^{-9}}{0.50\times10^{-3}\times2\times1\times\cos(0)} = 6.32\times10^{-4}\, radian$$

iii) Percentage Differences of results between the Method of Interference Fringes (MIF) and the Direct Calculated Method (DC)

$$PercentageDifference,\% =$$

$$\left|\frac{\alpha_{MIF}-\alpha_{DC}}{\alpha_{DC}}\right|\times100\% = \frac{-6.32\times10^{-4}+3.24\times10^{-3}}{3.24\times10^{-3}}\times100\% = 80.47\%$$

iv) Discussion

From the results obtained, the separation of fringes calculated by the method of interference fringes has shown the clear difference in comparison with the direct calculated method. The percentage difference of results between the two methods is 80.47%. The inconsistency could be attributed to the following reasons:

a) the incident angle of light beam

Because the incident light beam is almost perpendicular to the surface of the optical flats, all the reflected light from the surfaces of the flats are almost projected to the same areas in the field of view. The interference fringes observed, as a result, could be a type of mixed interference fringes formed by the reflected light from the four surfaces of two optical flats, instead of those only produced by the reflected light from two interfaces of wedge-shaped film of air, as it is shown in Figure 3 - 9.

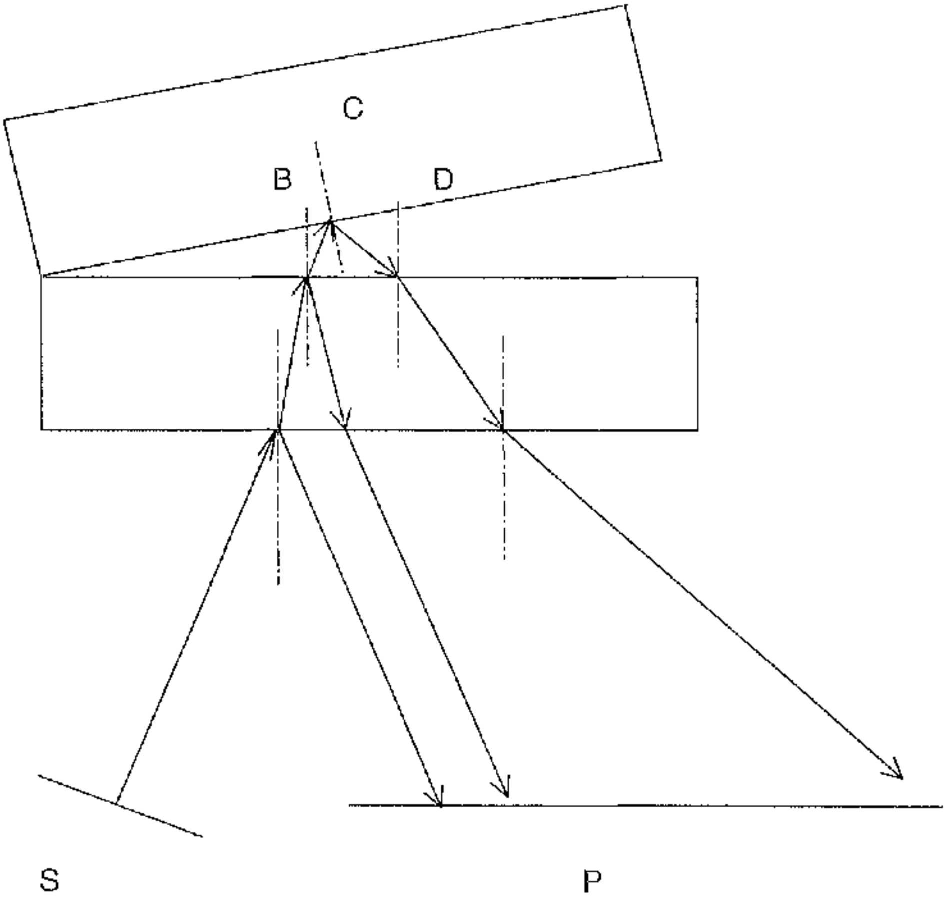

Figure 3 - 9 the mixed interference fringes formed by the reflected light

b) the intensity of light beam

The intensity of light beam is so strong, though part of light had been reflected by beam splitter, that the true interference fringes produced by the reflected light from two interfaces of the wedge-shaped film of air were obscured by the reflected light from other surfaces of optical flat.

§3.15.2 The Spatial Filter was introduced into the setups

To improve the quality of the interference pattern, the spatial filter was introduced.

i) Interference fringes

In comparison to the experiment above-mentioned, the fringes are very clearly observed after using the spatial filter. However, four sets of fringes are seen which interweave each other when the beam is nearly perpendicular to the surface of optical flat, as is shown in Figure 3 - 10. Each fringe set appeared to have the different width. This made fringes unclear. As a result, it is difficult to measure the separation of consecutive interference fringes. In order to eliminate the phenomenom as far as possible, the incident angle of laser beam was adjusted. At incident angle of 20°, the number of fringes sets decreased from four to two, as is shown in Figure 3 - 11. The set with the larger width of fringes was still a little unclear. However, it was clear enough to demarcate the position of the edge of bright and dark fringes visually.

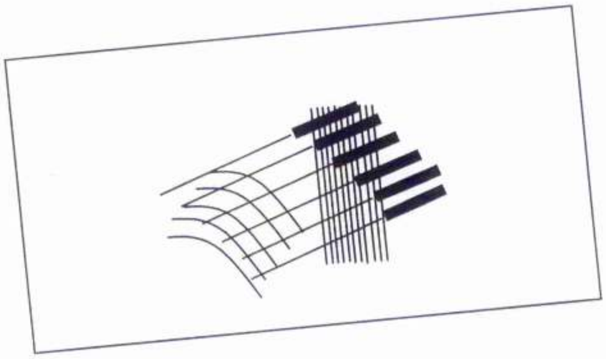

Figure 3 - 10 Sketch of Interference Fringes of Equal Thickness at the incident angle of 0 degree

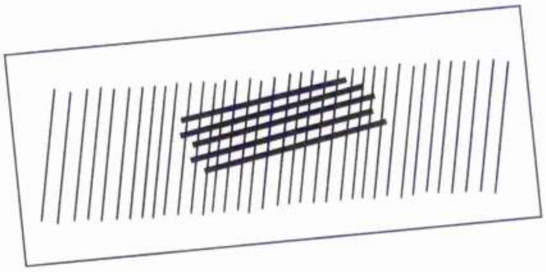

Figure 3 - 11 Sketch of Interference Fringes of Equal Thickness at the incident angle of 20°

ii) Value of Angle

At position Z_0, only two clear fringes among the group of fringes were visible. We have the separation of fringes:

$$\Delta X_{Z_0}^{1} = 0.10 \text{ mm},$$

$$\Delta X_{Z_0}^{2} = 0.10 \text{ mm},$$

Because parts of the fringes except the clear fringes are unrecognizable, the mean of these separation of fringes:

.

$$\overline{\Delta X_{Z_0}} = \frac{0.10+0.10}{2} = 0.10mm$$

At position Z_1, similarly, we have the separation of fringes:

$$\Delta X_{Z_1}^{1} = 0.10 \text{ mm},$$

$$\Delta X_{Z_1}^{2} = 0.10 \text{ mm}.$$

The rest can not be distinguished. So, the mean of separation of fringes is:

$$\overline{\Delta X_{Z_1}} = \frac{0.10+0.10}{2} = 0.10mm$$

The distance L_0 between optical flat and Z_0 is equal to 289.20 mm, the distance a between Z_0 and Z_1 is 113.26 mm. All these were measured by vernier calliper with a precision of ± 0.02 mm. Consequently, we have the mean of separation of fringes on the film of air gap is

$$\overline{\Delta X_Z} = \overline{\Delta X_{Z_0}}\left(1 - \frac{\left(1 - \frac{\overline{\Delta X_{Z_0}}}{\overline{\Delta X_{Z_1}}}\right)L_0}{a \times \frac{\overline{\Delta X_{Z_0}}}{\overline{\Delta X_{Z_1}}}}\right) = 0.10mm$$

Considering the equation 3 - 6, the angle of wedge film of air gap is:

$$\alpha_{MIF} = \frac{\lambda_0}{\Delta x 2 n_i \cos(r)} = \frac{632.8 \times 10^{-9}}{0.10 \times 10^{-3} \times 2 \times 1 \times \cos(20^\circ)} = 3.37 \times 10^{-3}\,radian$$

iii) Percentage Differences of results between the Method of Interference Fringes (MIF) and the Direct Calculated Method (DC)

$$PercentageDifference,\% =$$

$$\left|\frac{\alpha_{MIF} - \alpha_{DC}}{\alpha_{DC}}\right| \times 100\% = \frac{3.37 \times 10^{-3} - 3.24 \times 10^{-3}}{3.24 \times 10^{-3}} \times 100\% = 3.99\%$$

iv) Discussion

What we had observed in the experiment showed that the background noise in the field of view was cut down by the use of spatial filter with a 25 μm diameter pinhole in spite of the remarkable attenuation in power. The edges of the interference fringes were far clearer using a 25μm pinhole than for a 100 μm pinhole, Obviously, the percentage difference of results between the method of interference fringes and the direct calculated method decreased considerably from 80.47% to 3.99% after the spatial filter was introduced into the setups.

However, there are still some other factors except for the errors above-mentioned of which affect the exactness of wedge-shaped angle.

a) optical flat

Theoretically, if the thickness of optical flat is more than the coherence length of source, the interference will not appear caused by the reflected light FP, AP, and EP, as it is shown in Figure 3 - 9, which could result in strong background noise as it was mentioned in above experiment. Therefore, the thicker optical flat should be used to improve the situation in the future if the laser with shorter coherence length is used to replace the HeNe laser at the same time.

b) limitation of the viewing system

Limited by the dimensions of the equipment such as travelling microscope with vernier scale, it is difficult to move the travelling microscope with vernier from position Z_0 to position Z_1 along the same axial line of reflected light, as it is shown in Figure 3 - 2, despite best efforts had been taken. The minute deflection from the axial line could result in the errors of the separation of consecutive interference fringes. It could be the reason why the width of interference fringes observed at position Z_0 was the same as the one observed at position Z_1. Therefore, there is necessary to re-design the viewing system to guarantee that Travelling Microscope with Vernier move along the same axial line of reflected light in the future work.

c) subjective

Estimation of the fringes is, to some extent, subjective. Consequently, the separation of consecutive interference fringes measured by different people will show variations. In view of the fact that the light of laser is extremely dangerous for human eyes, some other methods such as image capture will be considered to eliminate this error in the future.

d) instrument

If the angle of wedge-shaped film of air is so small that the tiny interference fringes could not be discerned by common travelling microscope with vernier scale. A high resolution travelling microscope with vernier scale should be employed to improve this situation. Also, it is a good choice to add some other instruments such as magnifying lens in the viewing system.

In conclusion, it is a good method to detect the angle of wedge-shaped film. Moreover, in consideration of the fact that intialization and setup of the extrinsic Fabry-Perot sapphire fibre sensors could be quite time-consuming, it will also be a potential method to be utilized to fabricate the Fabry-Perot cavity of sensors.

§3.16 The measurement of angle of a wedge-shaped sheet of glass

§3.16.1 Setup

The schematic of this experiment is shown in Figure 3 – 13. In this experiment, a light from a HeNe laser with wavelength 632.8nm was allowed to pass through a Spatial Filter with 100μm diameter of pinhole, be divided by a beam splitter, and then be incident on the surface of glass. The glass was fixed on the Angle Vernier by a clamp in order that the incident angle *i* we need of laser beam could be adjusted. A Travelling Microscope with Vernier was used to measure the separation of consecutive interference fringes of equal thickness produced by the two reflected lights from the two surfaces of wedge-shaped glass.

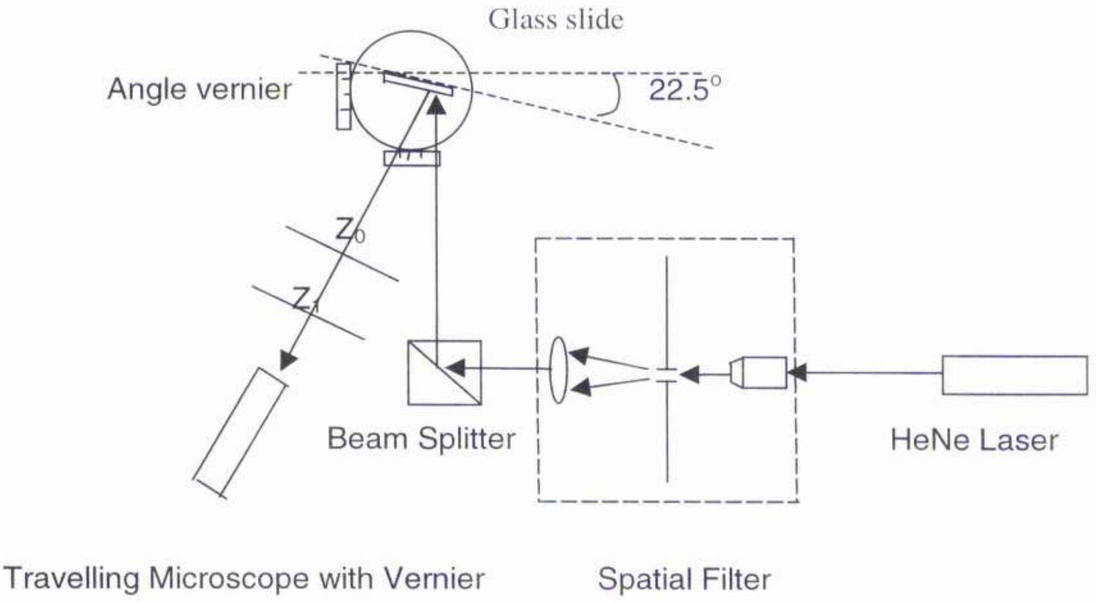

Figure 3 – 13 Schematic of the measurement of angle of a wedge-shaped sheet of glass

§3.16.2 Experimental Results

i) Interference fringes

Two different kinds of fringes could be observed clearly when the incident angle of laser light is about 22.5°, as it is shown in Figure 3 -14. The two kinds of fringes appeared along the glass slide to and fro periodically, which could be caused by the different situation of surfaces of glass. The fringes could hardly be observed when the beam is nearly perpendicular to the surface of glass slide.

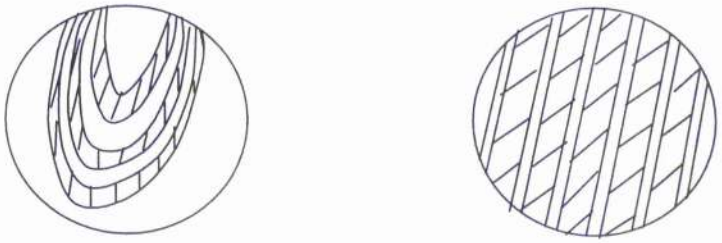

(a) (b)

Figure 3 - 14 Interference Fringes by reflection with surfaces of glass slide

ii) Value of Angle

At position Z_0, we have the separation of fringes:

$$\Delta X_{Z_0}^{1} = 0.29 \text{ mm},$$

$$\Delta X_{Z_0}^{2} = 0.29 \text{ mm},$$

$$\Delta X_{Z_0}^{3} = 0.31 \text{ mm},$$

$$\Delta X_{Z_0}^{4} = 0.28 \text{ mm},$$

Because parts of the fringes except clear fringes are unrecognizable, the mean of these separation of fringes:

$$\overline{\Delta X_{Z_0}} = \frac{0.29 + 0.29 + 0.31 + 0.28}{4} = 0.2925mm$$

At position *Z₁*, similarly, we have the separation of fringes:

$$\Delta X^1_{Z_1} = 0.36 \text{ mm},$$

$$\Delta X^2_{Z_1} = 0.37 \text{ mm}.$$

The rest can not be distinguished. So, the mean of separation of fringes is:

$$\overline{\Delta X_{Z_1}} = \frac{0.36+0.37}{2} = 0.365mm$$

The distance L_0 between Optical flat and Z_0 is equal to 343.38 mm, the distance a between Z_0 and Z_1 is 175.41 mm. All these were measured by vernier caliber. Consequently, we have the mean of separation of fringes is

$$\overline{\Delta X_Z} = \overline{\Delta X_{Z_0}}\left(1 - \frac{\left(1-\frac{\overline{\Delta X_{Z_0}}}{\overline{\Delta X_{Z_1}}}\right)L_0}{a \times \frac{\overline{\Delta X_{Z_0}}}{\overline{\Delta X_{Z_1}}}}\right) = 0.1419mm$$

Considering the equation 3 - 6, the wedge angle of glass is:

$$\alpha = \frac{\lambda_0}{\Delta x 2n_f \cos(r)} = \frac{632.8\times10^{-9}}{0.1419\times10^{-3}\times2\times\sqrt{n_f^2-1\times\sin^2(22.5°)}}$$

$$= \frac{632.8\times10^{-9}}{0.1419\times10^{-3}\times2\times\sqrt{1.52^2-\sin^2(22.5°)}} = 1.52\times10^{-3}\,radian$$

§3.2 Intrinsic Sapphire Fibre-optic Fabry-Perot Sensors

Based on the experiment done in section § 3.1, the aim of the experiment is to establish a procedure which could be exploited to observe the interference fringes from an intrinsic sapphire fibre-optic Fabry-Perot sensor, and to infer the temperature from this signal.

§3.21 Functional relationship between the output of interference signal of intrinsic sapphire fibre-optic Fabry-Perot sensors and temperature

When a length of sapphire fibre is heated from temperature T_1 to temperature T_2, there is a corresponding linear change from V_1 to V_2 in volume. Here, the expansion of single crystal sapphire fibre along the c-axis (across its a-axis) is only considered because the change of sapphire fibre along the a-axis is unrelated to the variation of the optical path difference. Therefore, the coefficient, α_m, of volumetric thermal expansion of the substance on heating from T_1 to T_2 is expressed as [34,35]

$$\alpha_m = \frac{1}{V}\left(\frac{\partial V}{\partial T}\right)_P = \frac{1}{L}\left(\frac{\partial L}{\partial T}\right)_P \qquad (3 - 16)$$

where, *L* is the length of sapphire fibre, *P* means that the thermal expansion is at constant pressure.

Assuming constant atmospheric pressure, we have

$$\alpha_m = \frac{1}{L}\frac{dL}{dT} \qquad (3-17)$$

Generally, the condition for multi-beam interference in parallel plate is

$$2nL\cos\theta = N\lambda \qquad (3-18)$$

where, *n* is the index of refraction of the sapphire between the surfaces, *θ* is the angle between the direction of the incident rays and the perpendicular to the surfaces, *N* is the order of interference, and *λ* is the wavelength of the light in vacuum.

Therefore, differentiating equation 3 -18, we have

$$\frac{dL}{L} = \frac{\lambda}{2nL\cos\theta}dN - \frac{dn}{n} = \frac{dN}{N} - \frac{dn}{n} \qquad (3-19)$$

where, *dN* is the number of interference fringes, and *dn* is the change of refractive index.

Combining equation 3 - 17 with equation 3 - 19, we have

$$\alpha_m dT = \frac{dN}{N} - \frac{dn}{n} \qquad (3 - 20)$$

Obviously, the variation of temperature could be translated into the output of the number of interference fringes. As a result, we could obtain the change in temperature by counting the number of interference fringes with some instruments such as oscilloscope, etc.

§3.22 Experimental Design

Figure 3 - 15 shows the schematic of setup for the experiment. In this experiment, two endfaces of a length of multimode unclad sapphire fibre with a diameter of 425 μm, is polished to form the Fabry-Perot cavity of 70 mm in lengths. Light from a HeNe laser with wavelength 632.8nm passes through a spatial filter with a 25 μm diameter pinhole and is expanded by a beam expander. It is then divided by the first beam splitter which is used to separate the input and output light of the sensor, and then launched by a 10X microscope objective into the multimode sapphire fibre. A special holder, which can adjust the angle easily between the principle axis of the microscope objective and the axis of the sapphire fibre, was used to align the fibre. The soldering iron with ten different temperature settings is used to heat a small length near the end of the sapphire fibre. The interference fringes generated by the two reflections from the interface of air - sapphire and the end face of sapphire - air is divided again by the second

beam splitter into two parts, one of which is processed in the oscilloscope or chart recorder, and another is observed directly by the frame-grabber system which is composed of travelling microscope with vernier scale, JVC digital colour video camera, and computer.

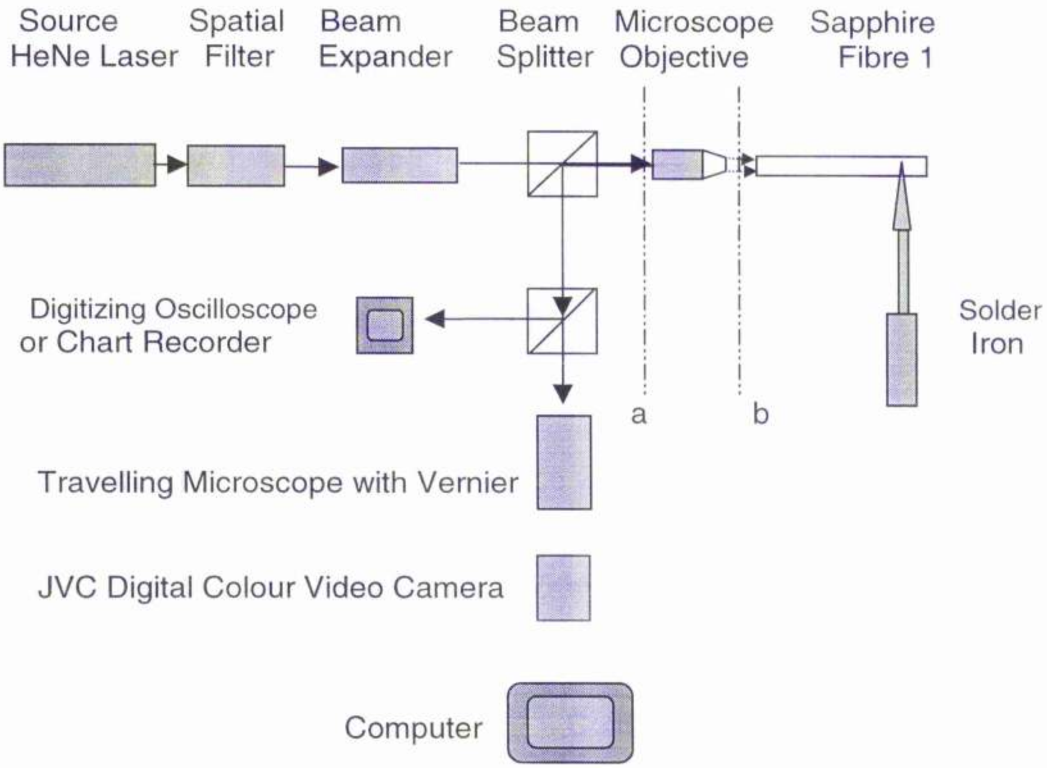

Figure 3 - 15 Schematic of measurement setup of interference fringes from an intrinsic sapphire fibre-optic Fabry-Perot sensor

Considering the fact that the propagating light incident onto the first endface of the sapphire fibre is partially reflected at the first air - sapphire interface, and the light launched into the sapphire fibre is also partially reflected at the endface of the sapphire - air interface, the reflectivity, *R*, at each of the two interfaces is equal to

$$R = \left(\frac{n-1}{n+1} \right)^2 \tag{3 - 21}$$

where, *n* is the index of refraction of the sapphire and equal to 1.763. Therefore, we have

$$R = \left(\frac{n-1}{n+1} \right)^2 = \left(\frac{1.763-1}{1.763+1} \right)^2$$

$$= 7.63\%$$

If we assumed that I_0 is the intensity of the incident light, I_1 is the intensity of the light reflected from the first air - sapphire interface, and I_2 is the intensity of the light transmitted from the first air - sapphire interface with the opposite direction of incident light, which is the light reflected from the endface of the sapphire - air interface, the visibility can be expressed as

$$V_{\text{int}} = \frac{2\sqrt{I_1 \times I_2}}{I_1 + I_2} \tag{3 - 22}$$

where,

$$I_1 = R \times I_0 = 7.63\% \cdot I_0$$

$$\begin{aligned} I_2 &= R(1-R)^2 \times I_0 \\ &= 7.63\% \cdot (1-7.63\%)^2 \cdot I_0 \end{aligned}$$

Therefore, we have

$$V_{\text{int}} = \frac{2\sqrt{I_1 \times I_2}}{I_1 + I_2} = \frac{2 \times 7.63\% \times (1-7.63\%)}{7.63\% + 7.63\%(1-7.63\%)^2} = 99.69\% \approx 1$$

For the intrinsic sapphire fibre-optic Fabry-Perot sensor, the signal received by the detector can be described as

$$I_{\text{int}} = \frac{1}{4}(I_1 + I_2)(1 + V_{\text{int}} \cos\delta) \qquad (3 - 23)$$

Hence, we have

$$\frac{I_{\text{int}}}{I_0} \approx \frac{1}{2}[R + R(1-R)^2]\cos^2(\frac{\delta}{2}) \qquad (3 - 24)$$

As a result,

$$\frac{I_{\text{int}}}{I_0} \approx 7.07\% \cos^2(\frac{\delta}{2})$$

Obviously, the output signal of the intrinsic sapphire fibre-optic Fabry-Perot sensor will be considerably weaker than the intensity of light launched into the sensor though the interference fringes have a good visibility theoretically.

§3.23 Experimental Results and Discussions

i Fringes

From Figure 3 - 16, we could see the two types of interference fringes output of intrinsic sapphire fibre-optic Fabry-Perot sensors, where the circular fringes are generated by the two reflections from the interface of air - sapphire and the end face of sapphire - air, and the straight fringes are produced by the beam splitter. The cross features also were observed which are the flaws on the travelling microscope with vernier scale. The edges of interference fringes are obscure because the two types of interference fringes interweave. If inserting a piece of black paper in front of the microscope objective (position a) or the sapphire fibre (position b), respectively, we see only the straight interference fringes, as is shown in Figure 3 -17, Figure 3 - 18, respectively. To ensure that the circular interference fringes were not produced by the reflections between the surface of microscope objective and the surface of one end of sapphire, a small angle between its axis line and the axis line of microscope objective was made by positioning the sapphire fibre, the circular fringes were still observed and concluded to be due to intrinsic interference in the fibre.

The position of interference fringes was seen to shift with the changes of temperature when the soldering iron was used to heat the end of sapphire fibre, as it is shown in Figure 3 - 19. The background at the centre of the interference fringes changes from darkness to brightness in turns during heating and cooling. The rings of the interference fringes shrink and vanish at the centre ceaselessly because the length of sapphire fibre changes with the rise of the temperature of soldering iron.

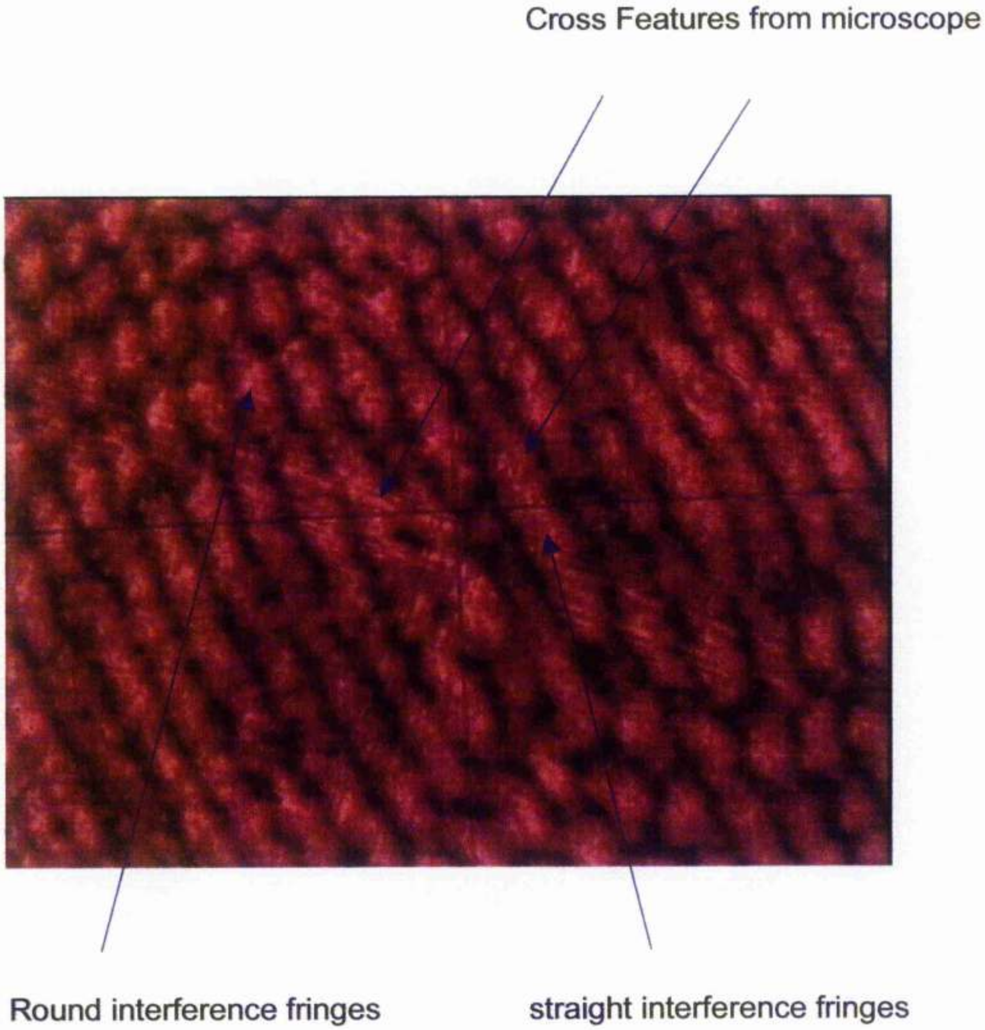

Figure 3 - 16 Interference Fringes From the Intrinsic Sapphire Fibre-optic Fabry-Perot Sensors

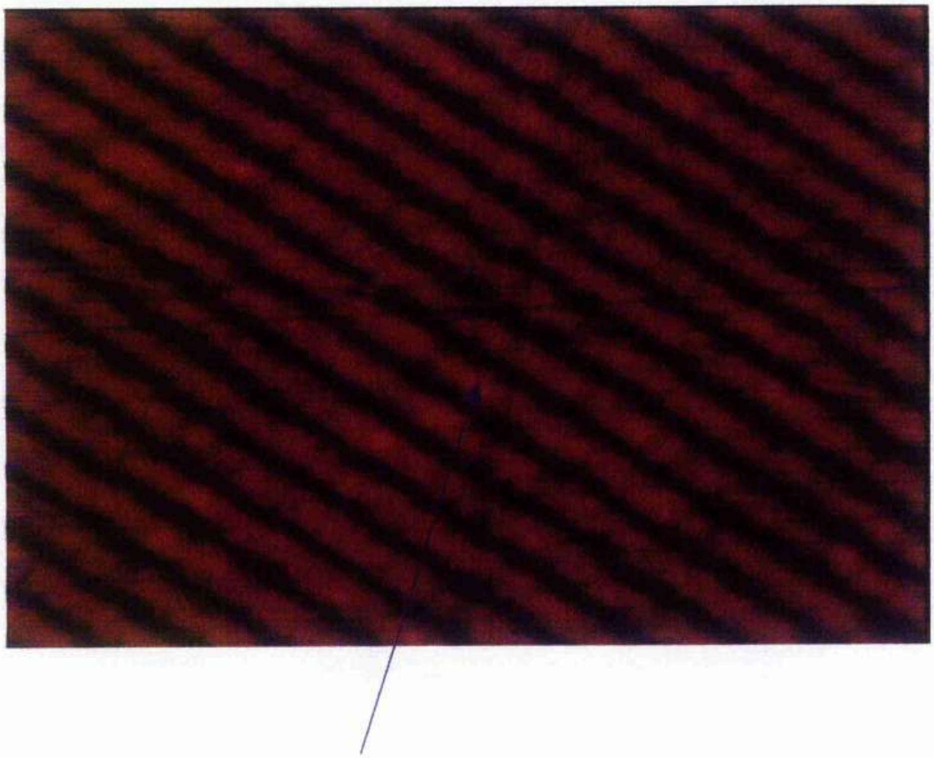

Straight Interference Fringes

Figure 3 - 17 Straight Interference Fringes when a black paper is at Position a

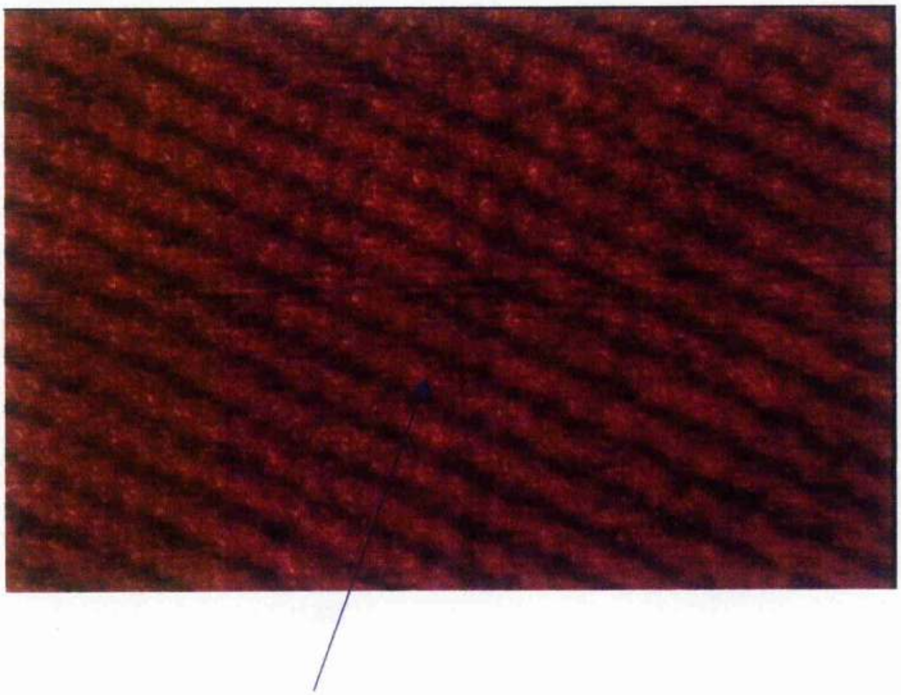

Straight Interference Fringes

Figure 3 - 18 Straight Interference Fringes when A Black Paper is at Position b

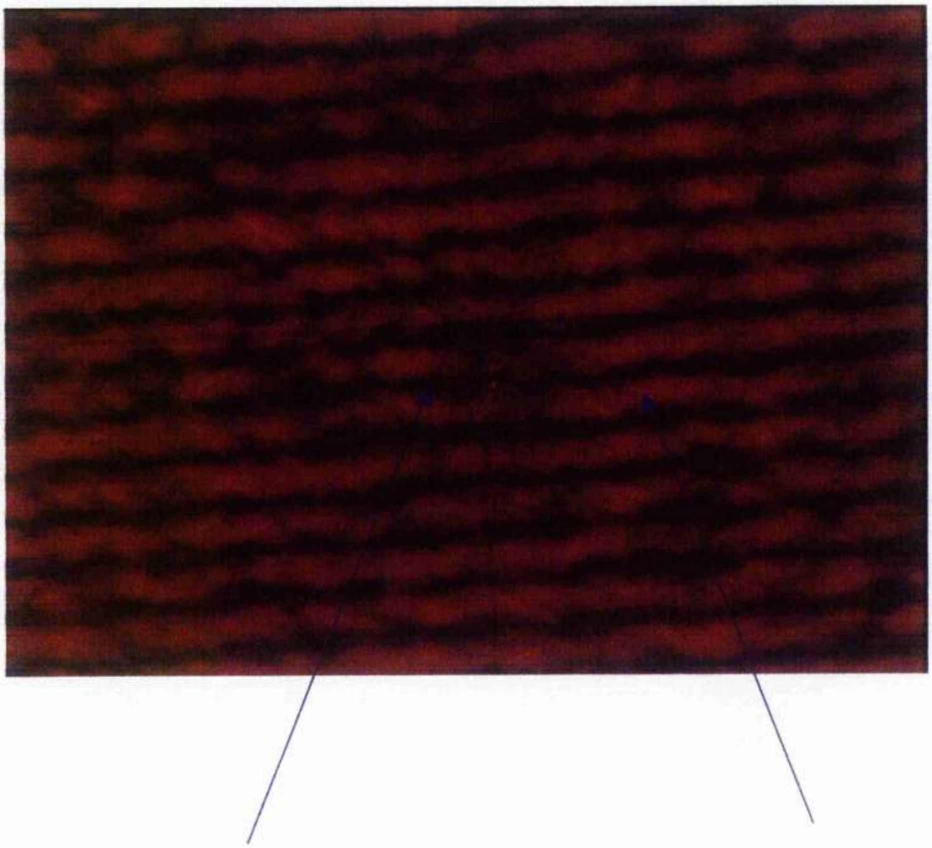

(a) Interference fringes before heating

Figure 3 - 19 The changes of Interference Fringes before heating and during heating

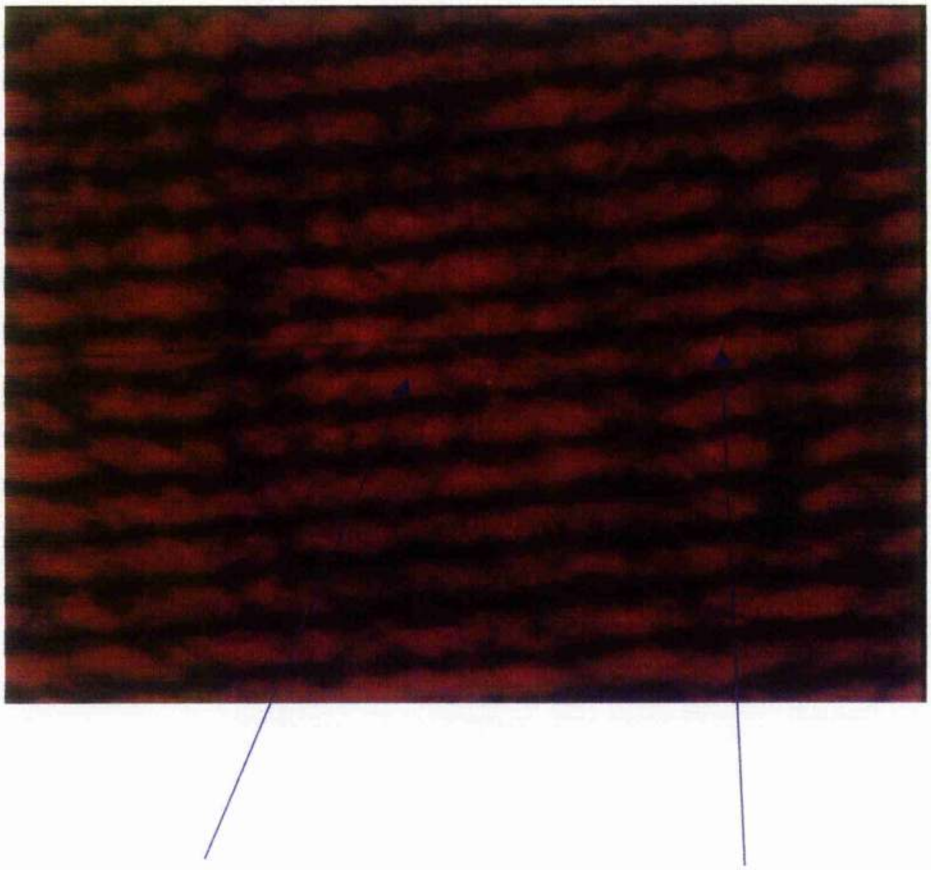

(b) Interference fringes during heating

Figure 3 - 19 The changes of Interference Fringes before heating and during heating

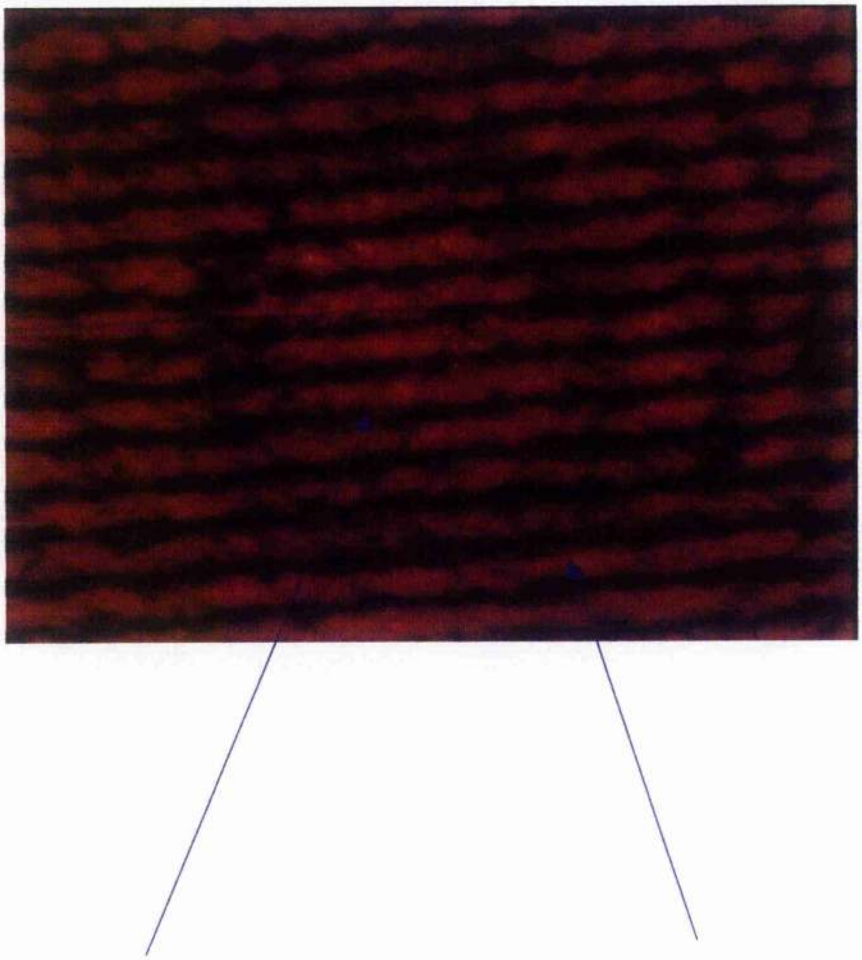

(c) Interference fringes when heating 5 minutes

Figure 3 - 19 The changes of Interference Fringes before heating and during heating

Centre of interference fringes(darkness) round interference fringes

(d) Interference fringes when heating 10 minutes

Figure 3 - 19 The changes of Interference Fringes before heating and during heating

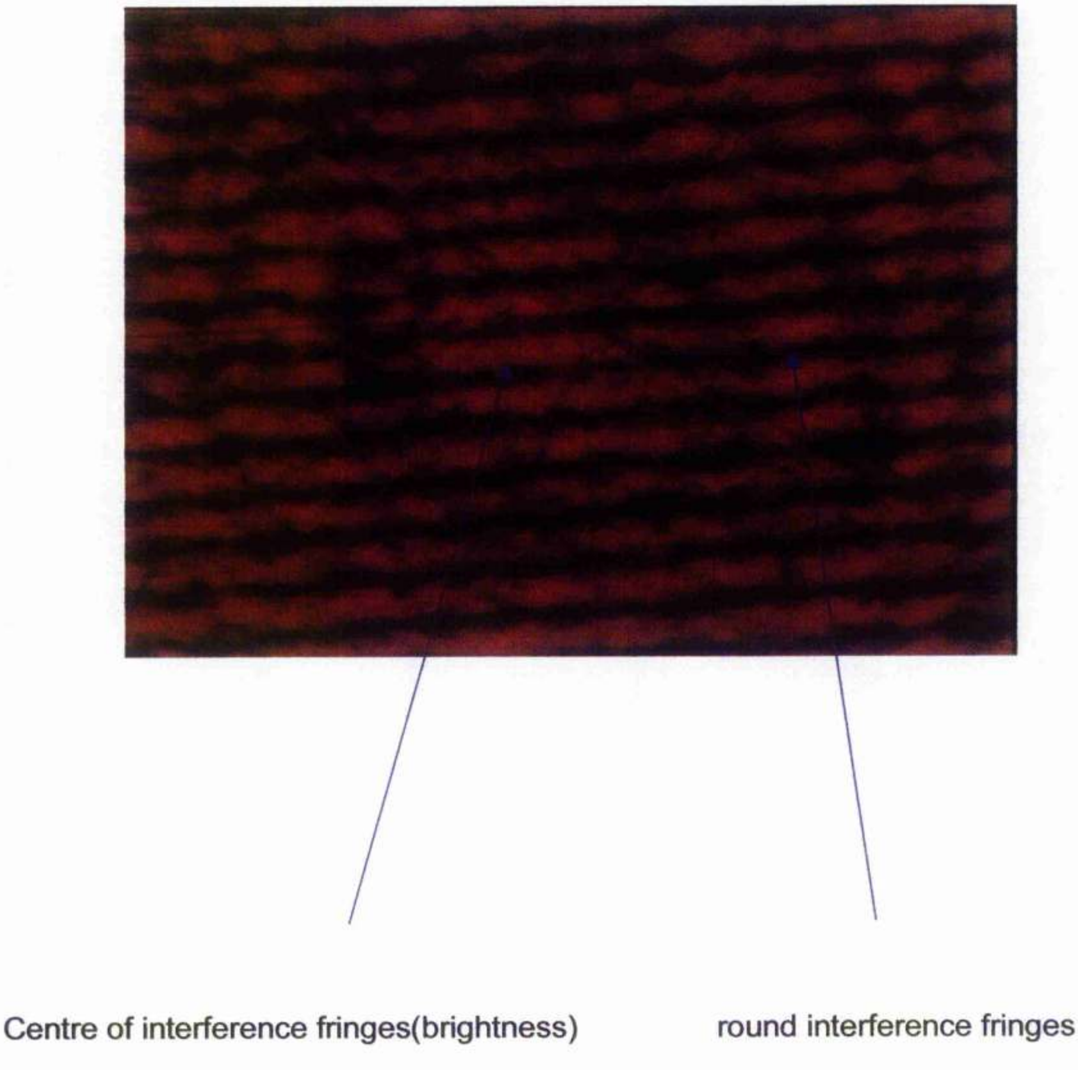

(e) Interference fringes when stopping heating

Figure 3 - 19 The changes of Interference Fringes before heating and during heating

Centre of interference fringes(darkness) round interference fringes

(f) Interference fringes when stopping heating 5 minutes

Figure 3 - 19 The changes of Interference Fringes before heating and during heating

Centre of interference fringes(brightness) round interference fringes

(g) Interference fringes when stopping heating 10 minutes

Figure 3 - 19 The changes of Interference Fringes before heating and during heating

ii Chart

a) Oscilloscope

Also, the changes of interference fringes during heating and cooling could be observed using the oscilloscope, as it is shown in Figure 3 - 20 and Figure 3 - 21.

The output signal varied slowly between 415 mV and 435 mV with the changes of temperature when the end of sapphire fibre was heated by the soldering iron and cooled with the soldering iron.

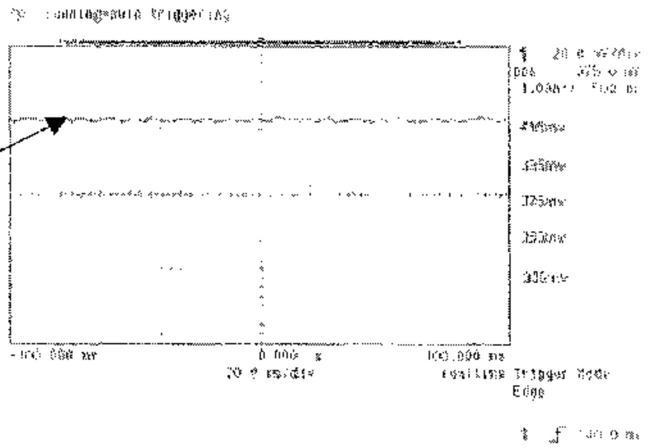

Output signal

(a) Output signal before heating

Figure 3 - 20 The changes of Output signal before heating and during heating

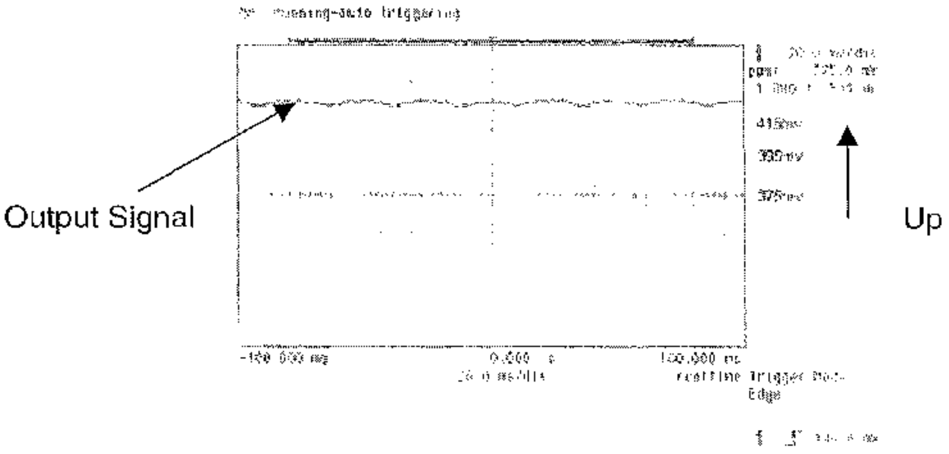

(b) Output signal when heating from room temperature to 70°C (up)

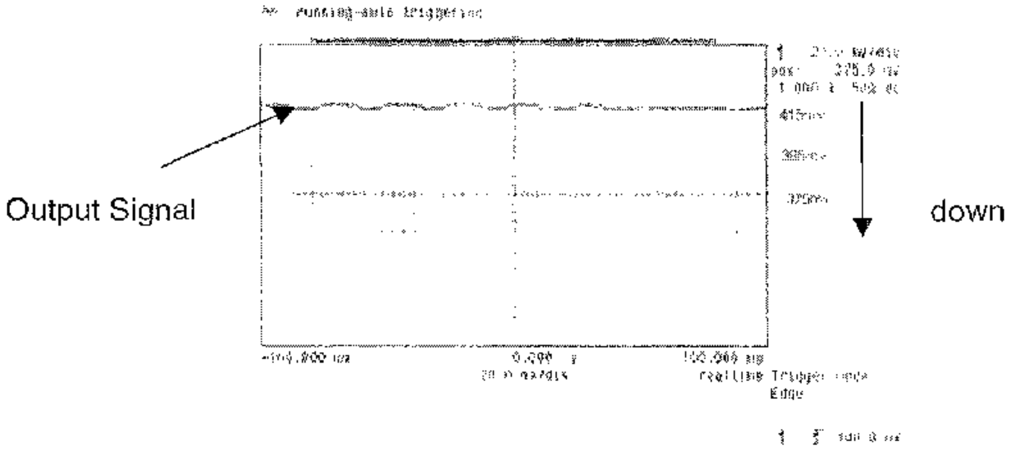

(c) Output signal when heating from room temperature to 245°C (down)

Figure 3 - 20 The changes of Output signal before heating and during heating

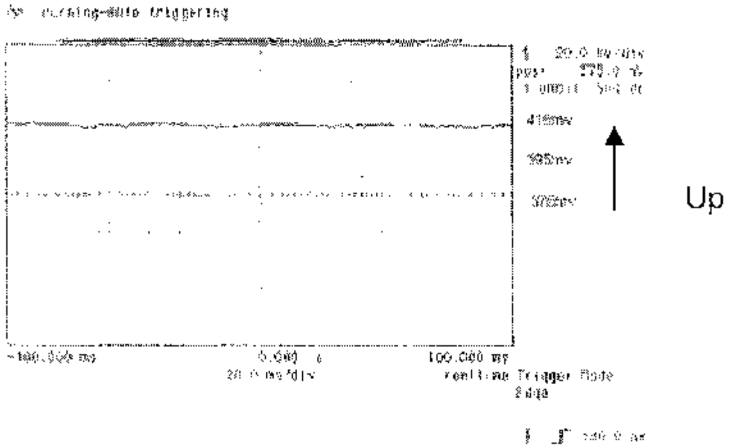

(d) Output signal when heating from room temperature to 365°C (up)

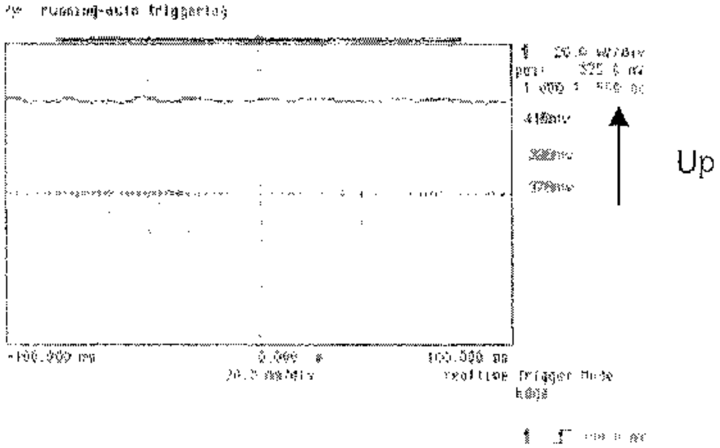

(e) Output signal when heating from room temperature to 365°C and keeping it (1) (up)

Figure 3 - 20 The changes of Output signal before heating and during heating

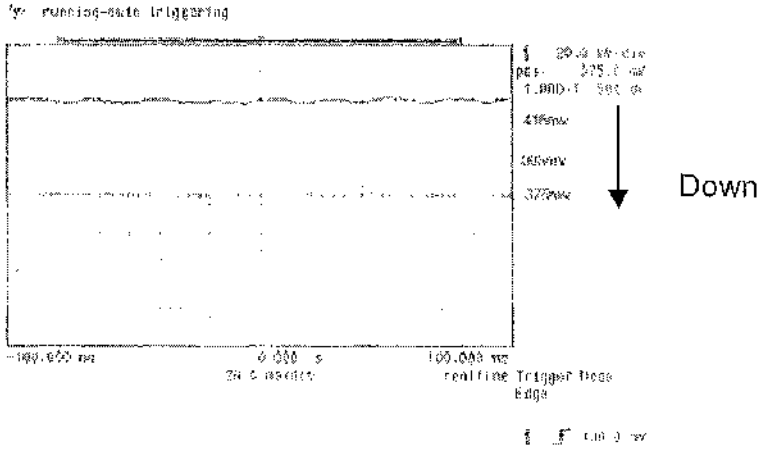

(e) Output signal when heating from room temperature to 365°C and keeping it (2) (down)

Figure 3 - 20 The changes of Output signal before heating and during heating

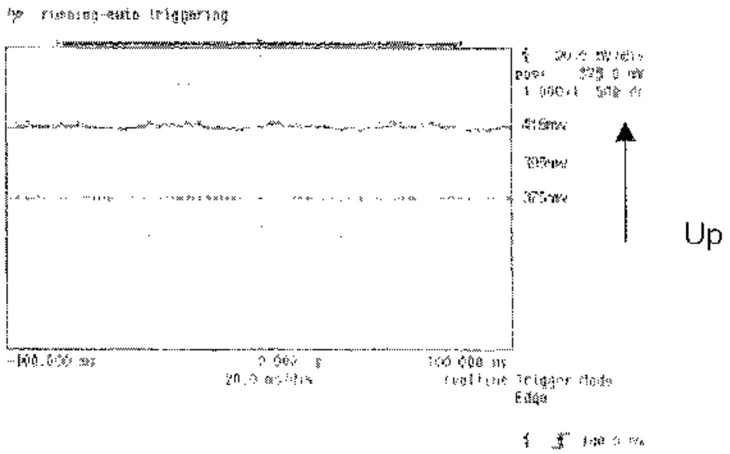

(a) Output signal when cooling for 2 minutes (up)

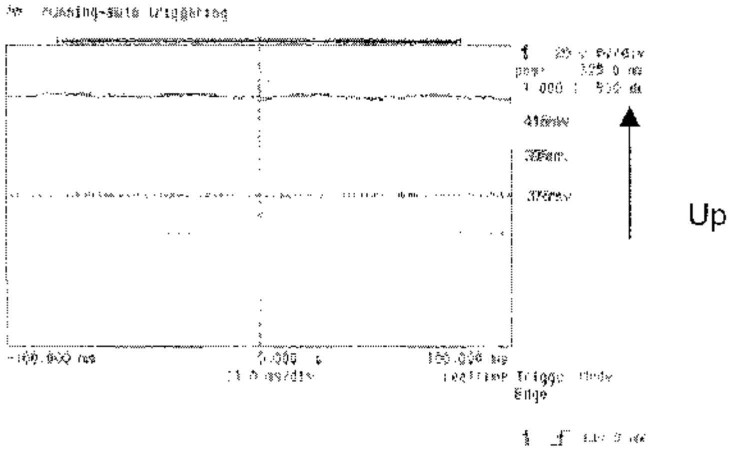

(b) Output signal when cooling for 4 minutes (up)

Figure 3 - 21 The changes of Output signal during cooling

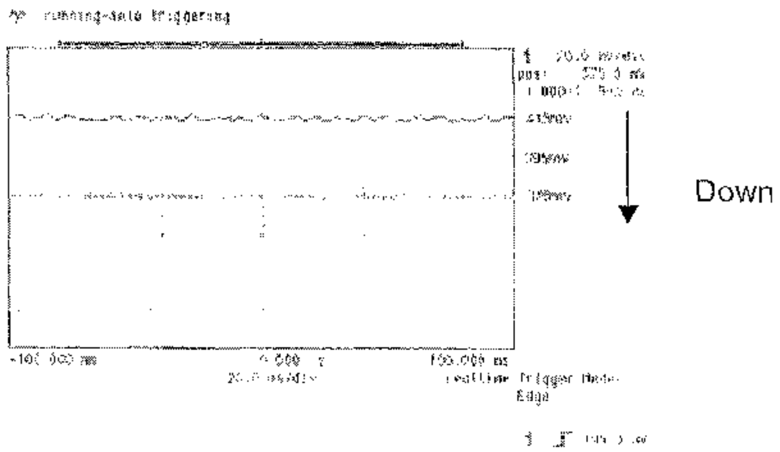

(c) Output signal when cooling for 7 minutes (down)

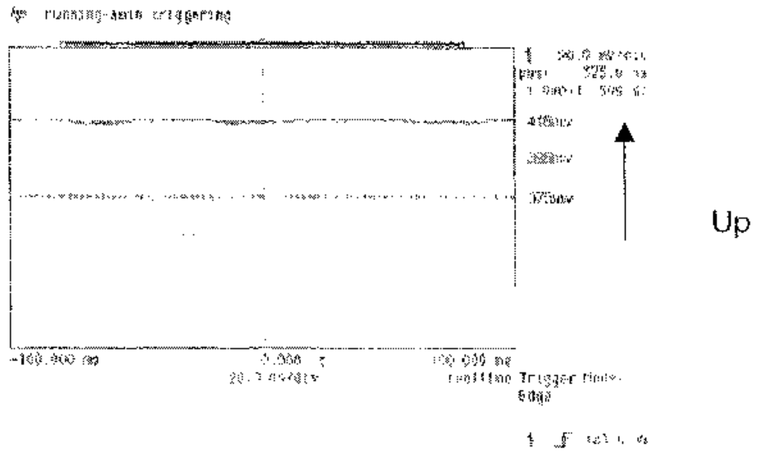

(d) Output signal when cooling for 10 minutes (up)

Figure 3 - 21 The changes of Output signal during cooling

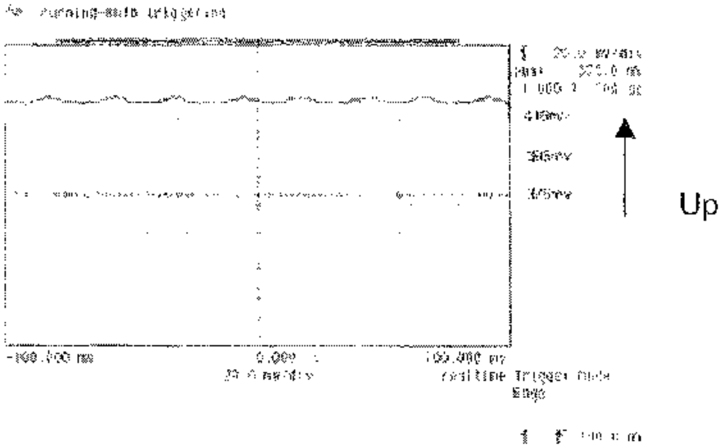

(e) Output signal when cooling for 14 minutes (up)

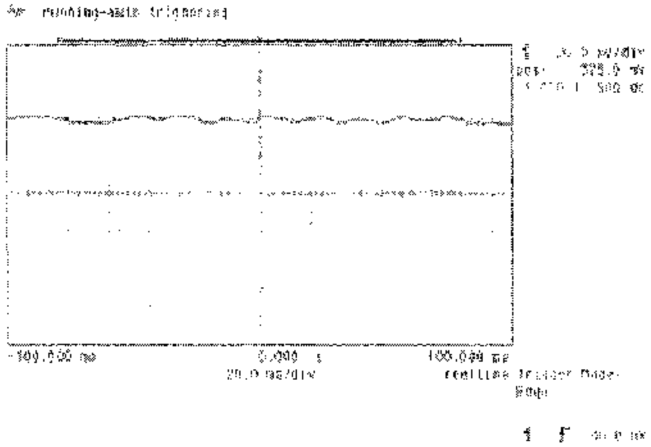

(f) Output signal when cooling for 20 minutes

Figure 3 - 21 The changes of Output signal during cooling

b) Chart Recorder

The chart recorder could clearly draw the changes of intensity of interference fringes from darkness to brightness. Therefore, the optical path-length difference at different environmental temperatures could be obtained by totalizing the maxima or minima of the trace of the interference fringes on the drawing, as it is shown in Figure 3 - 22. The remaining traces of the graphs under the different temperatures can be found in Appendix. Table 1 shows the value of the number of interference fringes under the different temperatures. Thus, we can acquire the fitting equation, the functional relationship between the number of interference fringes of intrinsic sapphire fibre-optic Fabry-Perot sensor and temperature, by data fitting, as it is shown in Figure 3 - 23. A linear output as a function of temperature was obtained for the measurement range of 75 °C - 435 °C. Obviously, as long as we can record the number of interference fringes of intrinsic sapphire fibre-optic Fabry-Perot sensor, we can acquire the corresponding temperature by the fitting equation.

According to the fitting equation, the output of the number of interference fringes when the temperature goes up from room temperature 20 °C to 435 °C should be

$$dN = 0.31x - 26.9$$

$$= 0.31 \times 435 - 26.9 \approx 107$$

Assuming constant atmospheric pressure, the equation 3 -19 will be expressed as

$$\frac{dL}{L} \approx \frac{\lambda}{2nL} dN \tag{3 - 25}$$

Hence, the change of single crystal sapphire fibre along the c-axis is

$$dL \approx \frac{\lambda}{2n} dN \approx \frac{632.8 \times 10^{-9}}{2 \times 1.763} \times 107 \approx 19.2 \mu m$$

Temperature (°C)	75	95	140	195	240	280	330	375	420	435
Fringes Count	2	4	13	31	48	55	73	90	99	117

Table 1 the value of the number of interference fringes under the different temperatures

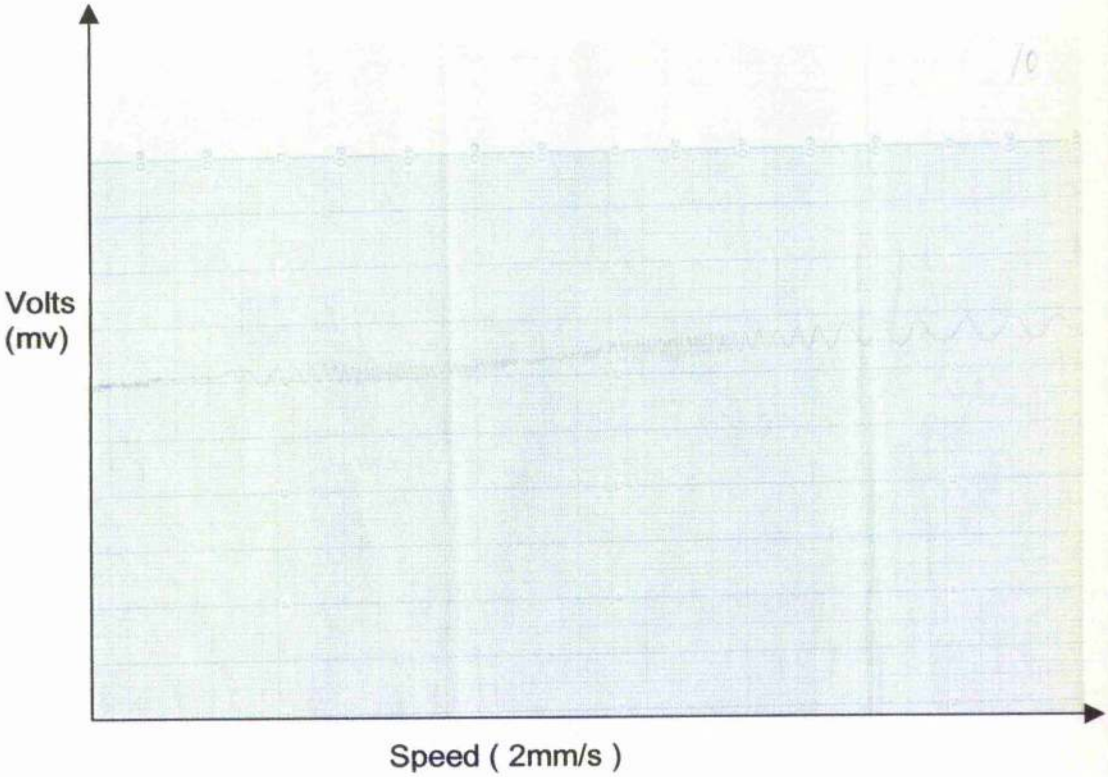

Figure 3 - 22 The output of sensors from the chart record

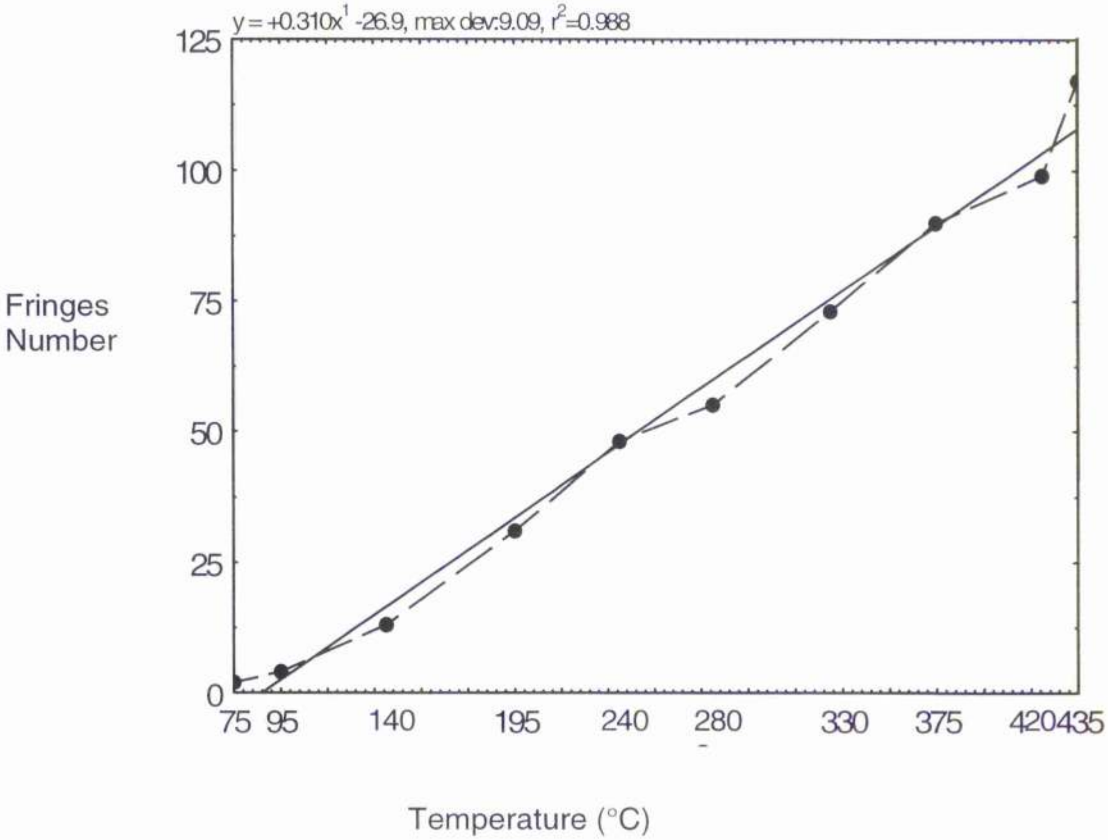

Figure 3 - 23 The output of intrinsic sapphire fibre-optic Fabry-Perot sensors as a function of temperature

iii Discussions

From the results obtained, the poor optical resolution of the travelling microscope with vernier scale and JVC digital colour video camera was not good enough to shoot the high quality pictures. Therefore, one with higher resolution should be employed to improve this situation in the future. There is a linear relationship between the ten temperatures measured and the output signal of the intrinsic sapphire fibre-optic Fabry-Perot sensor for the range of temperature 75 °C - 435 °C. Nevertheless, the output of the sensor could suffer from some background noise, that is:

1) The straight interference fringes produced by beam splitter interweave with the circular interference fringes output by the intrinsic sapphire fibre-optic Fabry-Perot sensor so that it will lead to a strong noise. Consequently, the coated pellicle beam splitter should be considered to be an alternative in the future.

2) The reflected light from microscope objective was also an important factor if compared Figure 3 - 17 with Figure 3 - 18. However, it can be improved by using all fibre-optic system in the future.

3) In view of the fact that the sapphire fibre is heated by nonuniform way limited by the shape of the solder iron, it causes the changes of the output of the sensor. Therefore, further experiment for calibration needs to be done in the future.

§3.3 Extrinsic Sapphire Fibre-optic Fabry-Perot Sensors

Based on the method proposed in the wedge interferometer experiment in section §3.1, the aim of the experiment is to establish a procedure which can exploit directly the observation of the interference fringe output of extrinsic sapphire fibre-optic Fabry-Perot sensors, and determine the air gap cavity length of sensors without initiation.

§3.31 Functional relationship between the output of interference signal of extrinsic sapphire fibre-optic Fabry-Perot sensors and temperature

We assumed that the extrinsic sapphire fibre-optic Fabry-Perot sensors will be fixed to homogeneous plate materials and the adhesive such as high temperature ceramic adhesive based on aluminum oxide will have the same coefficient of volumetric thermal expansion with the sapphire fibre at the temperature T_1, as it is shown in Figure 3 - 24. L_a and L_b is the distance between the attachment point and the endface of sapphire fibre a and sapphire fibre b, respectively. L is the length of cavity, and L_g is the distance between the two attachment points.

For the extrinsic sapphire fibre-optic Fabry-Perot sensor, the optical path difference for maximum fringe brightness can be described as

$$\Delta \cong 2nL = m\lambda \tag{3 - 26}$$

where n is the refractive index of the interferometer medium. For air, n= 1. So, we have

$$\Delta \cong 2L = m\lambda \tag{3 - 27}$$

When the extrinsic sapphire fibre-optic Fabry-Perot sensors is heated from temperature T_1 to temperature T_2, there is a corresponding linear change of interference cavity from L to L' in length, respectively. Therefore, we have

$$2(L'-L) = (m'-m)\lambda = N\lambda \tag{3 - 28}$$

where, N is the number of interference fringes counted in going from T_1 to T_2. Here,

$$L' = L - \Delta L_a - \Delta L_b + \Delta L_g \tag{3 - 29}$$

where ΔL_a and ΔL_b is the change of the distance between the attachment point and the endface of sapphire fibre a and sapphire fibre b, respectively, from temperature T_1 to temperature T_2. ΔL_g is the change of homogeneous plate material from temperature T_1 to temperature T_2. From equation 3 - 17, we have

$$\alpha_{sap} L_a \Delta T = \Delta L_a \tag{3 - 30}$$

$$\alpha_{sap} L_b \Delta T = \Delta L_b \tag{3 - 31}$$

$$\alpha_m L_g \Delta T = \Delta L_g \tag{3 - 32}$$

where, α_{sap} is the coefficient of volumetric thermal expansion of the sapphire fibre, α_m is the coefficient of volumetric thermal expansion of the homogeneous plate materials. ΔT is the change of temperature due to heating. As a result, the number of fringes in the output signal of the sensor with the increase of temperature is described as

$$N = \frac{2(\alpha_m L_g - \alpha_{sap} L_a - \alpha_{sap} L_b)\Delta T}{\lambda} \tag{3 - 33}$$

Considering the fabrication of interferometer cavity, the length of cavity should meet the following condition if $\Delta L_a^{\max} + \Delta L_b^{\max} > \Delta L_g^{\max}$

$$\Delta L_a^{\max} + \Delta L_b^{\max} - \Delta L_g^{\max} \le L < \frac{\lambda^2}{\Delta\lambda} \tag{3 - 34}$$

where, $\Delta L_a^{\max}$ and $\Delta L_b^{\max}$ is the maximum change of the distance between the attachment point and the endface of sapphire fibre a and sapphire fibre b, respectively, from temperature T_1 to temperature T_2. $\Delta L_g^{\max}$ is the maximum change of homogeneous plate material from temperature T_1 to temperature T_2.

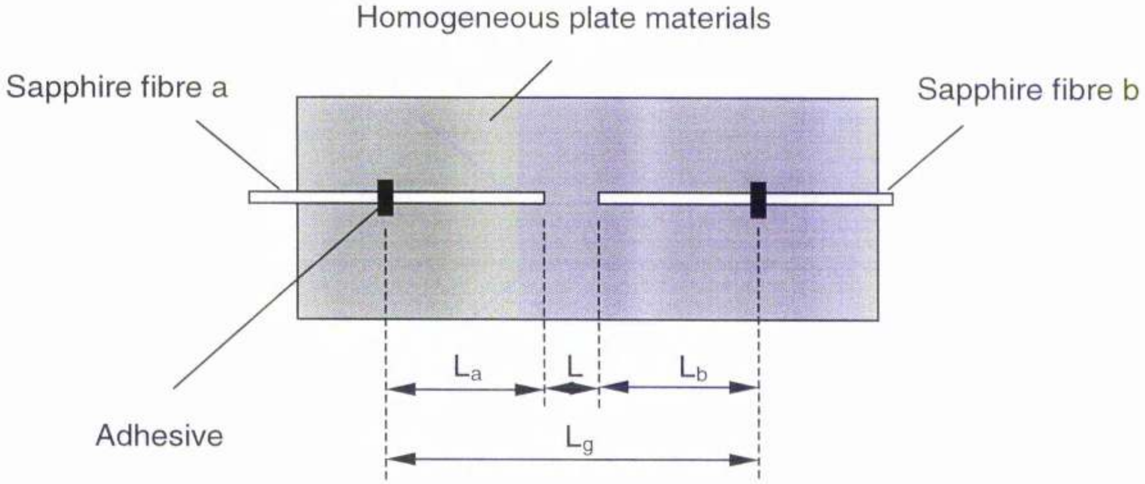

Figure 3 - 24 The schematic of extrinsic sapphire fibre-optic Fabry-Perot sensor

For the extrinsic sapphire fibre-optic Fabry-Perot sensor, if we assumed that I_0 is the intensity of the incident light, I_1 is the intensity of the light reflected from the first sapphire - air interface, and I_2 is the intensity of the transmitted light from the first sapphire - air interface with the opposite direction of incident light, which is the light reflected from the endface of the second air - sapphire interface. where,

$$I_1 = R(1-R)\times I_0 = 7.63\%(1-7.63\%)\cdot I_0$$

$$I_2 = R(1-R)^3\times I_0 = 7.63\%\cdot(1-7.63\%)^3\cdot I_0$$

Therefore, the visibility can be expressed as

$$V_{ext} = \frac{2\sqrt{I_1\times I_2}}{I_1+I_2} = \frac{2\times 7.63\%\times(1-7.63\%)^2}{7.63\%(1-7.63\%)+7.63\%(1-7.63\%)^3} = 99.69\% \approx 1$$

For the extrinsic sapphire fibre-optic Fabry-Perot sensor, the signal received by the detector can be described as

$$I_{ext} = \frac{1}{4}(1-R)(I_1+I_2)(1+V_{ext}\cos\delta) \qquad (3-35)$$

Hence, we have

$$\frac{I_{ext}}{I_0} \approx 6.03\%\cos^2(\frac{\delta}{2})$$

Obviously, the output signal of the extrinsic sapphire fibre-optic Fabry-Perot sensor will be weaker considerably than the intensity of light launched into the sensor though the interference fringes also have a good visibility theoretically.

§3.31.1 Experimental Design

Figure 3 - 25 shows the schematic diagram for the experiment. Light from a HeNe laser with wavelength 632.8nm passes through a spatial filter with a 25 μm diameter pinhole and is expanded by a beam expander. It is first divided by the coated pellicle beam splitter which is used to separate the input and output light to and from sensor. The light then is launched by a 10X microscope objective into the multimode sapphire fibre. A special holder, which can adjust the angle between the principle axis of the microscope objective and the axis of the sapphire fibre, is used to fix the sapphire fibre a. Sapphire fibre a, whose one endface of which was polished at an slight angle with respect to the fibre axis normal to prevent from intrinsic interference, and Sapphire fibre b, whose far endface was unpolished. The endfaces forming the cavity were carefully prepared to ensure flatness and perpendicularity to the fibre axes, and were aligned face to face along the same axial line to form a low-finesse Fabry-Perot cavity. Sapphire fibre b is attached to a translation stage to produce an accurate reference distance for experiment and system calibration. A soldering iron with ten different temperatures setting is used to heat a small length near the end of sapphire fibre b. The output beam containing the interference fringes is divided by a bulk beam splitter into two parts: one is processed by the chart recorder, and the other is observed directly by the frame-grabbing system which is composed of a travelling microscope, a JVC digital color video camera, a JVC video recorder and computer.

To avoid producing interference fringes by the cavity formed between the end of the microscope objective and the sapphire fibre end, a small angle between its axis and the axis of microscope objective was used.

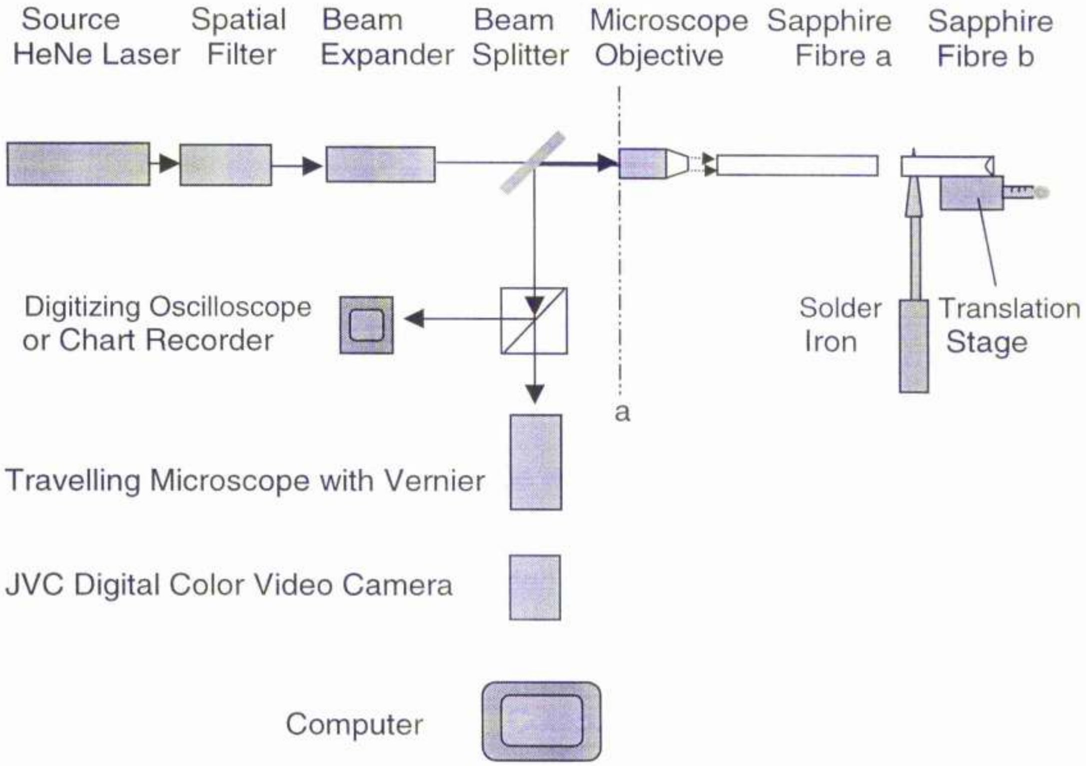

Figure 3 - 25 Schematic of measurement setup of interference fringes from the extrinsic sapphire fibre-optic Fabry-Perot sensor

§3.31.2 Experimental Results and Discussions

i Fringes

Considering the reflected signal from the bulk beam splitter is quite strong and the output of the interference fringes from the extrinsic sapphire fibre-optic Fabry-Perot sensor can also be quite weak, the bulk beam splitter was replaced by a coated pellicle beam splitter to improve this situation. Inserting a piece of black paper in front of the microscope objective (position a), we can see only speckle, which reflected from pellicle itself, instead of the straight interference fringes previously seen with the bulk beam splitter, as it is shown in Figure 3 - 26. Removing the black paper from position a, we can see a kind of mixed-type interference fringe patterns formed by the reflected light from the surfaces of microscope objective, and the two endfaces of sapphire fibre a and the endface of sapphire fibre b, as it is shown in Figure 3 - 27. Obviously, the true output of the cavity interference fringes produced by the extrinsic sapphire fibre-optic Fabry-Perot sensor is partially obscured by the background noise, and therefore can not be easily observed by this experimental configuration. However, the change of interference fringes can be observed in the viewing system when we adjusted the translation stage to move the end of sapphire fibre b, as it is shown in the video cassette.

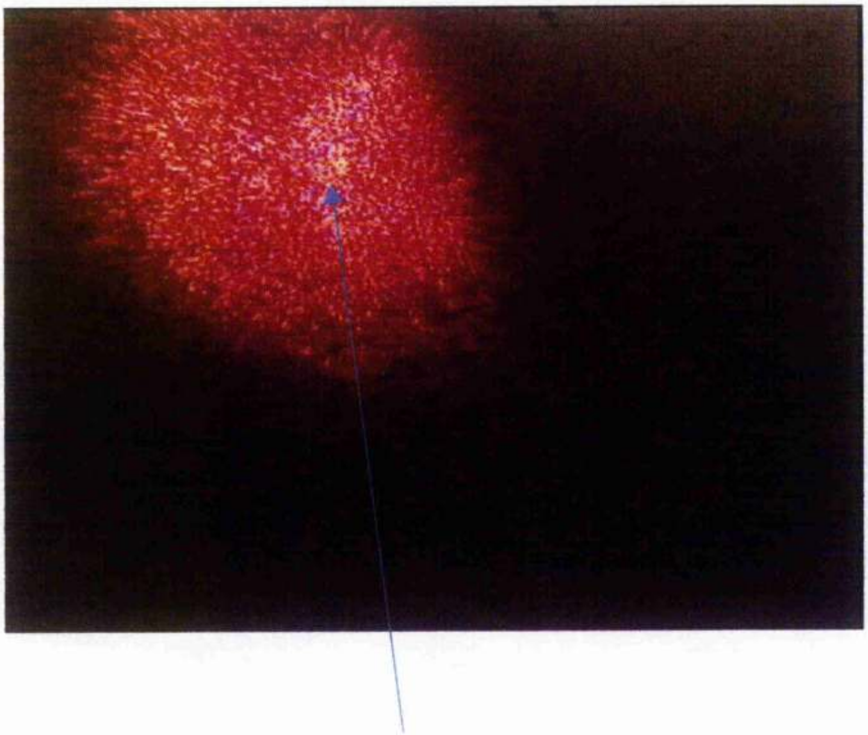

Figure 3 - 26 bright speckle reflected from pellicle itself when placing a black paper at position a

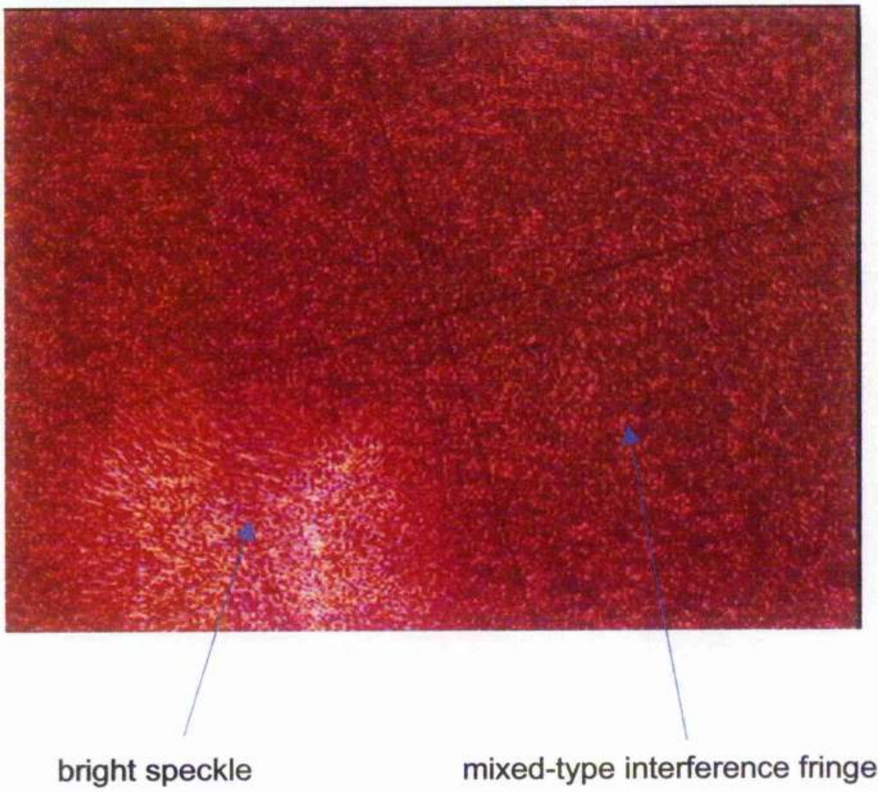

Figure 3 - 27 The output of interference fringes of extrinsic sapphire fibre-optic Fabry-Perot sensors when moving away the black paper at position a

ii Chart

The chart recorder could clearly draw the changes of intensity of interference fringes from darkness to brightness. Therefore, the optical path-length difference at different environmental temperatures could be obtained by counting the number of maxima or minima in the trace of the interference fringes on the drawing, as it is shown in Figure 3 - 28. The irregular output signal of the extrinsic sapphire fibre-optic Fabry-Perot sensors shows that background noise was still present in the system.

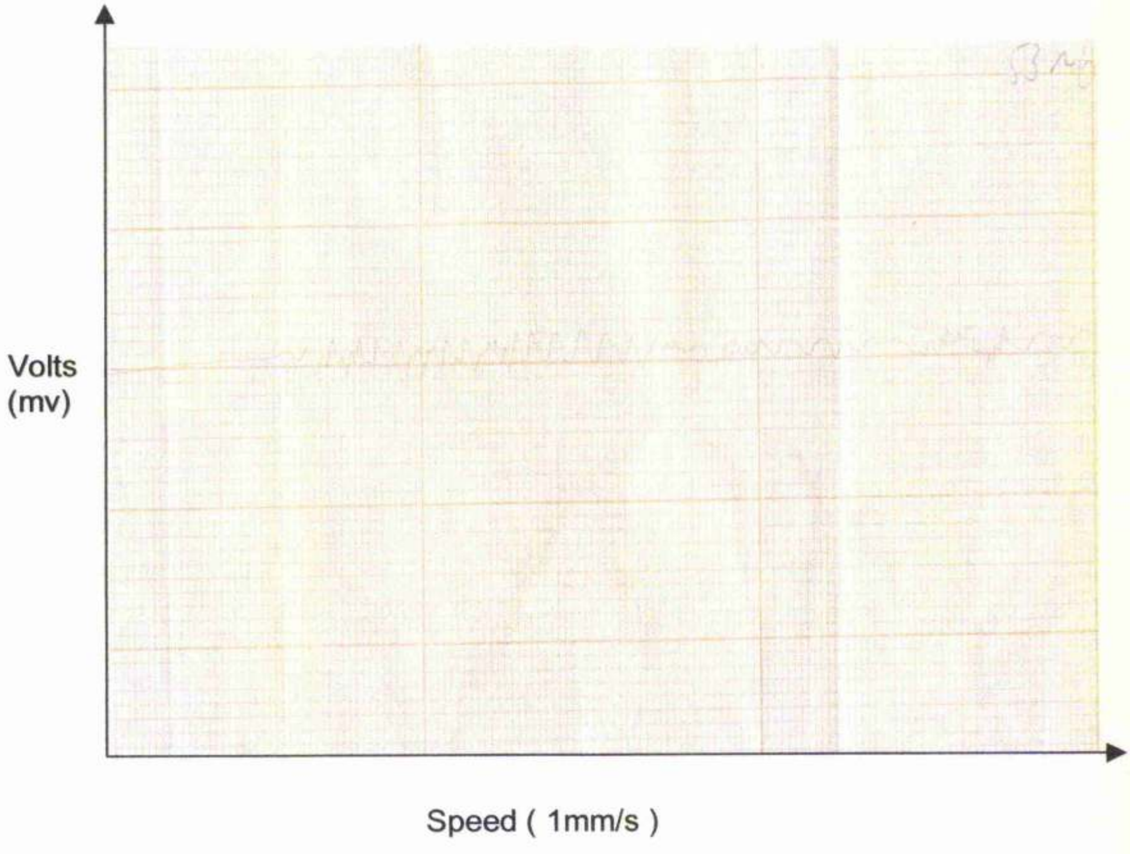

Figure 3 - 28 Chart recording of the output of the extrinsic sapphire fibre-optic Fabry-Perot sensor

iii Discussions

From observation, the output of the interference fringes of the extrinsic sapphire fibre-optic Fabry-Perot sensor can not readily be observed by the low resolution travelling microscope with vernier and JVC digital colour video camera. Therefore, a system with higher resolution should be employed to improve this situation in future. The irregular output signal of the extrinsic sapphire fibre-optic Fabry-Perot sensor shows that background noise was prevalent in the system, that is:

1) Although the coated pellicle beam splitter was used to replace the bulk beam splitter, the interference fringes output by the extrinsic sapphire fibre-optic Fabry-Perot sensor is still affected by the interference between the microscope objective and sapphire fibre a. Also, the output of interference fringes of the extrinsic sapphire fibre-optic Fabry-Perot sensor can be quite weak. Consequently, an all fibre-optic system should be considered to be an alternative to the current free space arrangement in future.

2) Because of the coherence length of HeNe laser, the reflected light from the two endfaces of sapphire fibre a also gave rise to interference fringes and led to an overlap between the fringe of the intrinsic effect and that of the extrinsic effect. Therefore, a laser with shorter coherence length could be considered as an alternative in future work.

3) The sapphire fibre is heated in a nonuniform way limited by the shape of the soldering iron. Therefore, further experiment for exact calibration needs to be done in future.

4) In order to fabricate and calibrate the cavity of the extrinsic sensor, a new setup which can exactly control the distance and situation of the FP cavity needs to be built up in future.

§3.32 White Light Interferometric Signal Processing Techniques

In view of the problem of initiation, environmental perturbation, costs, etc, during the process of the fabrication and measurement of extrinsic fibre-optic Fabry-Perot sensors, white light interferometric signal processing techniques are a good choice to improve the situation discussed-above for its high stability and accuracy [36,37,38].

White light interferometric signal processing techniques utilize a broadband source such as a super-luminescent diode (SLED) instead of a laser in the system of extrinsic sapphire fibre-optic Fabry-Perot sensors. A spectrometer and a personal computer finish the signal processing, as it is shown in Figure 3 - 29.

If an LED has a Gaussian spectral intensity distribution in their emitted radiation, this can be expressed by the formula [39]

$$I(k) = I_0 \cdot \exp[-(\frac{k - k_0}{\sigma / 2})^2] \qquad (3 - 36)$$

where k_0 is the central wave number and σ is the half width of the spectra ($k_0 - k$) at which the optical power falls to e^{-1} of its maximum value at k_0.

For the extrinsic sapphire fibre-optic Fabry-Perot sensor, the signal received by the detector can be described as

$$I(k) = I_0 \cdot [1 + v(k, \Delta)\cos[\varphi(k, \Delta)]] \qquad (3 - 37)$$

where *v(k, Δ)* is the visibility function of the output of interference fringes, Δ is the optical path difference of the interferometer cavity. Here

$$\Delta \cong 2nL \tag{3 - 38}$$

where *n* is the refractive index of the interferometer medium, *L* is the length of air gap of cavity. *Φ(k, Δ)* is the optical phase angle and can be expressed as

$$\phi(k,\Delta) = \frac{2\pi\Delta}{\lambda} \tag{3 - 39}$$

where *λ* is the wavelength of light in vacuum. So, we have

$$\phi(k,\Delta) = \frac{2\pi\Delta}{\lambda} = \frac{4\pi nL}{\lambda} \tag{3 - 40}$$

Consider two different wavelengths from the LED source λ_1 and λ_2 which can be expressed as

$$\phi_i(k,\Delta) = \frac{2\pi\Delta}{\lambda_i} = \frac{4\pi nL}{\lambda_i} \tag{3 - 41}$$

where i=1, 2. Therefore, the phase difference between the two spectral lines $\Delta\Phi$ is

$$\Delta\phi = \varphi_2 - \phi_1 = \frac{4\pi nL(\lambda_1 - \lambda_2)}{\lambda_1\lambda_2} \tag{3 - 42}$$

Therefore, the length of cavity L is equal to

$$L = \frac{\Delta\phi \cdot \lambda_1 \cdot \lambda_2}{4\pi n(\lambda_1 - \lambda_2)} \tag{3 - 43}$$

Obviously, the length of interferometer cavity can be calculated by measuring the phase difference $\Delta\Phi$, and the wavelengths λ_1 and λ_2, which can be performed by the spectrometer.

§3.32.1 Experimental Design

The experiment set-up is shown in Figure 3 - 29.

An LED with a central wavelength λ_0 of 880 nm and a spectral width $\Delta\lambda$ of 80 nm was used as the light source. The light from the LED is collimated and expanded by a beam expander, and then passes through a beam splitter which is used to separate the input and output light of sensor. Light from the LED is transmitted by a 10 X microscope objective into the sapphire EFPI. A special holder, which can adjust the angle between the principle axis of the microscope objective and the axis of the sapphire fibre, is used to fix the orientation of the sapphire fibre. Sapphire fibre a, whose first endface was polished at an small angle with respect to the fibre axis normal, and sapphire fibre b, whose far end was left unpolished, cavity forming endfaces were carefully prepared to ensure flatness and perpendicularity to the axis line of the two sapphire fibres. Sapphire fibres were inserted face to face into a hollow sapphire tube to form a Fabry-Perot cavity. Sapphire fibre b was attached to a translation stage to produce a reference distance for experiment and system calibration. The interference signal was detected by optical detector and processed in a computer-interfaced spectrometer so that the cavity length may be calculated.

It was found that the spectrum of the LED varied with a change of load voltage, that is, if the load voltage varied from 5 V to 9 V, the central spectrum of the LED also rose from 885 nm at 5 V to 899 nm at 9 V, as is shown in Figure 3 - 30 (a), (b). Therefore, we have to choose two fixed values of voltage 5 or 9 Volt in order to ensure the validity of experimental results. Moreover, with the increase of load voltage, the intensity output of the LED also enhances. Hence, the sensitivity setting of the instrument for the load voltage 9 V must be lower than that for the load voltage 5 V to prevent from the overflow. As a result, the figures on the graph of the LED for the load voltage 9 V are less than that for the load voltage 5 V, as is shown in Figure 3 - 30 (a), (b).

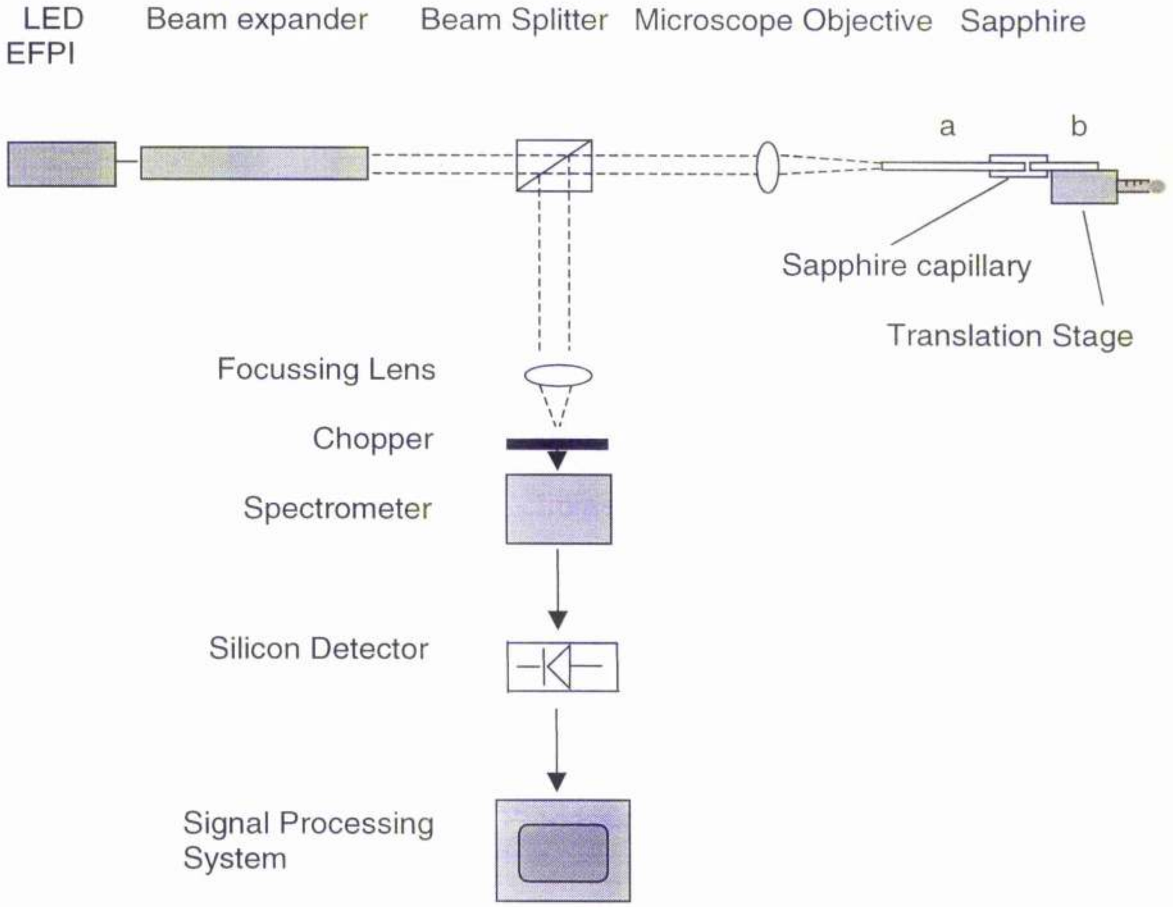

Figure 3 - 29 Experimental setup of extrinsic sapphire fibre-base Fabry-Perot interferometer

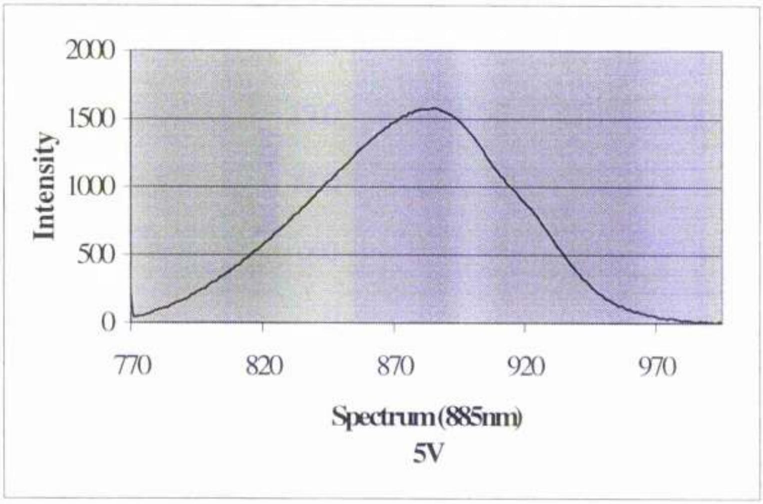

(a) The output spectrum of λ=885 nm LED at 5 Volts

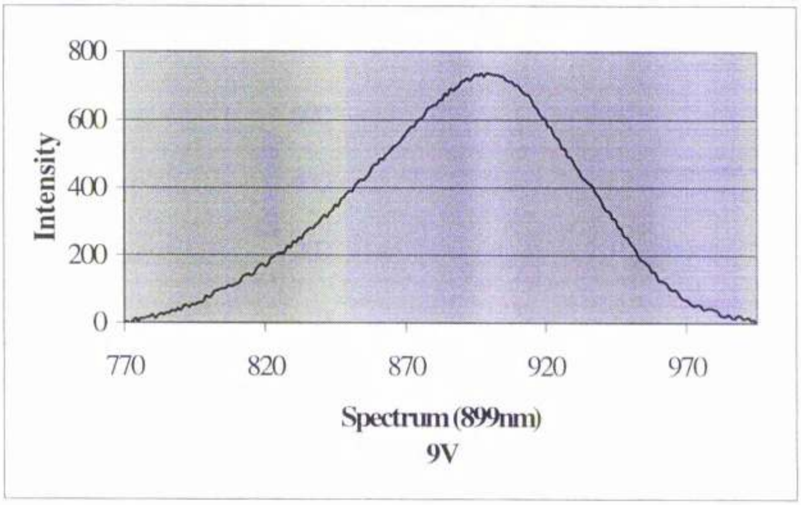

(b) The output spectrum of λ=899 nm LED at 9 Volts

Figure 3 - 30 output spectra of the LED under varying voltage

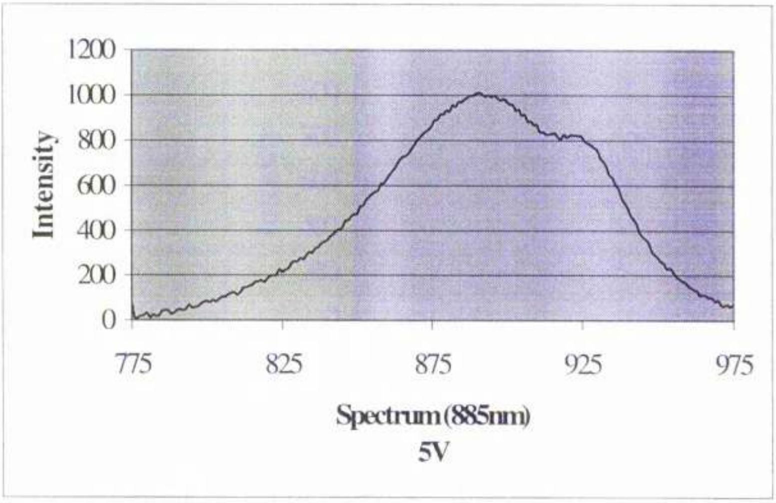

(c) output of LED after working a period of time

Figure 3 - 30 output spectra of the LED under varying voltage

§3.32.2 Experimental Results and Discussions

The experiment result is shown in Figure 3 - 31.

1. When sapphire fibre b is far away the lead-in fibre a, the spectrum output of the EFPI sensor is shown in Figure 3 - 31 (a). When sapphire fibre b is quite close to the lead-in fibre a, the output spectrum of EFPI sensor is also shown in Figure 3 - 31 (b). It is obvious that the intensity of output signal of EFPI is enhanced with the reduction of the air gap. The same phenomenon was also demonstrated as it is shown in Figure 3 - 31 (c), (d), (e), in which the length of the air gap, measured by a dial gauge with a precision of ± 0.01 mm, was adjusted decreasingly by moving translation stage to about 16μm, 6μm, 3μm, respectively.

However, the situation is not always like this as it is shown in Figure 3 - 31 (f), (g), (h), (i), which the air gap is 3μm, 6μm, 12μm, 17μm, respectively. The reason is likely to be due to the undulation of power output of LED after working a period of time, as it is shown in Figure 3 - 30 (c), which the output spectrum of LED transformed if compared with Figure 3 - 30 (a) or (b). The same situation discussed-above also was encountered at the load voltage 9 V, as it is shown in Figure 3 - 33 (b), Figure 3 - 33 (c), Therefore, we need a light source with a stable output in future experiment.

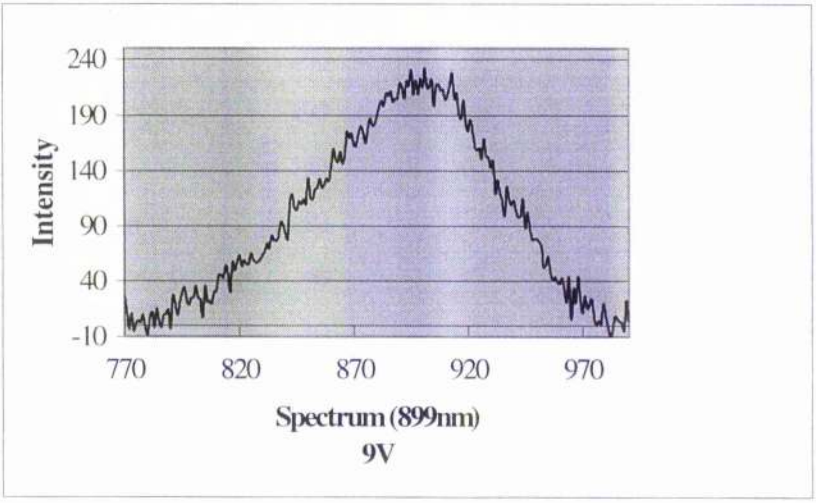

(a) The output spectrum of λ=899 nm LED at 9 V when sapphire fibre b is far away the lead-in fibre a

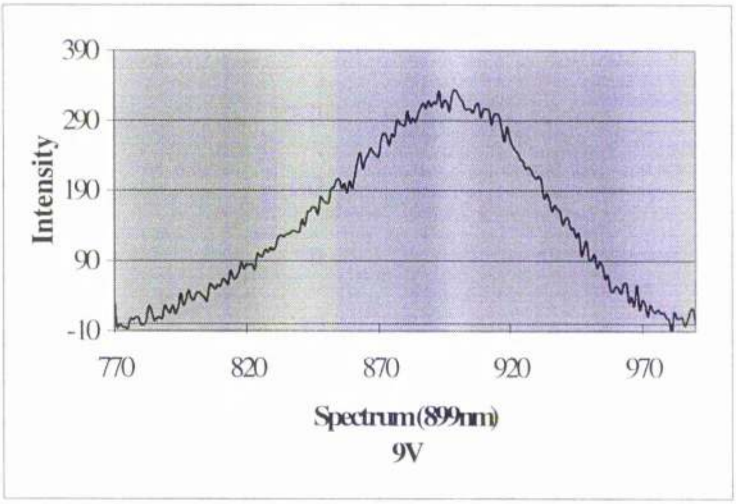

(b) The output spectrum of λ=899 nm LED at 9 V when sapphire fibre b is close to the lead-in fibre a

Figure 3 - 31 The output spectrum of sapphire EFPI sensor at different lengths of air gap

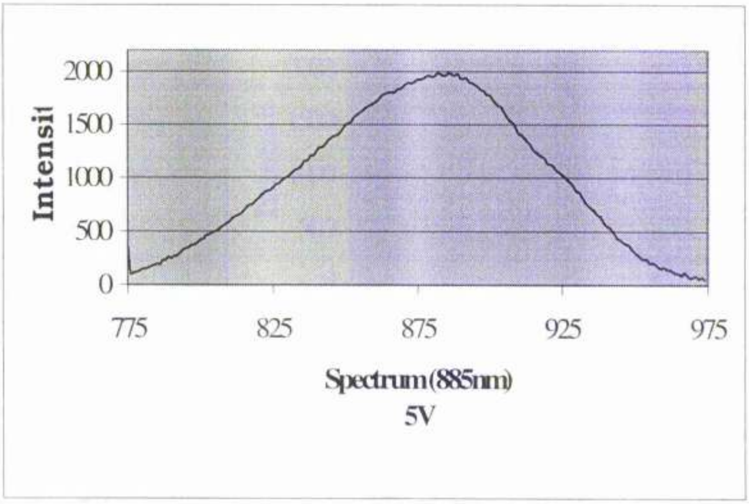

Air gap = 16μm

(c) The output spectrum of λ=899 nm LED at 5 V

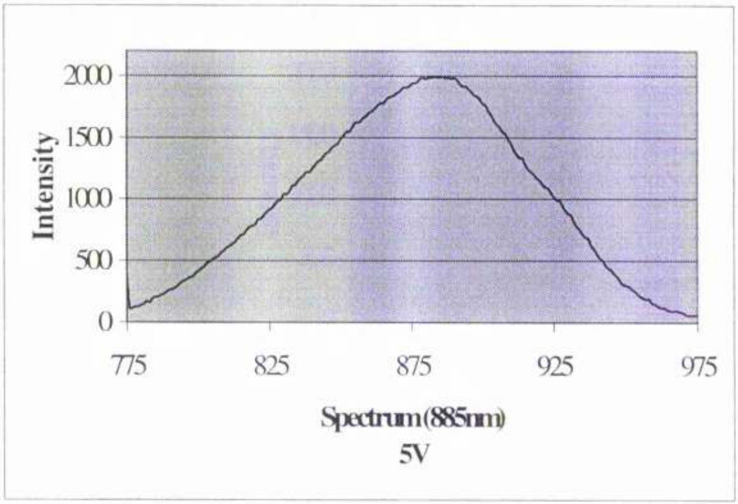

Air gap = 6μm

(d) The output spectrum of λ=899 nm LED at 5 V

Figure 3 - 31 The output spectrum of sapphire EFPI sensor at different lengths of air gap

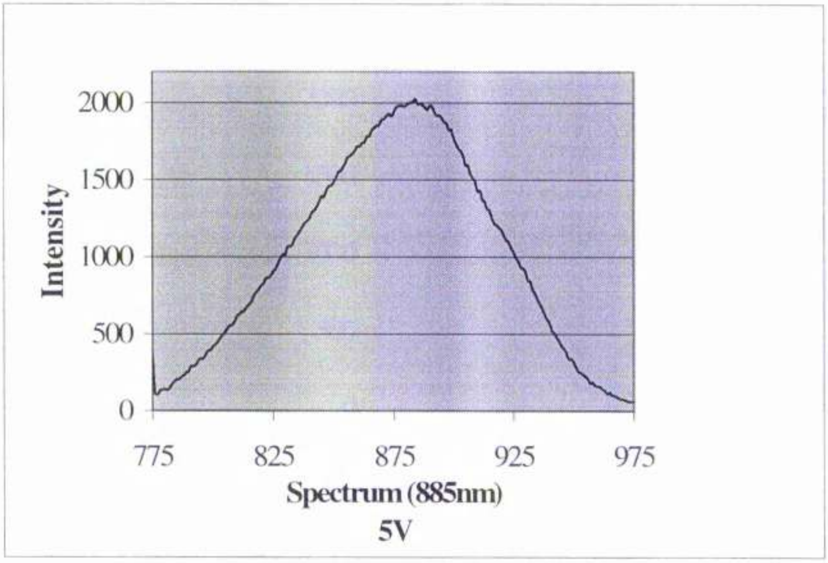

Air gap = 3μm

(e) The output spectrum of λ=899 nm LED at 5 voltage

Figure 3 - 31 The output spectrum of sapphire EFPI sensor at different lengths of air gap

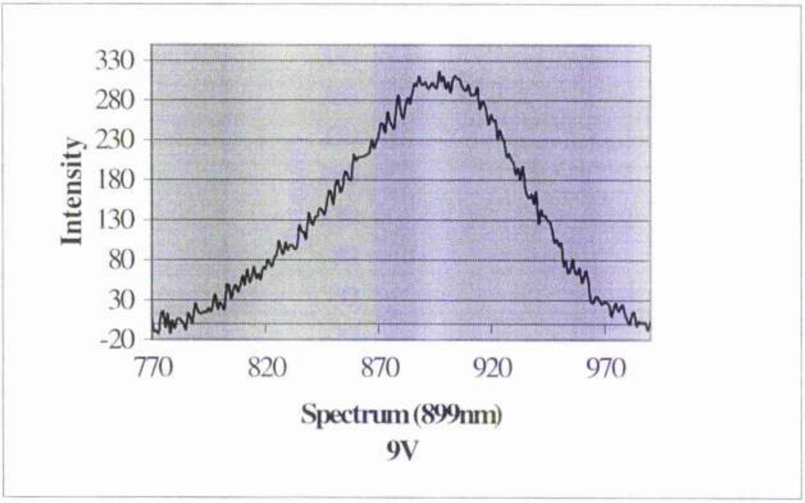

Air gap = 3μm

(f) The output spectrum of λ=899 nm LED at 9 voltage

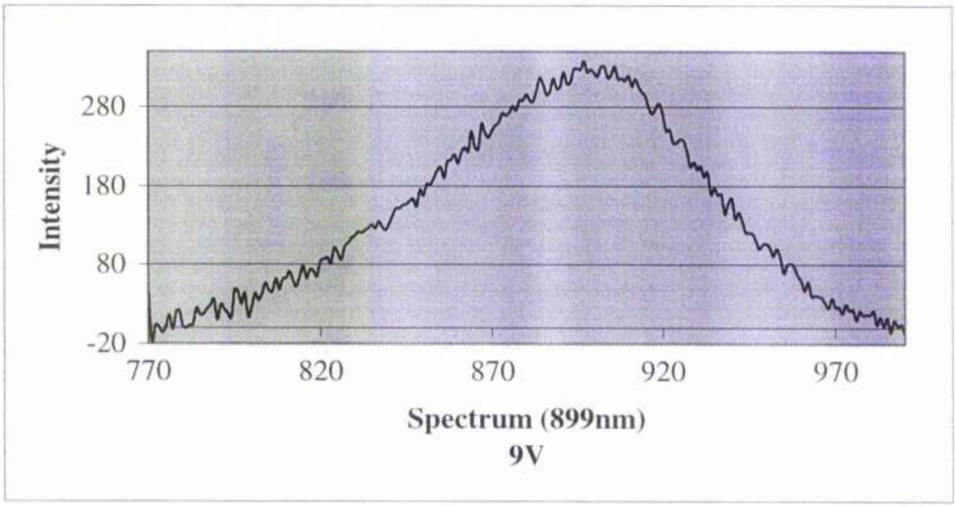

Air gap = 6μm

(g) The output spectrum of λ=899 nm LED at 9 voltage

Figure 3 - 31 The output spectrum of sapphire EFPI sensor at different lengths of air gap

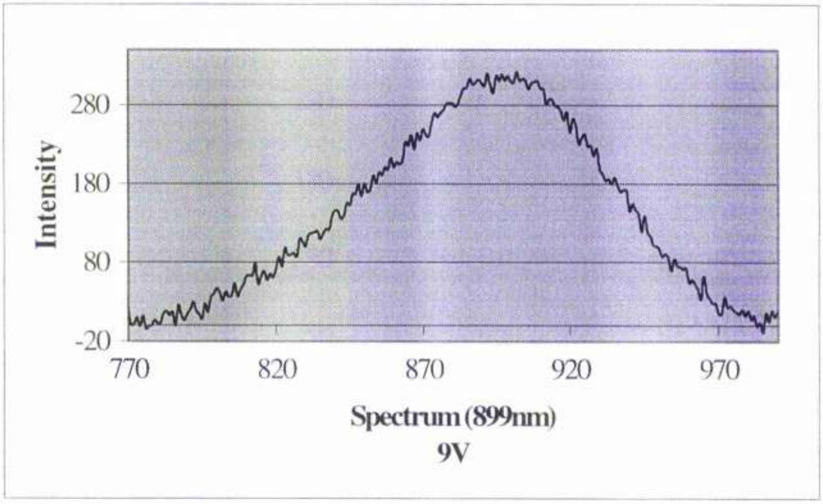

Air gap = 12μm

(h) The output spectrum of λ=899 nm LED at 9 voltage

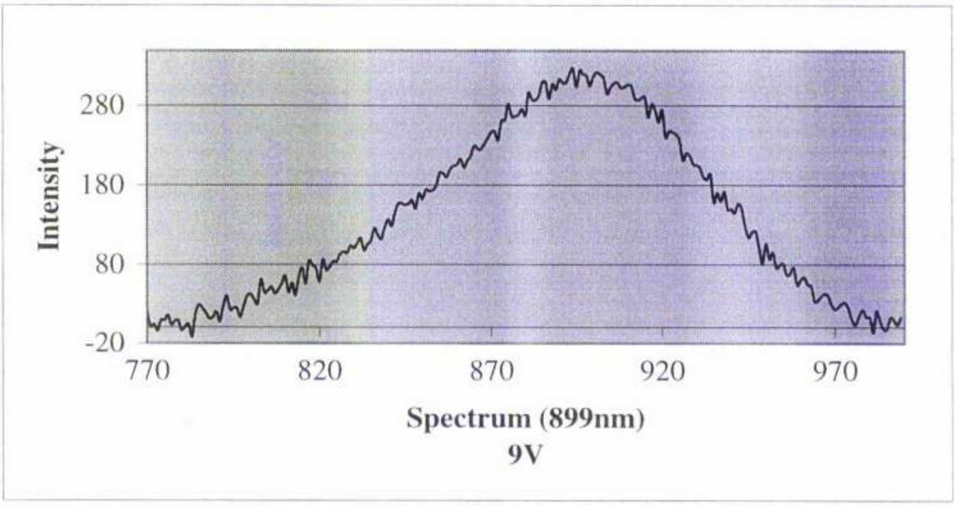

Air gap = 17μm

(i) The output spectrum of λ=899 nm LED at 9 voltage

Figure 3 - 31 The output spectrum of sapphire EFPI sensor at different lengths of air gap

2. Comparing Figure 3 - 31 with Figure 3 - 30 (a), (b), the spectra from the fibres have significantly increased noise level. It means the output signal of the EFPI sensor includes a large amount of noise so that very low fringe visibility is obtained, and this leads to the issue that the desired output signal can not be distinguished by spectrometer.

The following works were done in order to determine the origin of noise.

i. To adjust the translation stage carefully, detect the output signal by spectrometer. The result is shown in figure 3 - 31 (f), (g), (h), (i). Obviously, there is no significant difference between the four output spectra. Therefore, this implies that the background signal received by the optical detector totally covered the change due to the FP signal.

ii. Clean the endfaces of the sapphire fibres, splitter, and then detect the output signal again. The curves of output spectrum become less noisy as is shown in Figure 3 - 31 (c), (d), (e) in comparison with those before cleaning as it is shown in Figure 3 - 31 (a), (b). Consequently, we must take some special precautions to prevent from the contamination caused by airborne particulate and man-made faults.

iii. With the increase of load voltage from 5 V to 9 V, the intensity output of the LED also enhances. As a result, the noise level is correspondingly enhanced if comparing Figure 3 - 30 (a) with Figure 3 - 30 (b).

iv. If we used the infrared viewer to observe the light directly, we saw a lot of reflected and scattered light from the splitter, lens, beam expander, etc. By adjusting the angle of the splitter and the angle between the principle axis of the microscope objective and the axis of the sapphire fibre, we can filter a part of scattered light from the splitter. The result is as shown in Figure 3 - 32 (a), (b). Apparently, the major factors which produce the background signal is the reflected light from the splitter, etc.

v. As Figure 3 - 32 (b) shows, the signal we received is so weak that we can not distinguish it. We have to change to a more sensitive detector, the result is shown in Figure 3 - 33 (a). The signal received by new detector is more evident, but it still includes a lot of noise. So, we add a lens before the spectrometer to focus the signal. The result is shown in Figure 3 - 33 (b). However, the remaining background signal is also strengthened at the same time as the desired signal, as is shown in Figure 3 - 33 (c). The different spectra between Figure 3 - 33 (b) and Figure 3 - 33 (c) was contributed to the different positions and angles of lens. As a result, we still can not extract the signal from the FP cavity.

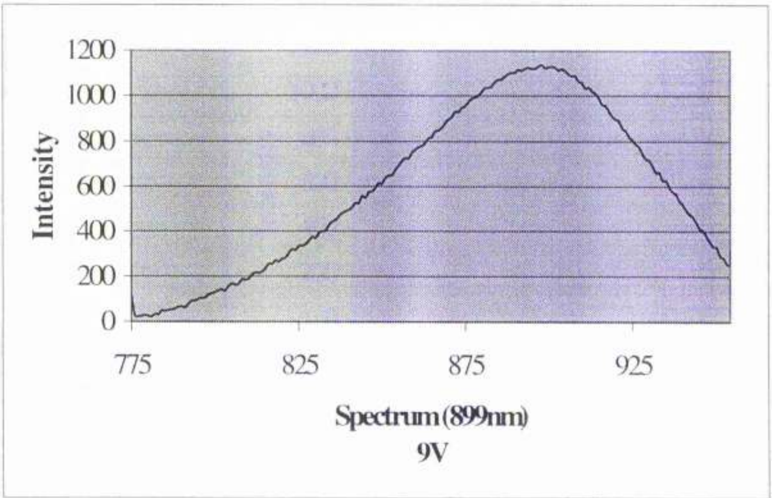

(a) The Output Spectrum before filtering reflection light from splitter

Figure 3 - 32 Comparison of Output Signal

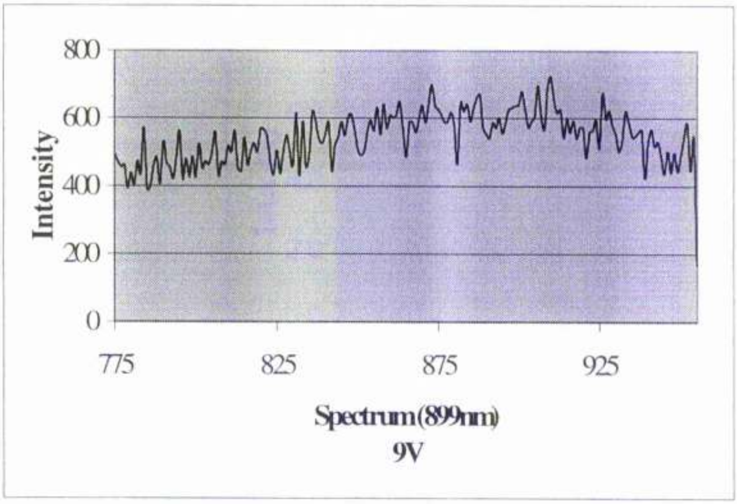

(b) The Output Spectrum after filtering reflection light from splitter

Figure 3 - 32 Comparison of Output Signal

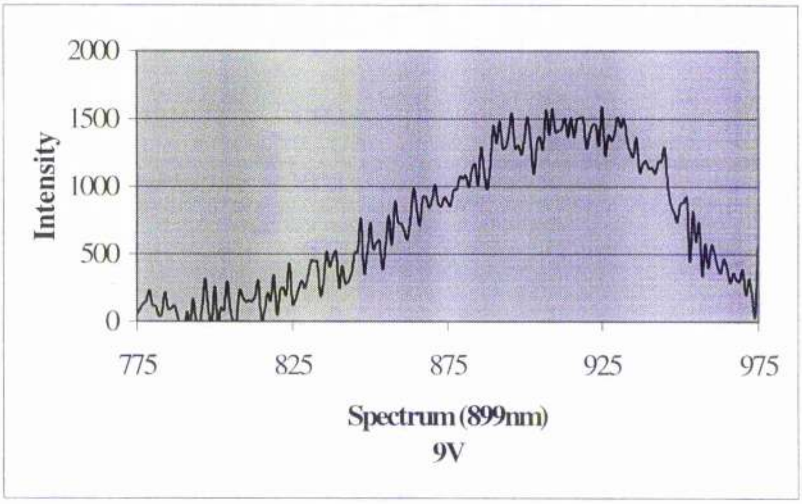

(a)

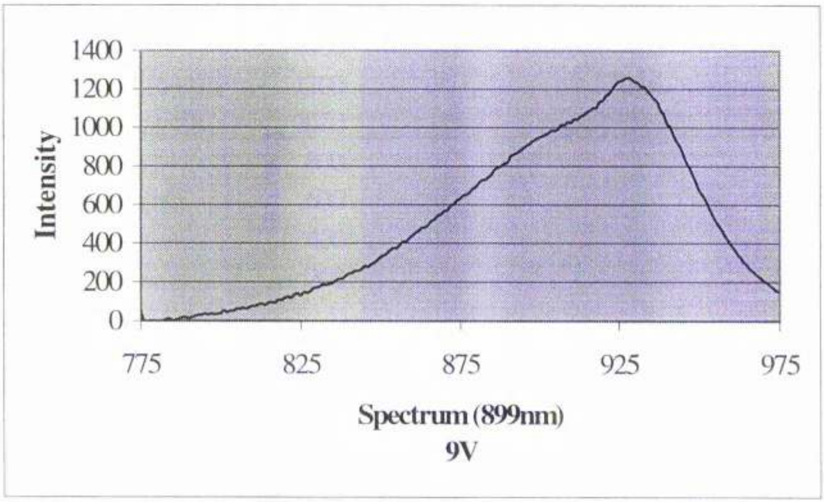

(b)

Figure 3 - 33 Signal Received by New Detector

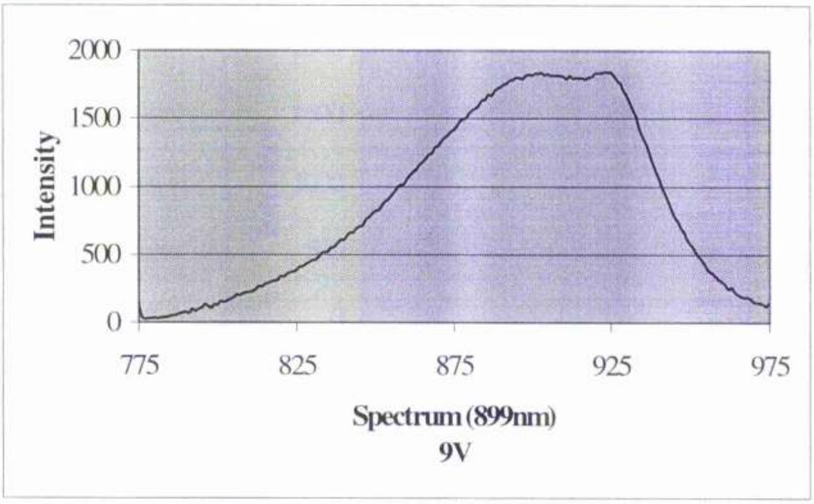

(c)

Figure 3 - 33 Signal Received by New Detector

In summary, the reason why the present set-up used is not suitable for detecting the interference signal of sapphire EFPI sensor by white light interferometric signal processing techniques is not only the noise caused by reflected and scattered light from splitter, lens, etc. but also due to the large loss of the cavity signal caused by multiple reflections. Therefore, we must change the present experimental set-up into all-fibre setup to detect the interference signal in future work.

§3.4 Monolithic Sapphire Fibre-optic Fabry-Perot Sensors

In order to fabricate an integrated Fabry-Perot sensor, a monolithic Fabry-Perot cavity structure was designed. Michelson interferometric testing was also used to assess the optical quality of the internal surface of the melted end of the sapphire tube.

§3.41 Phase relationship between the output of the interference signal of monolithic sapphire fibre-optic Fabry-Perot sensors and the angular frequency of sound wave

From Figure 2 – 14, the output signal of the monolithic sapphire fibre-optic Fabry-Perot sensors can be expressed as

$$I = I_1 + I_2 + 2\sqrt{I_1 I_2}\cos\delta \tag{3 - 44}$$

where I_1 is the intensity of light from the endface of the lead-in sapphire fibre, and I_2 is the intensity of light from the endface of the sapphire diaphragm. δ is the total phase difference arising from the optical path difference between the two reflections. Here, given that the refractive index of air, n=1, we have

$$\delta = \frac{4\pi nL}{\lambda} = \frac{4\pi L}{\lambda} \tag{3 - 45}$$

Hence, we have

$$d\delta = \frac{4\pi}{\lambda} dL \tag{3 - 46}$$

where dL is the total change of the optical path difference of the interferometer cavity, and equal to

$$dL = dL_P + dL_T \tag{3 - 47}$$

where, dL_P is the change of the optical path difference of the cavity caused by pressure change of background, and is the function of pressure P. dL_T is the thermal expansion change of the optical path difference of the cavity generated by the temperature change. Hence, we have

$$d\delta = \frac{4\pi}{\lambda} dL = \frac{4\pi}{\lambda} (dL_P + dL_T) \tag{3 - 48}$$

where, the pressure P is the function of temperature T and the angular frequency of sound wave ω. Finally, we can have

$$dL_P(\omega, T) = \frac{\lambda}{4\pi} d\delta - dL_T \tag{3 - 49}$$

§3.42 The Fabrication of The Head of Sensors

Direct laser melting was used to fabricate the head of the sensors, as is shown in Figure 3 - 34. A beam of CO_2 laser radiation is expanded and split into a hollow cylindrical tube beam with relatively uniform intensity distribution by a reflaxion, as is shown in Figure 3 - 35, and then reflected and projected by a coated plane mirror oriented at an angle of 45° onto a parabolic mirror which is used to focus the cylindrical beam on a small spot to melt the top of the sapphire tube. Very high temperatures can be achieved rapidly. The sapphire capillary is clamped by a special holder so that the end of the tube is melted, and then cooled during a period of time. Finally, this melted top section of sapphire tube sheath is polished until the head of sensor we need was obtained.

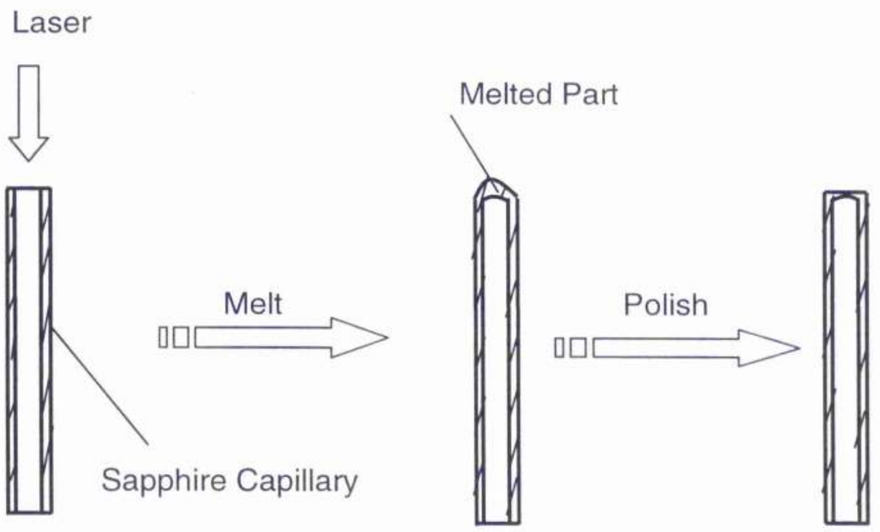

Figure 3 - 34 Schematic of procedure of Fabrication of Sapphire Sheath

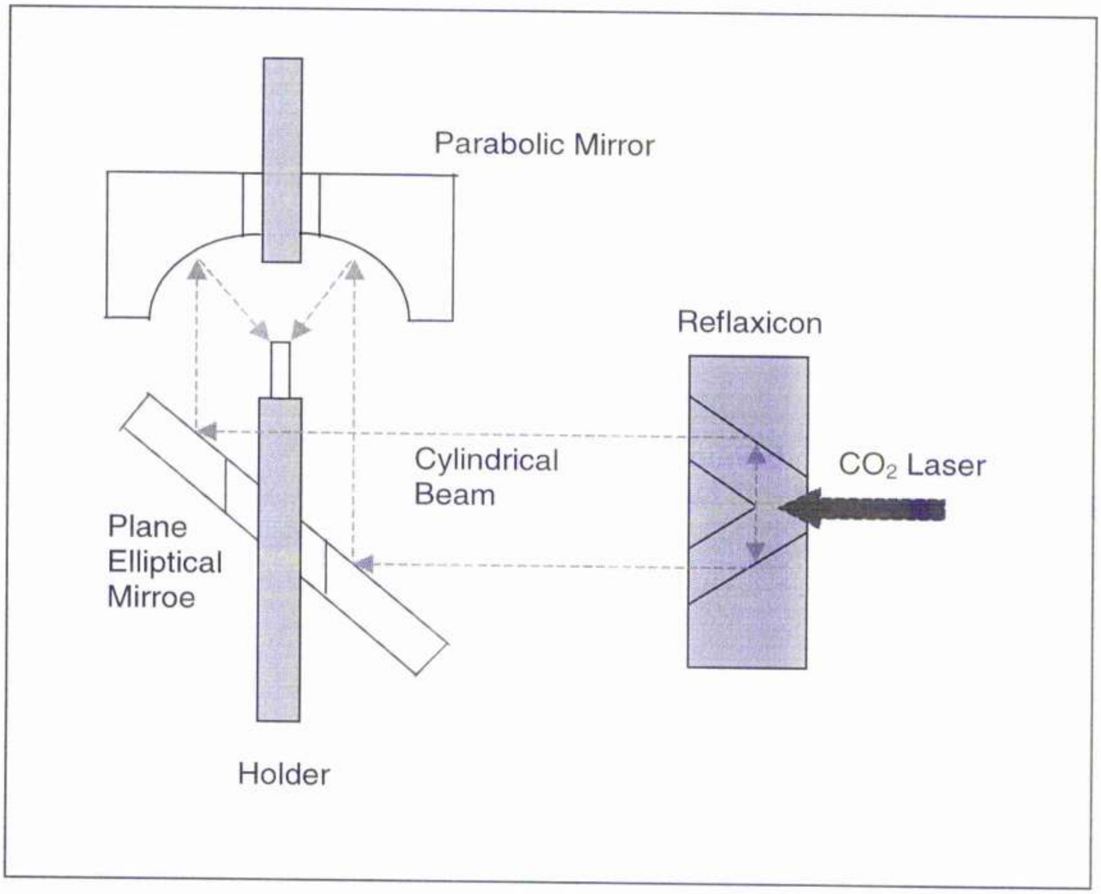

Figure 3 - 35 Schematic of procedure of Fabrication of Sapphire Sheath

A microscope was used to examine the internal surface of the melted end of the sapphire tube to assess the quality of the surface, and the results are shown in Figure 3 - 36. The inner face of the sapphire capillary can be seen to be rough. This situation is likely to be caused by the surface tension of the melting area on the top of the sapphire capillary when cooling. Although the way to fabricate the sapphire sheath is controlled deliberately under almost identical conditions, the shapes of the internal surfaces of the sheaths were found to be quite different, as is shown in Figure 3 - 37 (a), (b), (c), (d). During production, there is slight variation in position and angular alignment between the sapphire tube and the laser axis, which makes the temperature distribution on the melting end of sapphire tube nonuniform and results in varying thermal stresses when cooling.

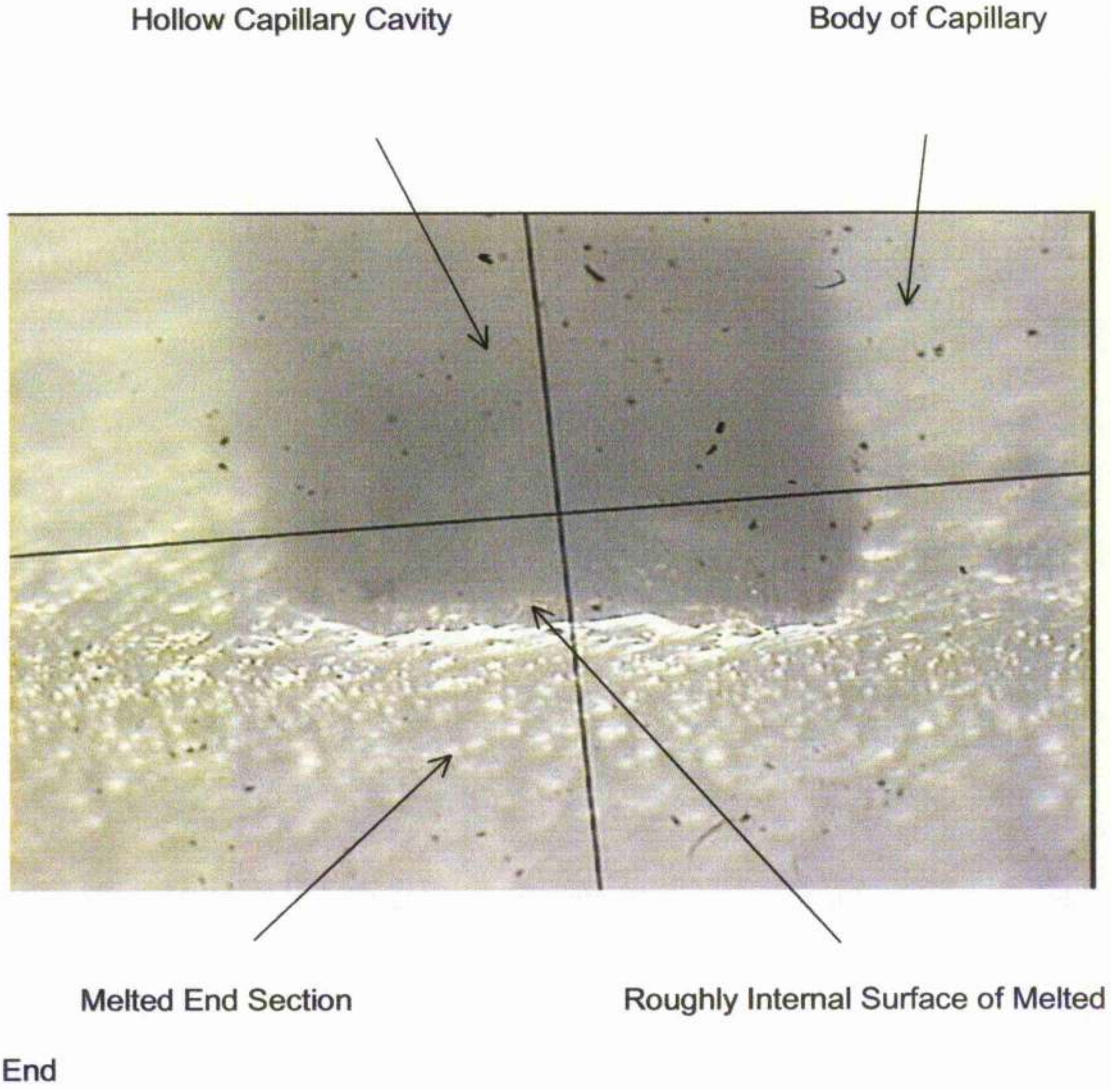

(a)

Figure 3 - 36 The Picture of the Inner Face of a Melted End of a Sapphire Capillary Sheath

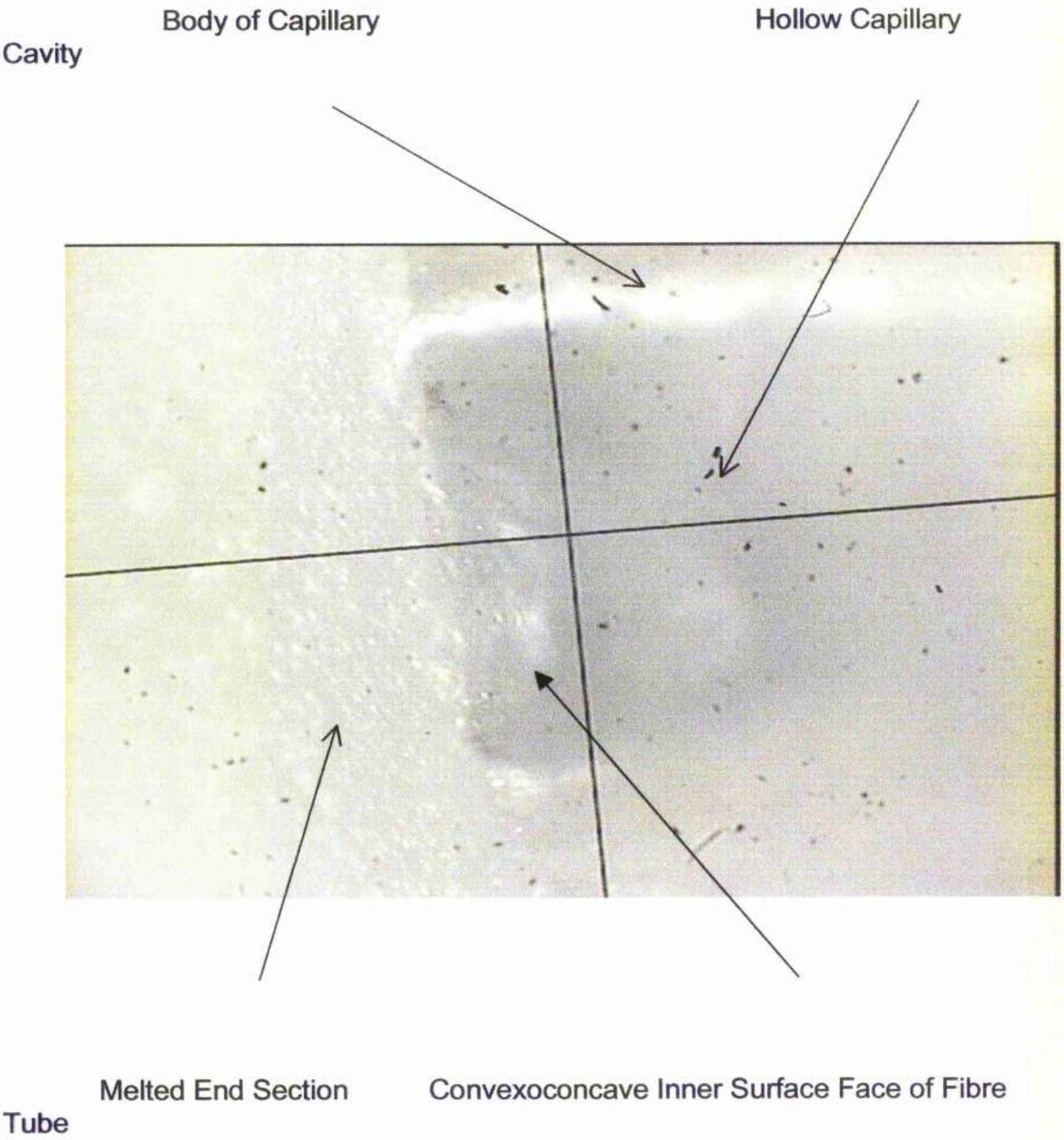

(b)

Figure 3 - 36 The Picture of the Inner Face of a Melted End of a Sapphire Capillary Sheath

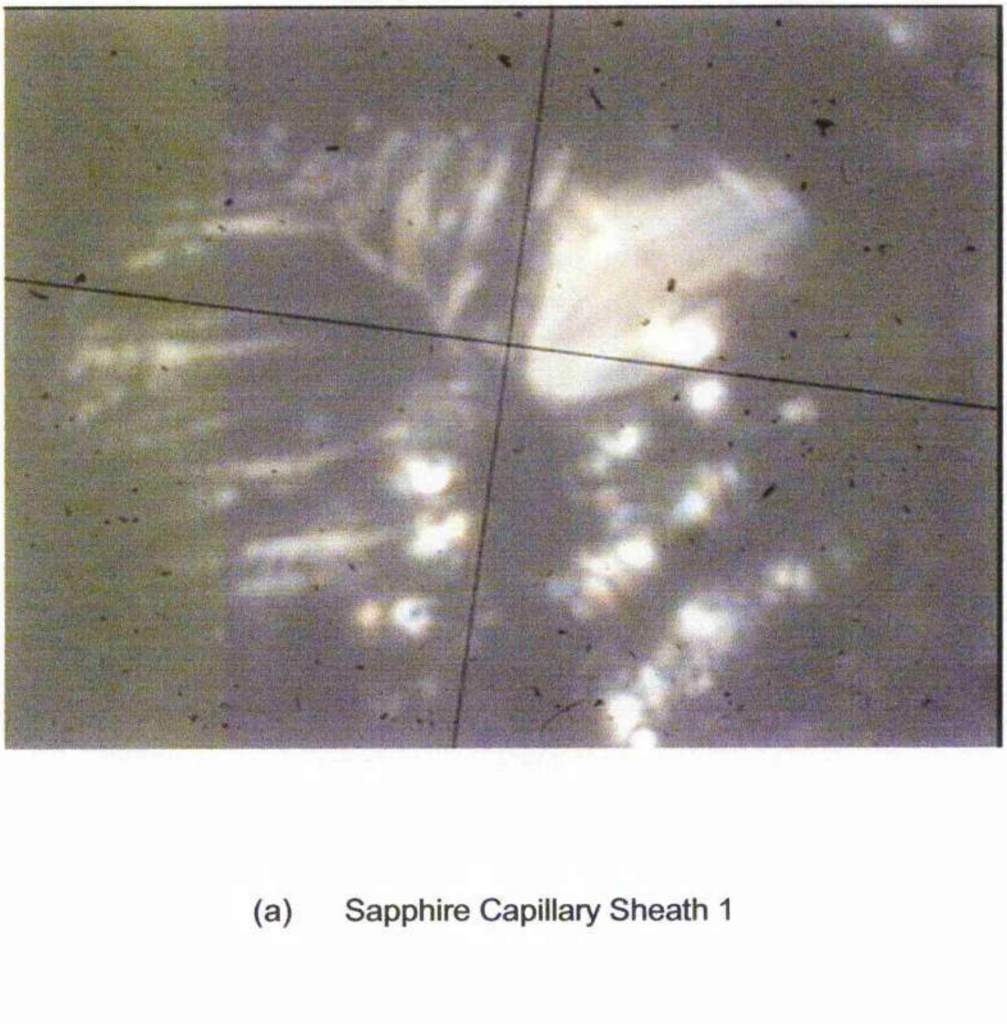

(a) Sapphire Capillary Sheath 1

Figure 3 - 37 The Picture of the Inner Face of a Melted End of a Sapphire Capillary Sheath

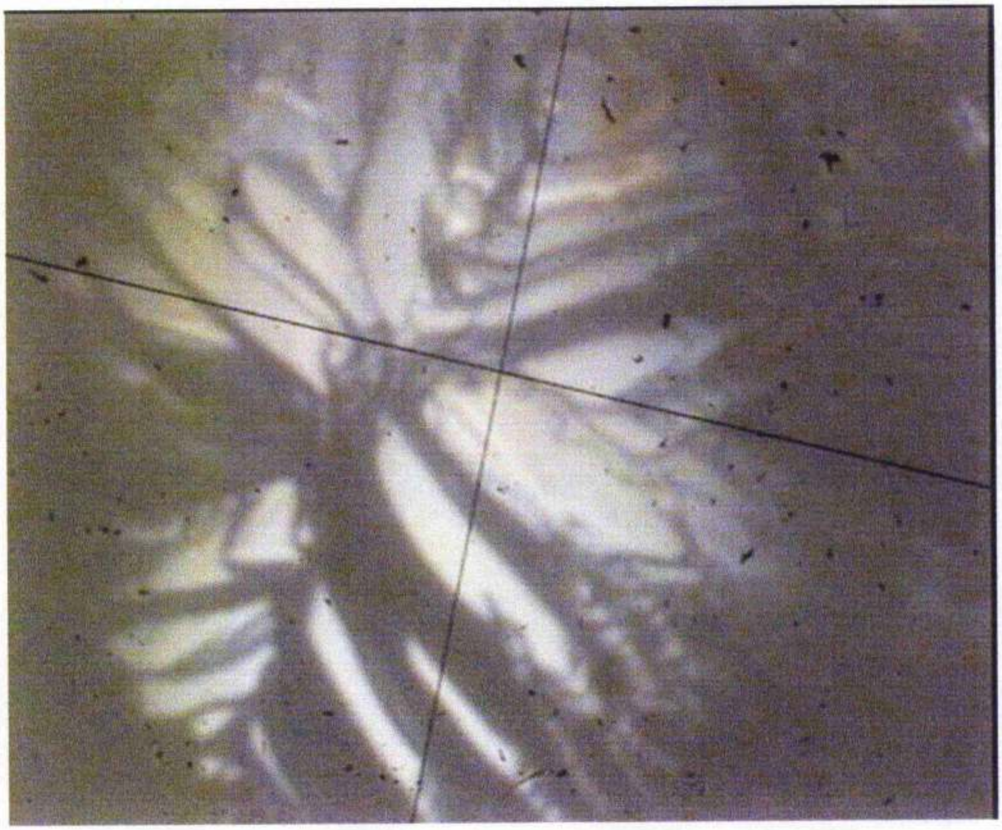

(b) Sapphire Capillary Sheath 2

Figure 3 - 37 The Picture of the Inner Face of a Melted End of a Sapphire Capillary Sheath

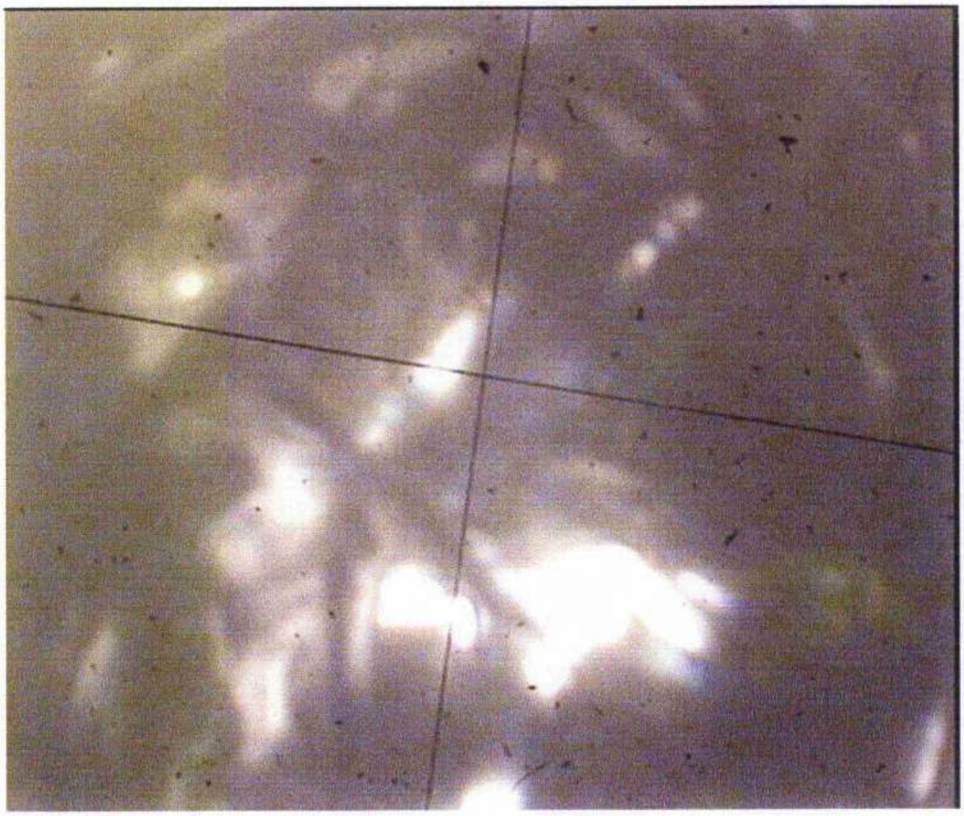

(c) Sapphire Capillary Sheath 3

Figure 3 - 37 The Picture of the Inner Face of a Melted End of a Sapphire Capillary Sheath

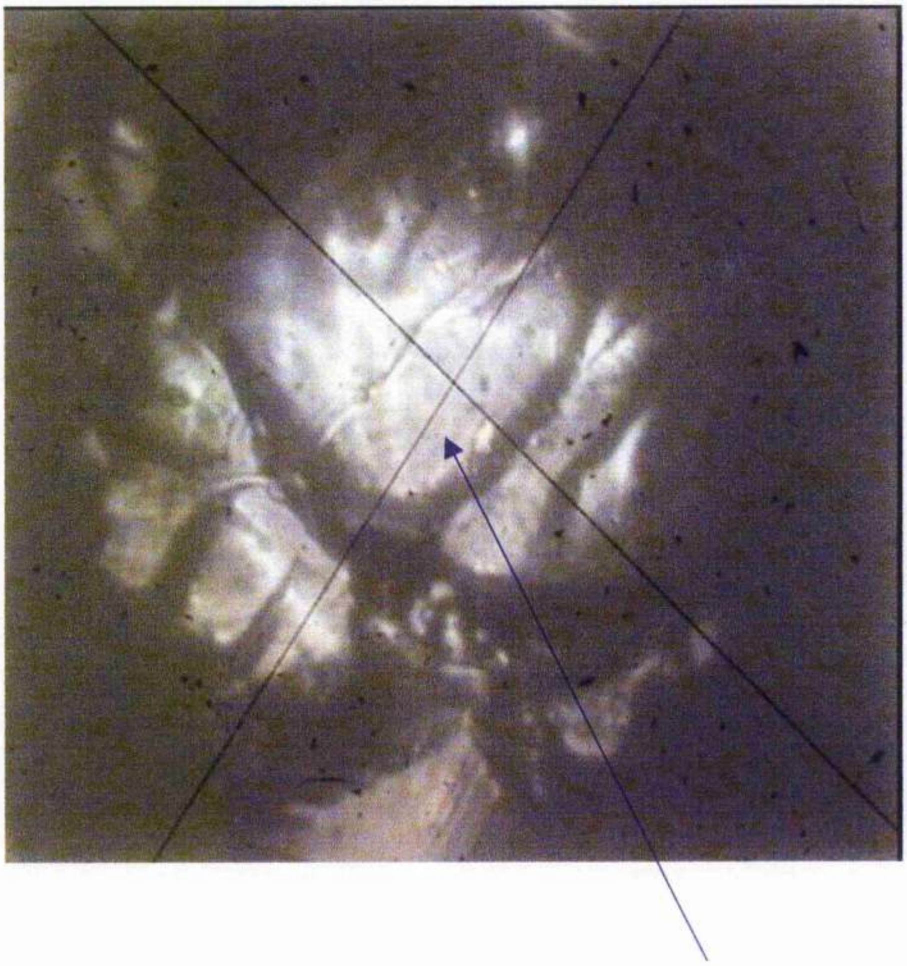

(d) Sapphire Capillary Sheath 4

Figure 3 - 37 The Picture of the Inner Face of a Melted End of a Sapphire Capillary Sheath

§3.43 Michelson Interferometric Method Testing

To evaluate the optical quality of the internal surface of the melted end of the sapphire capillary and its usefulness in being able to form a reflective cavity, a Michelson interferometric method was used to observe directly the interference fringes generated by the reflected lights from a mirror and from the internal surface of sapphire tube sheath.

A special holder, which could adjust the angle of the capillary, was used to fix the sapphire tube sheath. In order to eliminate the reflected light from the rim of the other endface of the sapphire tube sheath, the rim was covered. A lens was placed before the screen to magnify the image of the interference fringes. The interference fringes were captured directly by a digital color video camera and frame grabber.

§3.44 Results and Conclusion

From Figure 3 - 38 (a), (b), (c), we can see two types of interference fringes. One is a set of circular fringes, which are likely to be the fringes of equal inclination generated by the two reflected beams from mirror and the part of internal homogenous surface of the sapphire tube sheath perpendicular to the mirror. Another set are of curved shape, which are likely to be produced by the two reflected lights from mirror and the part of internal irregular surface of the sapphire tube sheath. It seems that the phenomenon coincides with the shape of the internal surface of the sapphire tube sheath on which large parts of light are reflected along the same direction, as is shown in Figure 3 - 37 (d), (a), (c), respectively. The same situations also are observed in Figure 3 - 37 (b), the rough internal surface of the sapphire tube sheath made the light scatter so that the output of interference fringes is straight or curved fringes, as it is shown in Figure 3 - 38 (d). Obviously, there is the potential to fabricate a monolithic sapphire fibre-optic Fabry-Perot sensor by the sapphire tube sheath. However, the following problems should be solved in advance if considering the structure and assembly of the monolithic sapphire fibre-optic Fabry-Perot sensor:

1) The investigation on the formation and its process of internal homogenous surface of the sapphire tube sheath during cooling will be an important aspect in future work, for the uneven surface will cause the light to be highly scattered, as a result, there will be strong background noise in the output signal of the monolithic sapphire fibre-optic Fabry-Perot sensor.

2) The internal surface of the sapphire tube sheath produced by melting should be able to be adjusted easily to keep parallel with the endface of the sapphire fibre to form a Fabry-Perot cavity. Otherwise, the assembly of the monolithic sapphire fibre-optic Fabry-Perot sensor will be difficult.

3) Under the high temperature, the thermal expansion of the internal surface of the sapphire tube sheath formed by melting can lead to drifting, distortion, and loss of the output signal of the monolithic sapphire fibre-optic Fabry-Perot sensor assembled under the room temperature. Therefore, study of the process of thermal expansion of

the internal surface of the sapphire tube sheath should be further finished.

4) If the transformation of the internal surface of the sapphire tube sheath produced by outside vibration is asymmetrical, the same situation discussed in 3) can also appear. Therefore, further research on the transformation process of the internal surface of the sapphire tube sheath under the vibration environment outside should be done in future.

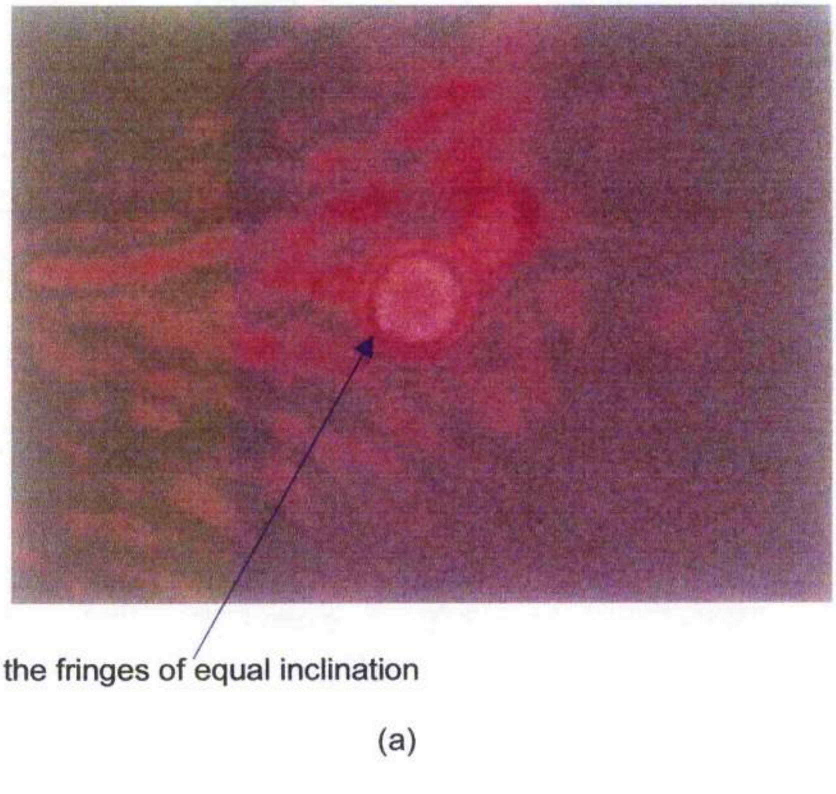

(a)

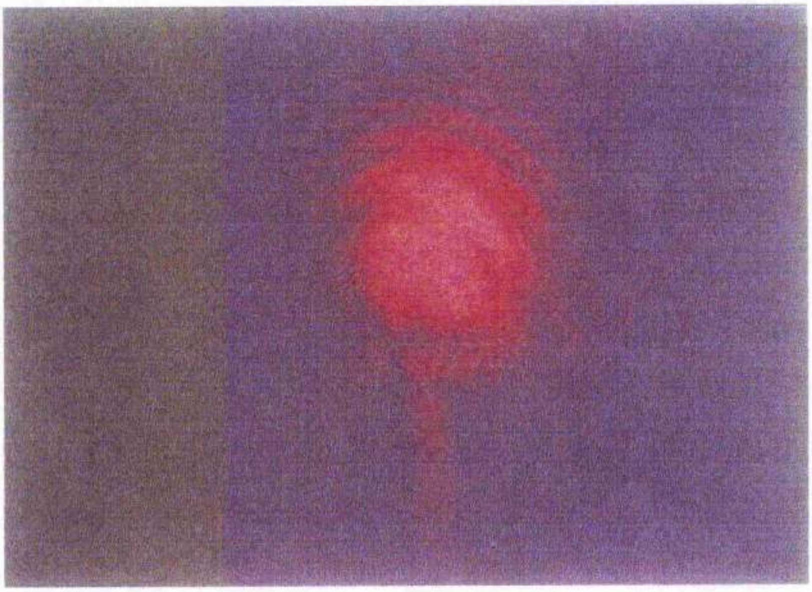

(b)

(c)

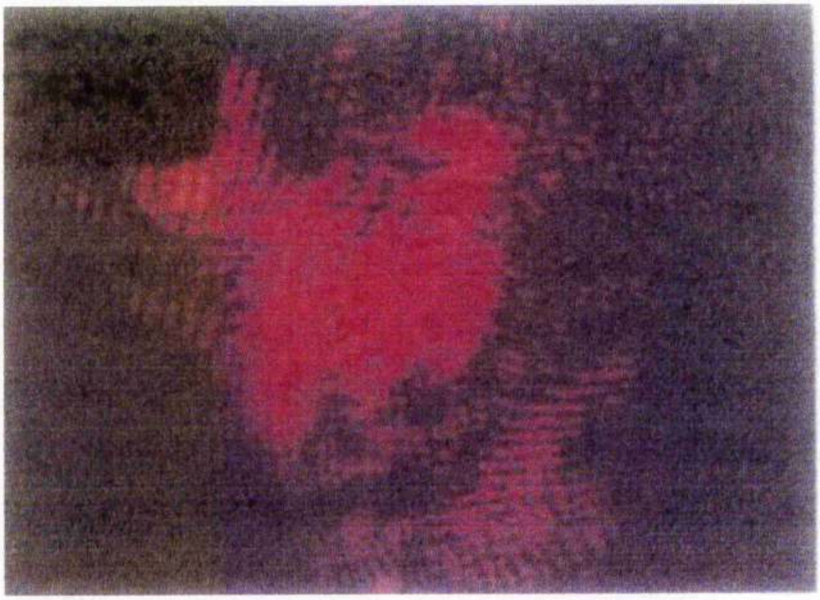

(d)

Figure 3 - 38 the interference fringes generated by the two reflected lights from mirror and the part of internal surface of sapphire tube sheath

§4 Summary and Conclusion

We have investigated a number of topics related to establish a procedure of prototype to monitor the process of fabrication of a Fabry-Perot cavity.

A function of separation between the angle of wedge-shaped air gap of two slightly inclined optical flats and interference fringes of equal thickness was investigated and deduced. Two methodologies were presented to check the consistency:

1. Experimental method

   Measuring the separation of the interference fringes to calculate the wedge angle (MIF).

2. Theoretical analysis

   Direct calculation by measuring the thickness of the separating shim (DC).

From the results obtained in this experiment, the separation of fringes calculated by experimental method has shown the clear difference in comparison with the theoretical analysis. The percentage difference of results between the two methods is 80.47%. It was found that the inconsistency could be attributed to the following reasons. First, because the incident light beam is almost perpendicular to the surface of the optical flats, all the reflected light from the surfaces of the flats are almost projected to the same areas in the field of view. The interference fringes observed, as a result, could be a type of mixed interference fringes formed by the reflected light from the surfaces of four optical flats, instead of those only produced by the reflected light from two interfaces of wedge-shaped film of air. Second, the intensity of light beam is so strong, though part of light had been reflected by beam splitter, that the true interference fringes produced by the reflected light from two interfaces of the wedge-shaped film of air were obscured by the reflected light from other surfaces of the optical flat. The use of a spatial filter can reduce the inconsistency. The percentage difference of results between the method of interference fringes and the direct calculated method decreased considerably from 80.47% to 3.99% after the spatial filter was introduced into the setups. However, there are still some other factors except for the errors above-mentioned of which affect the exactness of wedge-shaped angle such as the thickness of optical flat, the coherence length of source, limitation of the viewing system, subjective, resolution of the instrument, the corresponding solutions also were proposed. The angle of a wedge-shaped sheet of glass was calibrated by this method.

An intrinsic sapphire fibre-optic Fabry-Perot sensor was fabricated, and the functional relationship between the output of interference signal of the intrinsic sapphire fibre-optic Fabry-Perot sensor and temperature was deduced. The variation of temperature could be translated into the output of the number of interference fringes which can be recorded by oscilloscope or chart recorder.

A theoretical analysis showed that the output signal of the intrinsic sapphire fibre-optic Fabry-Perot sensor will be weaker considerably than and equal to the 7.03% intensity of light launched into the sensor though the interference fringes have a good visibility which is near to 1 theoretically. The experiment proved the result that the poor optical resolution of the current travelling microscope with vernier scale and JVC digital color video camera was not good enough to shoot the high quality pictures for interference fringes. Therefore, one with higher resolution should be considered to improve this situation in future. An oscilloscope was used to observe the output of the intrinsic sapphire fibre-optic Fabry-Perot sensor, and a chart recorder counted the number of interference fringes. The fitting equation, the functional relationship between the output of the number of interference fringes of the intrinsic sapphire fibre-optic Fabry-Perot sensor and temperature, was obtained by data fitting. There is a near to linear relationship between the ten temperatures measured and the output signal of the intrinsic sapphire fibre-optic Fabry-Perot sensor for the range of temperature 75 °C - 435 °C. The output of the number of interference fringes when the temperature goes up from room temperature 20 °C to 435 °C were calculated, and the change of the length of single crystal sapphire fibre along the c-axis was 19.2 μm. Nevertheless, the output of the sensor could suffer from some background noise, that is:

i) The straight interference fringes produced by beam splitter interweave with the circular interference fringes output by the intrinsic sapphire fibre-optic Fabry-Perot sensor so that it will lead to a strong noise. Consequently, the coated pellicle beam splitter should be considered to be an alternative in future.

ii) The reflected light from the microscope objective was also an important factor. However, it can be improved by using all fibre-optic system in future.

iii) In view of the fact that the sapphire fibre is heated by nonuniform way limited by the shape of the solder iron, it causes the changes of the output of the sensor. Therefore, further experiment for calibration needs to be done in future.

An extrinsic sapphire fibre-optic Fabry-Perot sensor was fabricated, and the functional relationship between the output of interference signal of the extrinsic sapphire fibre-optic Fabry-Perot sensor and temperature was deduced. The variation of temperature could be translated into the output of the number of interference fringes which can be recorded by oscilloscope or chart recorder. The high temperature ceramic adhesive based on aluminum oxide was presented to solve the problem unmatched between the different materials and the extrinsic sapphire fibre-optic Fabry-Perot sensor. A theoretical analysis showed that during the process of the fabrication of interferometer cavity, the length of cavity should meet the following condition if $\Delta L_a^{\max} + \Delta L_b^{\max} > \Delta L_g^{\max}$, that is, $\Delta L_a^{\max} + \Delta L_b^{\max} - \Delta L_g^{\max} \le L < \frac{\lambda^2}{\Delta\lambda}$. The output signal of the extrinsic sapphire fibre-optic Fabry-Perot sensor will be about equal to the 6% intensity of light launched into the sensor though the interference fringes, theoretically, have a good visibility like the intrinsic sapphire fibre-optic Fabry-Perot sensor. The experiment proved the result theory predicted that the output of the interference fringes of the extrinsic sapphire fibre-optic Fabry-Perot sensor can not readily be observed by the low resolution travelling microscope with vernier and JVC digital colour video camera. Therefore, one with higher resolution should be considered to improve this situation in future. The chart recorder was used to count the number of interference fringes up to the temperature 435°C. The irregular output signal of the extrinsic sapphire fibre-optic Fabry-Perot sensor shows that background noise was prevalent in the system, that is:

1) The coated pellicle beam splitter was used to replace the bulk beam splitter, the interference fringes output by the extrinsic sapphire fibre-optic Fabry-Perot sensor is still affected by the interference between the microscope objective and sapphire fibre a. Also, the output of interference fringes of the extrinsic sapphire fibre-optic Fabry-Perot sensor can be quite weak. Consequently, an all fibre-optic system was proposed to be an alternative to the current free space arrangement in future.

2) The experiment showed that due to the coherence length of HeNe laser, the reflected light from the two endfaces of lead - in fibre also gave rise to interference fringes and resulted in an overlap between the fringe of the intrinsic effect and that of the extrinsic effect. Therefore, a laser with shorter coherence length was suggested being considered as an alternative in future work.

3) The sapphire fibre is heated in a nonuniform way limited by the shape of the soldering iron. Therefore, further experiment for exact calibration needs to be done in future.

4) In order to fabricate and calibrate the cavity of the extrinsic sensor, a new setup which can exactly control the distance and situation of the FP cavity needs to be built up in future.

White light interferometric signal processing techniques were used in the system of extrinsic sapphire fibre-optic Fabry-Perot sensors for its high stability and accuracy. It was found that the output signal of the EFPI sensor includes a large amount of noise so that very low fringe visibility is obtained. The noise is caused by the unstable output of the light source in the current system. As a result, with the increase of load voltage, the noise level is correspondingly enhanced with the intensity output of the LED. The contamination caused by airborne particulate and man-made faults also led to the higher level of noise. Consequently, some special protective precautions should be taken. Also, the scattered and reflected light from the splitter, lens, beam expander, etc were the major factors which produce the background signal. By adjusting the angle of the splitter and the angle between the principle axis of the microscope objective and the axis of the sapphire fibre, we can filter a part of scattered light from the splitter. The experiment showed that using a more sensitive optical detector, and a focussing lens before the spectrometer to focus the signal does not improve the noise level because the remaining background signal is also strengthened at the same time as the desired signal. In summary, the reason why the present set-up used is not suitable for detecting the interference signal of sapphire EFPI sensor by white light interferometric signal processing techniques is not only the noise caused by reflected and scattered light from splitter, lens, etc but also due to the large loss of the cavity signal caused by multiple reflections. Therefore, we must change the present experimental set-up into all-fibre setup to detect the interference signal in future work.

The phase relationship between the output of the interference signal of monolithic sapphire fibre-optic Fabry-Perot sensors and the angular frequency of sound wave was deduced. Some monolithic sapphire Fabry-Perot cavities were fabricated by laser, and their internal surface were observed. Michelson interferometric testing was also used to assess the optical quality of the internal surface of the melted end of the sapphire tube. The experiments showed that the interference fringes of equal inclination could be achieved if the internal surface of the monolithic sapphire Fabry-Perot cavities were a homogenous surface. The rough internal surface of the monolithic sapphire Fabry-Perot cavities made the light scattered so that the output of interference fringes is straight or curved fringes. Obviously, there is the potential to fabricate a monolithic sapphire fibre-optic Fabry-Perot sensor by the sapphire tube sheath.

§5 Appendix and References

Appendix A

References

1. James R. Cooper, Optical Fibre Thermometry: Quest For Precision, *Photonics Spectra*, Nov 1985, P71.
2. W. S. Cheung, *Sensors & Actuators*, Vol.19, P105 (1989).
3. J. P. Dakin and K. A. Kahn, A novel fibre-optic temperature probe, *Opt. Quantum Electron.* 9 (1977) 540.
4. J. P. Dakin and B. Culshaw, *Optical Fibre Sensors*, Artech, MA, 1988.
5. T. G. Giallorenzi, J. A. Bucaro, *etal*, *IEEE J. Quant. Electron.* 18, 626-665, 1982.
6. Frank L. Pedrotti, S. J., Leno S. Pedrotti, *Introduction to Optics*, 1993.
7. K. A. Murphy, A. J.Plante, A. Wang, and M. F. Gunther, *Conf. on Optical Fibre Communication (OFC/IOOC).* San Jose, Ca., 1993.
8. R. R. Dils, High-temperature Optical Fibre Thermometer, *J. Appl. Phys.* 54 (3), March, 1983.
9. K. A. Murphy, G. Z.Wang, *etal*, *SPIE OE/Fibres*, (Boston, MA), 1588, 117 (1991).
10. A. Wang, S. Gollapudi, *etal*, Advances in sapphire-fibre-based intrinsic interferometric sensors, *Optics Letters*, Vol. 17, No. 21, Nov. 1, 1992.
11. Anbo Wang, Sridhar Gollapudi, *etal*, Sapphire optical fibre-based interferometer for high temperature environmental application, *Smart Mater. Struct.* 4 (1995) 147-151.

12. J. H. Sharp, H. C. Seat, *etal*, Single-Crystal Ruby Fibres for Fluorescence-Based Temperature Sensing, *Section J: Optical Sensors*, Sensors and their Applications X, 5-8 (219) Sep. 1999.
13. Toshihiko Yoshino, Kiyoshi Kurosawa, *etal*, Fibre-optic Fabry-Perot interferometer and its sensor applications, *IEEE J. of Quantum Electronics*, Vol. QE-18, No. 10, Oct. 1982.
14. B. Budiansky, D. C. Drucker, *etal*, Pressuresensitivity of a clad optical fibre, *Applied Optics*, Vol. 18, No. 24, 4085 15 Dec. 1979.
15. J. A. Bucaro, H. D. Dardy, *etal*, Optical fibre acoustic sensor, *Applied Optics*, Vol. 16, No. 7, 1761, July, 1977.
16. Eric Udd, Fibre Optic Sensors- An introduction for engineers and scientists, *John Wiley & Sons. Inc*, 1991.
17. G. B. Hocker, Fibre optic acoustic sensors with composite structure:an analysis, *Applied Optics*, Vol. 18, No. 21, 3679, 1 Nov. 1979.
18. Lee C. E. and Taylor H. F. Fibre-optic Fabry-Perot temperature sensor using a low-coherence light source, *J. Lightwave Technology*, 9, 129-134, 1991.
19. Farahi F, Newson T. P., *etal*, Coherence multiplexing of remote fibre Fabry-Perot sensing system, *Opt. Commun.* 65, 319-321, 1988.
20. R. S. Longhust, Geometrical and Physical Optics, *Longman*, 1973.
21. J H Sharp, Laser applications, *Notes*.
22. Kent A. Murphy, William V. Miller III, *etal*, Miniaturized fibre-optic Michelson-type interferometric sensors, *Applied Optics*, Vol. 30, No. 34, 5063, 1 Dec. 1991.
23. D. A. Jackson, R. Priest, *etal*, Elimination of drift in a sing-mode optical fibre interferometer using a piezoelectrically stretched coiled fibre, *Applied Optics*, 19, 2926-2929, 1980.
24. Rao Y J and Jackson D A, Prototype fibre-optic-based Fizeau temperature sensor using coherence reading and mechanical amplification for medical applications, *Proc. SPIE* 2292, Paper 46, 1994.
25. G. A. Magel, D. H. Jundt, *etal*, Infrared Optical Materials and Fibres, *SPIE*. Vol. 618, P. 89, 1986.
26. M. m. Fejer, J. L. Nightingale, *etal*, Proceedings of Guided Wave Optoelectronic Materials, *SPIE* Vol. 460, P. 26, 1984.

27. J. stone and C. A. Burrus, *Fibre and Intergrated Optics*, Vol. 2, No. 1, P. 19, 1979.

28. R. R. Sholes, J. G. Small, Fluorescent decay thermometer with biological applications, *Rev. Sci, Instrum.*, Vol. 51, N7, 882-884, 1980.

29. Zhiyi Zhang, K. T. V. Grattan, *etal*, A novel signal processing scheme for a fluorescence based fibre-optic temperature sensor, *Rev. Sci. Instrum.*, V62, N7, 1735-1742, 1991.

30. B. J. Lieser, S. D. Tilstra, Design and Test of an Optical Engine Inlet Temperature Sensor, *SPIE,* Vol 2295, 151-155, 1994.

31. K. T. V. Grattan, A. W. Palmer, *Rev. Sci. Instrum.*, 56(9), 1784, 1985.

32. K. T. V. Grattan and Z. Y. Zhang, Fire Optic Fluorescence Thermometry, *Chapman & Hall*, 1995.

33. Francis A. Jenkins and Harvey E. White, Fundamentals of Optics, *McGrAW-Hill International Editions*, 1976

34. Y. R. Chen_Jan Wang, Traditional Materials and New Materials, *Univ. of Tian Jin,* 1999

35. Yu Zou, the Analysis method of Materials, *Univ. of Ha Er Bin*, 2000.

36. Claude Belleville and Gaetan Duplain, White-light interferometric multimode fibre-optic strain sensor, *Optics Letters*, Vol. 18, No. 1, Jan 1, 1993.

37. Tianchu Li, Anbo Wang, *etal*, White-light scanning fibre Michelson interferometer for absolute position-distance measurement, *Optics Letters*, Vol. 20, No. 7, Apr. 1, 1995.

38. Libo Yuan, White-light interferometric fiber-optic strain sensor from three-peak-wavelength broadband LED source, *Applied Optics*, Vol. 36, No. 25, 1 Sep. 1997.

39. K. T. V. Grattan and B. T. Meggitt, Optical Fiber Sensor Technology, *Kluwer Academic Publishers,* 2000.

Appendix B

The output of intrinsic sensors from the chart record

LLOYD INSTRUMENTS

LLOYD INSTRUMENTS PLC Segensworth, Fareham, England. Telephone: (04895) 4221
LLOYD INSTRUMENTS SA 78230 Montigny Le Bretonneux, France. Telephone: (1) 30 57 40 74

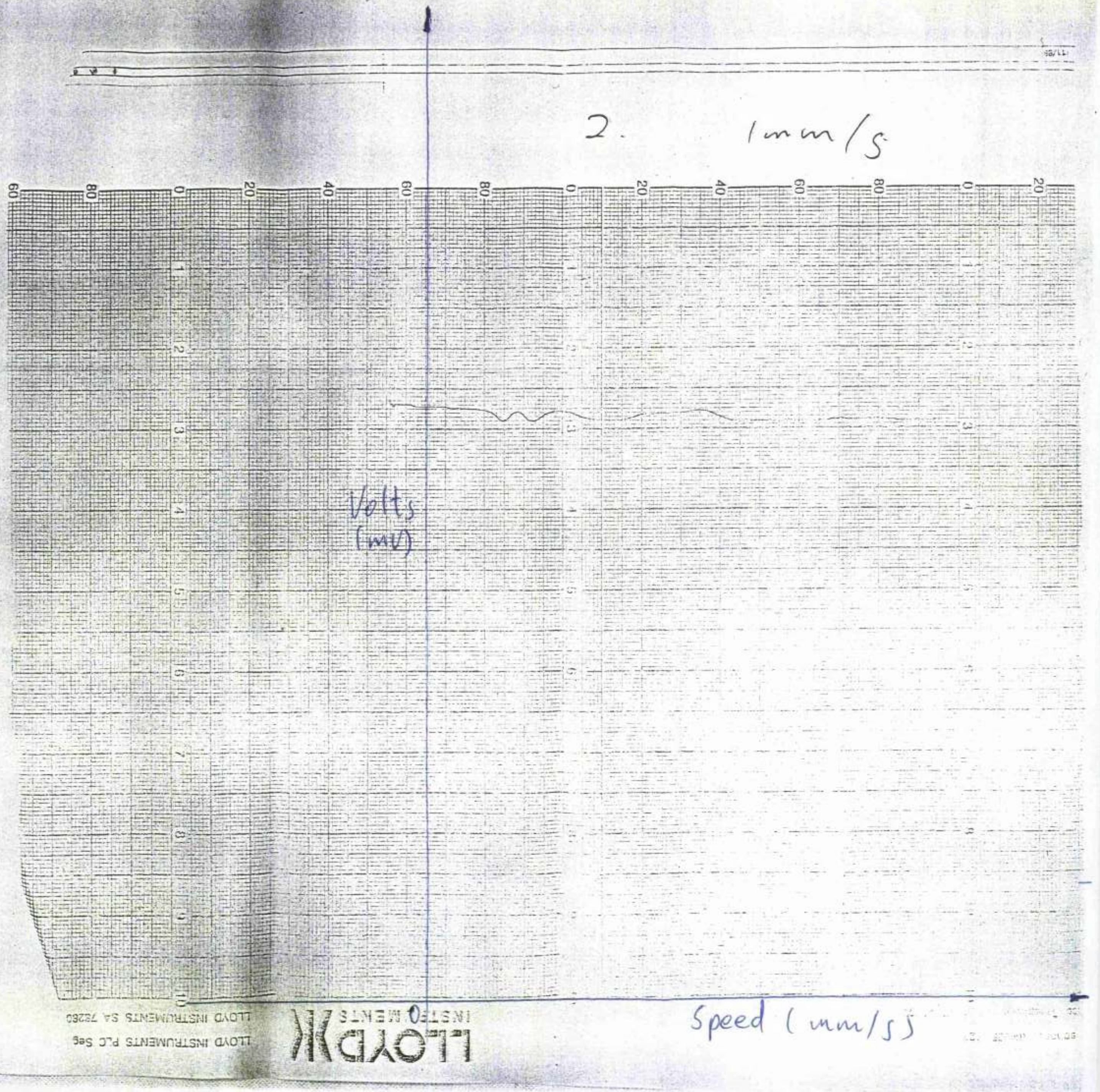
2. 1mm/s
Volts (mV)
Speed (mm/s)
LLOYD INSTRUMENTS
LLOYD INSTRUMENTS PLC Seg
LLOYD INSTRUMENTS SA 78280
60
80
0
20
40
60
80
0
20
40
60
80
0
20
1
2
3
4
5
6
7
8
9
10

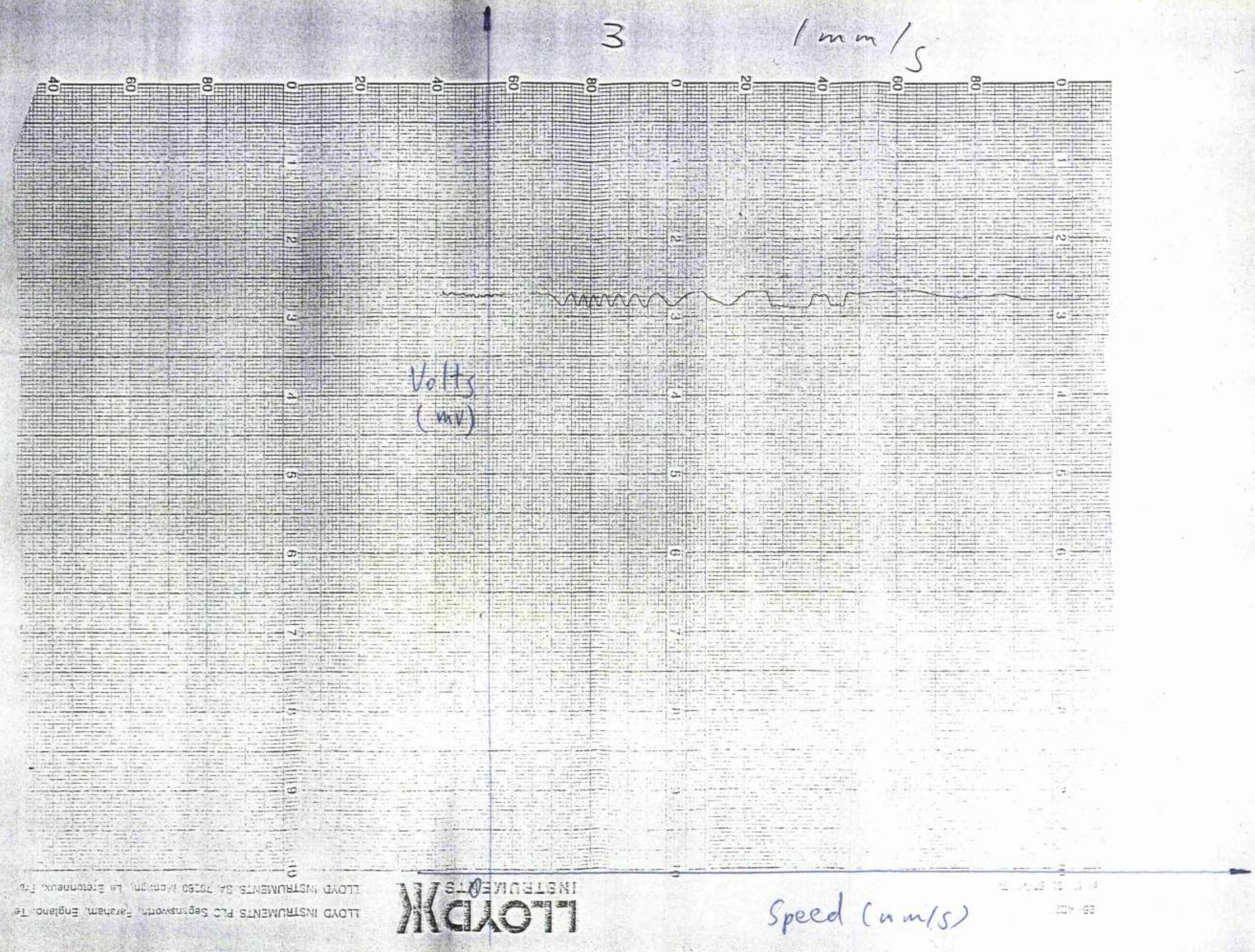
3
1 mm/s
Volts
(mV)
Speed (mm/s)
LLOYD INSTRUMENTS
LLOYD INSTRUMENTS PLC Segensworth, Fareham, England
LLOYD INSTRUMENTS SA 79160 Montigny, Le Bretonneux, France
0
1
2
3
4
5
6
7
8
9
10
20
40
60
80

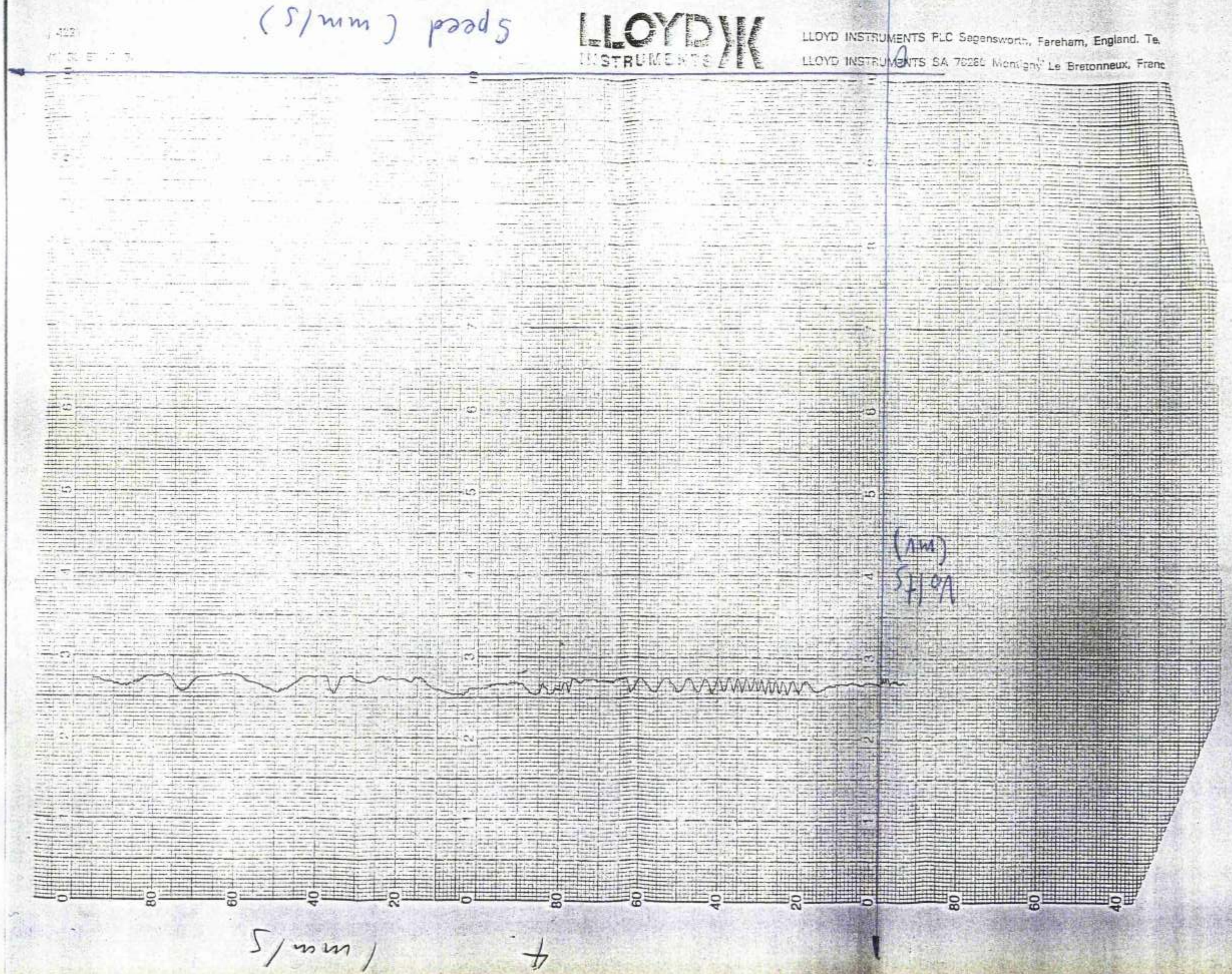
Speed (mm/s)
LLOYD INSTRUMENTS
LLOYD INSTRUMENTS PLC Segensworth, Fareham, England. Te
LLOYD INSTRUMENTS SA 78280 Montigny Le Bretonneux, Franc
Volts (mV)
0
1
2
3
4
5
6
7
8
9
10
0
80
60
40
20
0
80
60
40
20
0
80
60
40
4
(mm/s

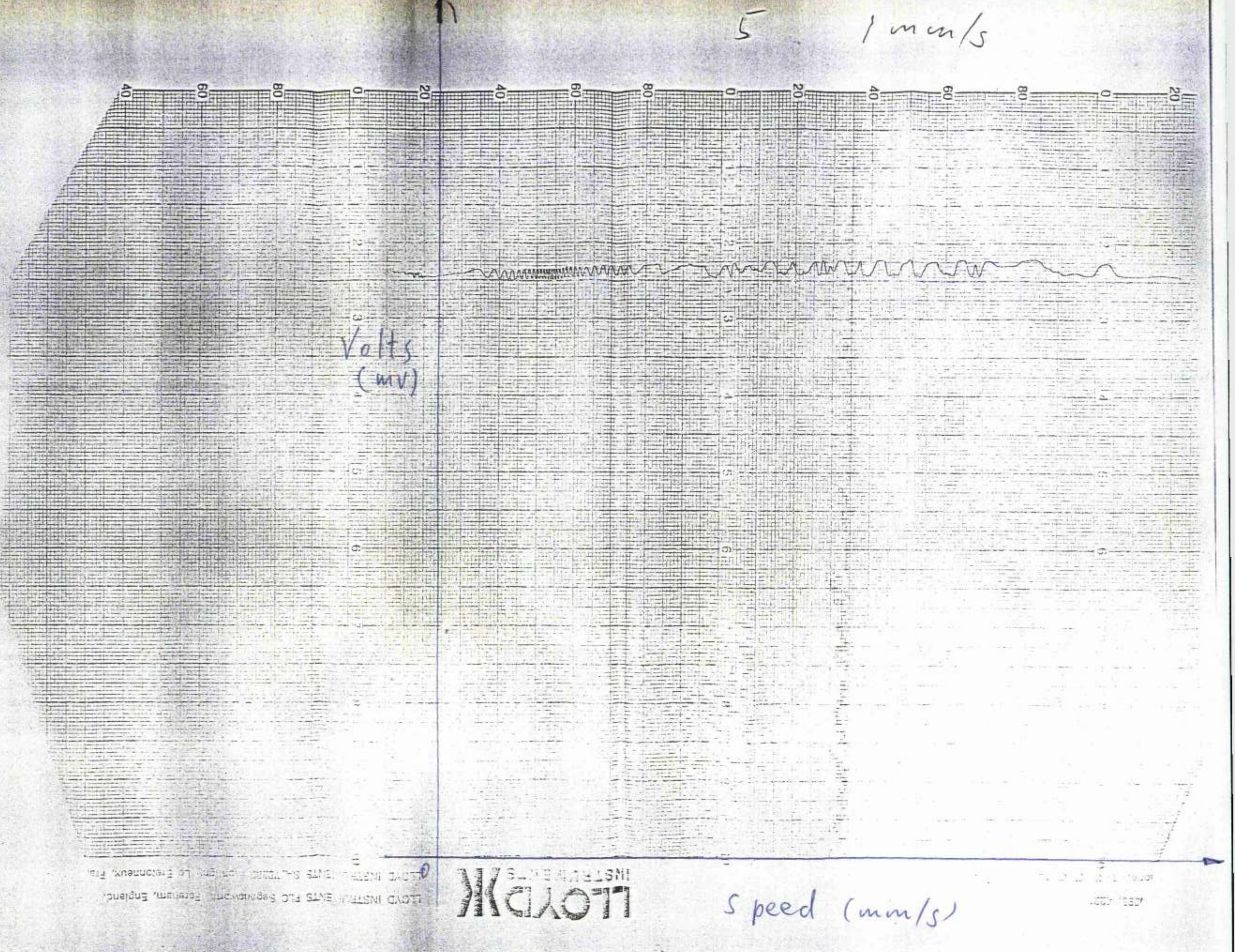
5
1 mm/s
Volts
(mV)
0
Speed (mm/s)
40
60
80
0
20
2
3
4
5
6
LLOYD INSTRUMENTS

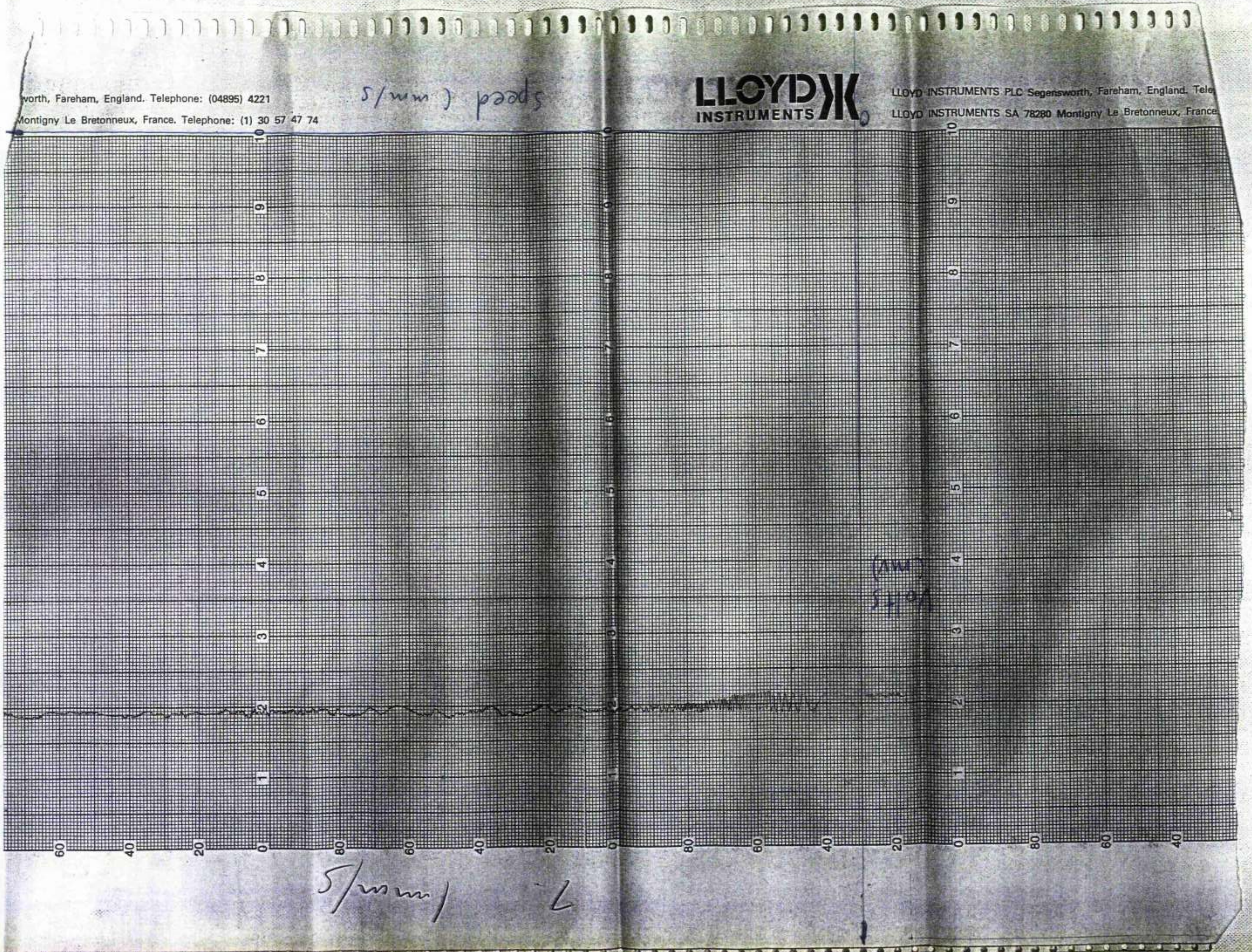
worth, Fareham, England. Telephone: (04895) 4221
Montigny Le Bretonneux, France. Telephone: (1) 30 57 47 74
LLOYD INSTRUMENTS
LLOYD INSTRUMENTS PLC Segensworth, Fareham, England. Tele
LLOYD INSTRUMENTS SA 78280 Montigny Le Bretonneux, France
speed (mm/s
volts (mV)
10
9
8
7
6
5
4
3
2
1
0
20
40
60
80
7 (mm/s

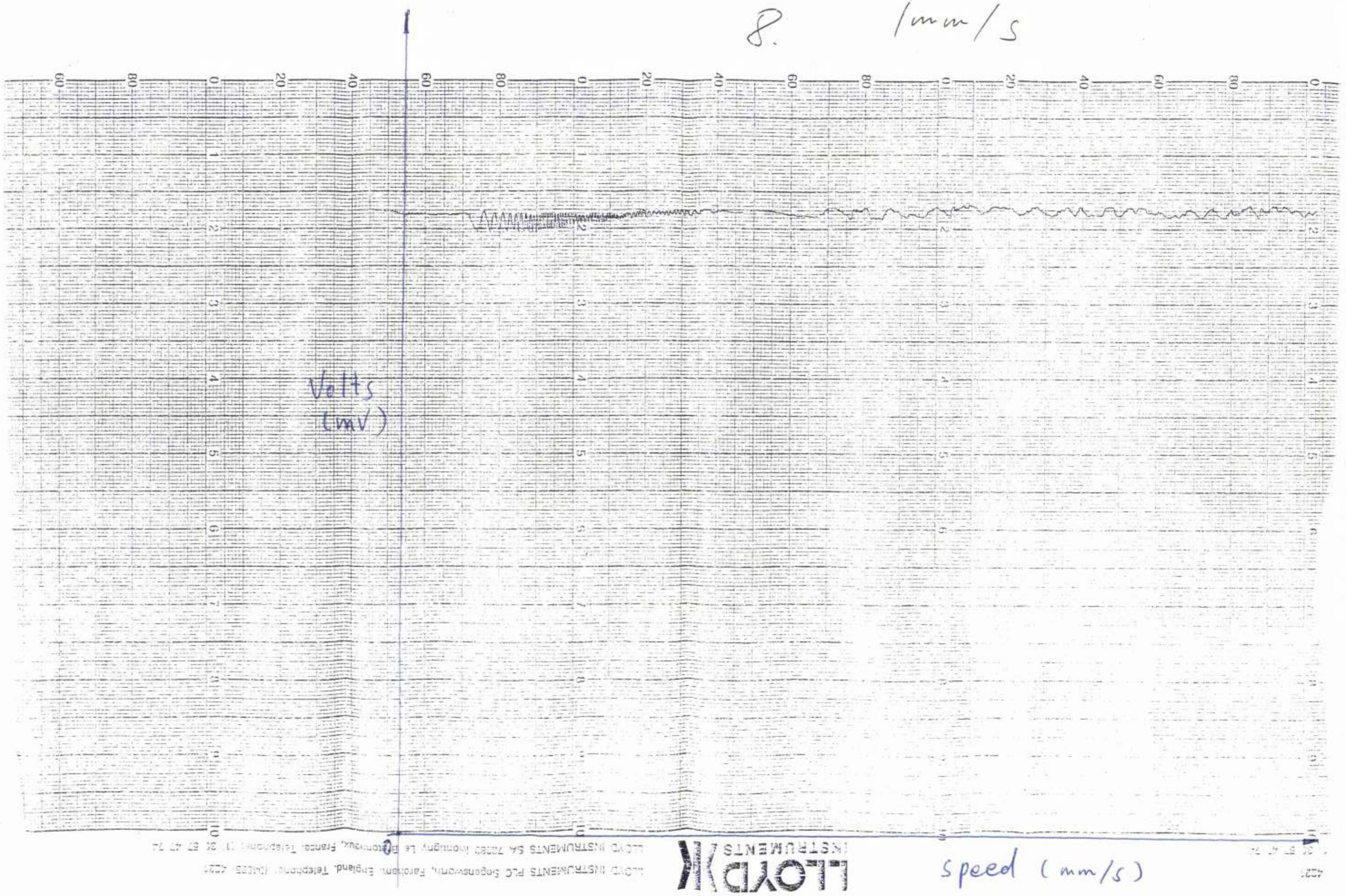
8.
/mm/s
Volts
(mV)
0
speed (mm/s)
LLOYD INSTRUMENTS
LLOYD INSTRUMENTS PLC Sogenswortn, Fareham, England. Telephone (04895 4221
LLOYD INSTRUMENTS SA 78280 Montigny Le Bretonneux, France. Telephone (1) 30 57 47 74
DN6 5006

LLOYD INSTRUMENTS

LLOYD INSTRUMENTS PLC Segensworth, Fareham, England. Telephone: (04895) 4221
LLOYD INSTRUMENTS SA 78280 Montigny Le Bretonneux, France. Telephone: (1) 30 57 47 74

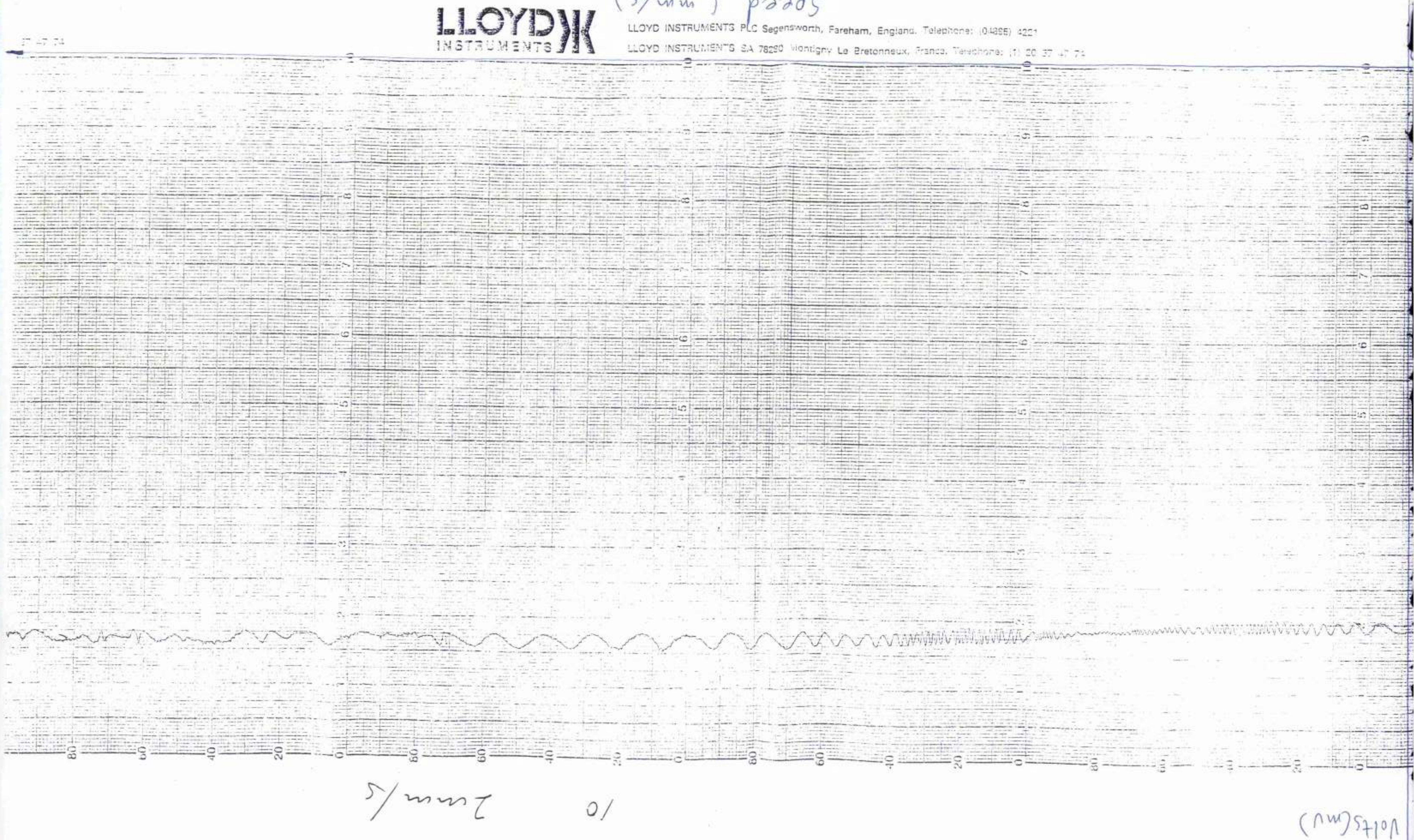

Appendix C

Video Cassette

Available to Dr James H. Sharp, Department of Mechanical Engineering, University of Glasgow.